Spatial distribution of snow accumulation and snowpack properties in Dronning Maud Land, Antarctica: Observational techniques and methods for surface mass-balance assessments of polar ice sheets

Räumliche Verteilung von Schneeakkumulation und Schneedeckeneigenschaften in Dronning Maud Land, Antarktis: Observationstechniken und Methoden der Netto-Massenbilanzbestimmung polarer Eisschilde

Gerit Rotschky

Ber. Polarforsch. Meeresforsch. 552 (2007)
ISSN 1618 - 3193

Gerit Rotschky
Stiftung Alfred-Wegener-Institut für Polar- und Meeresforschung Bremerhaven
Columbusstraße
Postfach 120161
D-27515 Bremerhaven

Die vorliegende Arbeit ist die inhaltlich geringfügig veränderte Fassung einer kumulativen Dissertation, die 2006 dem Fachbereich Geowissenschaften der Universität Bremen vorgelegt wurde. Die Arbeit ist in elektronischer Form verfügbar unter http://nbn-resolving.de/urn:nbn:de:gbv:46-diss000106148.

Contents

Zusammenfassung

Hauptziel der vorliegenden Arbeit war die Bestimmung der Verteilung von Schneeakkumulation und der sie beeinflussenden Faktoren im Dronning Maud Land (DML), Antarktis, durch Kombination verschiedener Untersuchungsmethoden. Für weite Teile des Antarktischen Eisschildes stehen Feldmessungen der Netto-Massenbilanz nur spärlich zur Verfügung. Deshalb untersucht diese Studie, wie gut sich abbildendes Satellitenradar für eine räumlich kontinuierliche Erfassung von Akkumulationsmustern in hoher Auflösung eignet. Dafür werden zunächst die Rückstreueigenschaften der antarktischen Schneedecke mittels gering-aufgelöster C- und Ku-Band Scatterometerdaten analysiert, um Verknüpfungen zwischen Schneemorphologie und Radarecho abzuleiten. Als ein bedeutendes Ergebnis daraus wird eine Schneedeckenklassifikation für die gesamte Antarktis präsentiert, welche für beide Frequenzen ein ähnliches Muster zeigt. Die schmale Perkolationszone am Rande des Eisschildes konnte außerdem von der den Antarktischen Eisschild dominierenden Trockenschneezone abgegrenzt werden.

Neben der Temperatur gilt die Akkumulationsrate von Schnee als ein wesentlicher Einflussfaktor auf die morphologischen Eigenschaften der Schneedecke, in erster Linie auf Korngröße und Schichtenverteilung. Daraus ergibt sich die Frage, ob Synthetic Aperture Radar (SAR) zur Erfassung der räumlichen Verteilung der Akkumulationsraten eingesetzt werden kann. Aus einfachen linearen Regressionsanalysen zwischen Bodenreferenzdaten und dem Rückstreukoeffizienten σ^0, aufgenommen vom Envisat ASAR-Sensor, wird geschlussfolgert, dass die Korrelation zwischen Rückstreuung und Akkumulationsrate nicht für die gesamte Bandbreite an existierenden Schneedeckentypen eindeutig ist. Die Einsetzbarkeit satellitengestützter Radarsysteme zur Erfassung von Akkumulationsraten ist begrenzt auf Bereiche mit geringer Akkumulation innerhalb der Trockenschneezone. Für das Gebiet um die EPICA-Tiefbohrung an der Kohnen Station wird eine erste SAR-basierte, hochaufgelöste Akkumulationskarte vorgestellt und mit früheren, aus Punkdaten interpolierten Karten verglichen. Der Unterschied in der Netto-Massenbilanz beträgt insgesamt 20%, was einen deutlichen Hinweis auf gegenwärtige Unsicherheiten bei der Quantifizierung der Massenbilanz der Antarktis gibt.

Als Bodendaten stehen Firnkern- und Schneeschachtmessungen sowie kontinuierliche Akkumulationsprofile, gewonnen aus Bodenradaraufnahmen (IPR) und Pegelstangenmessungen, zur Verfügung. Die vorliegende Arbeit beleuchtet Vorteile und Grenzen dieser Techniken zur Bestimmung von Akkumulationsraten und deren räumlichen Verteilung. Mit IPR, ergänzt durch Firnkernstudien, lässt sich die hohe räumliche Variabilität der Massenbilanz sehr gut erfassen. Die Analyse zweier, insgesamt 320 km langer IPR-Profile aus dem DML Plateaugebiet bestätigt beträchtliche Schwankungen um bis zu 50% auf Entfernungen von Kilometern. Diese werden bereits durch leichte Oberflächenwellen hervorgerufen, die vermutlich mit der Untergrundtopographie in Verbindung stehen. Aus dieser Information kann die räumliche Repräsentativität einzelner Punktmessungen für ihre weitere Umgebung abgeschätzt werden. Firnkerne haben den Vorteil, Langzeitmittel der Akkumulationsrate zu liefern, die weniger anfällig für das hohe zeitliche Rauschen in der Schneeablagerung auf lokaler Ebene sind. Die Arbeit zeigt eine vollständige Zusammenstellung verlässlicher Akkumulationspunktdaten für DML, die im Zuge zahlreicher Feldkampagnen verschiedener Nationen über die letzten 5 Jahrzehnte gewonnen wurden. Eine Kriging-Interpolation dieses Datensatzes offenbart die großräumige Akkumulationsverteilung, die v.a. durch Topographie, Höhenlage und Entfernung zum

offenen Ozean kontrolliert wird. Demzufolge schwankt die Akkumulation im DML im Mittel von 19 kg m^{-2} a^{-1} im Südosten des Untersuchungsgebietes bis zu einem Maximum von 491 kg m^{-2} a^{-1} auf dem Jutulstraumen. Die höchste Variabilität existiert in steil ansteigenden Bereichen des Eisschildes, verursacht durch starke katabatische Winde.

Diese Studie trägt zu einem besseren Verständnis der Komplexität der Schneeakkumulation in der Antarktis bei. Die Ergebnisse sind besonders für die numerische Modellierungen des Antarktischen Eisschildes und die Interpretation von Eisbohrkerndaten von Interesse. Für die Kalibrierung und Validierung von bevorstehenden satellitengestützten Radaraltimeter-Missionen, z.B. Cryosat der ESA, ist das Wissen um Rückstreueigenschaften in Abhängigkeit von der Schneedeckenmorphologie von großer Bedeutung. Diese Studie bestätigt letztlich auch den möglichen Einsatz von abbildendem Radar zur Reduzierung von Unsicherheiten bei der Interpolation von Felddaten über weite Entfernungen.

Abstract

Primary objective of this thesis is the investigation of the spatial distribution of snow accumulation and its influencing factors in Dronning Maud Land (DML), Antarctica, by using a combination of data from different observation techniques. Field measurements of surface mass balance are only sparsely available for most parts of the Antarctic ice sheet. The main focus of this study is on exploring the potential of radar satellite imagery for a spatially continuous assessment of accumulation patterns in high resolution. For this, radar backscattering properties of the Antarctic snowpack are analysed by means of low-resolution C- and Ku-band scatterometer data to establish links between returned radar signals and snow morphology. As a result, a continent-wide snowpack classification is presented, which shows similar patterns for both frequencies. Furthermore, the narrow percolation zone at the margin of the ice sheet could be distinguished from the interior dry-snow zone.

Beside temperature, snow accumulation rate is seen as a key factor that determines snowpack properties, in the first line grain size and subsurface layering. This is giving raise to the question, whether Synthetic Aperture Radar (SAR) data could be utilized to trace spatial accumulation changes by means of the sensed radar signal strength. Simple linear regression analyses are carried out between ground truth accumulation data and the backscattering coefficient σ^0, acquired by the Envisat ASAR sensor. From this, the correlation between the backscattering and accumulation rate was found to be not unique over the entire range of existing snowpack types. The capability of satellite radar imagery to quickly map accumulation patterns is limited to low accumulation areas within the dry-snow zone. A first high-resolution accumulation map based on SAR data is presented for the area of the EPICA deep ice core drilling site near Kohnen station, which is compared to an earlier compilation interpolated from in-situ point data. The total difference of 20% gives an indication for the present uncertainties in quantification of ice-sheet surface mass balance. The SAR based accumulation map indicates a much larger spatial variability of accumulation rates than previously assumed, even on the relatively smooth topography of the interior ice-sheet plateau.

Ground truth was available in the form of firn core and snow pit point measurements, as well as continuous accumulation profiles obtained by ice-penetrating radar (IPR) soundings and stake line readings. The study highlights advantages and limits of those techniques for accumulation investigations. IPR-soundings, complemented by firn core studies, provide a powerful tool to resolve the high spatial variability in net surface mass balance. The analysis of two IPR profiles taken on the DML plateau over a distance of 320 km confirms that considerable variations (up to 50%) occur on the km-scale resulting from slight surface undulations, the latter likely related to bedrock topography. This information can be used to estimate the degree to which single point measurements within the same area are representative for their wider surrounding. Shallow to medium depth firn cores have the advantage to provide long-term averaged accumulation rates. Thus, such data are less sensitive to the high temporal noise in snow deposition at a local scale. A complete set of reliable accumulation point records for DML is presented that have been collected in the course of numerous field campaigns carried out by several nations over the last 5 decades. A kriging interpolation from this dataset reveals the broad-scale accumulation distribution as controlled largely by topography, elevation, and distance to the open ocean. According to this, snow accumulation in DML ranges in average from as low as 19 kg m^{-2} a^{-1} at the south-eastern corner of the study area to a maximum of 491 kg m^{-2} a^{-1} on Jutulstraumen, with highest variability in the escarpment region due to enhanced katabatic winds.

This study contributes to a better understanding of the complexity of snow accumulation in the Antarctic. The results are of particular interest to ongoing ice sheet modelling and the interpretation of ice core data. For calibration and validation of forthcoming radar altimetric satellite missions, like ESA's Cryosat, the knowledge of backscattering properties in dependence of snow morphology is of high relevance. Finally, this study confirms the potential of satellite-radar observations to reduce inaccuracies in the interpolation of field data over long distances.

1 Antarctic Mass Balance: Introduction

Antarctica is known as the world's driest desert expressed by an extreme continental climate with very low air temperatures and humidity. The lowest temperature ever recorded was -89°C on July 21, 1983 at the Russian Vostok station (78°28'S, 106°48'E). According to Schwerdtfeger (1984), annual means for the Antarctic ice sheet range from -56°C at the U.S. Plateau Station (79°15'S, 40°30'E, 3625 m a.s.l.) to –9°C at the Australian station Casey on the coast (66°17'S, 110°31'E, 32 m a.s.l.). The Antarctic Peninsula experiences positive values in summer, however with monthly averages only slightly above 0°C. Here, the highest annual mean of -2.5°C was recorded at the Russian station Bellingshausen (62°12'S, 59°00'W, 14 m a.s.l.). Such conditions are preventing a true summer-melt season as it can be observed for the Northern Hemisphere polar regions (Zwally and Fiegles, 1994). Snow precipitation occurs at any time of the year (Hogan and Gow, 1997) but remains very small for most parts of interior Antarctica. Typical values of net annual accumulation rates are less then 100 kg m^{-2} a^{-1} (Vaughan and others, 1999a; Giovinetto and Zwally, 2000). Accumulation extremes can be observed only in coastal escarpment and mountain regions resulting from orographical uplift of maritime air masses, e.g. in Dronning Maud Land (DML) on Jutulstraumen annual values up to 780 kg m^{-2} a^{-1} were reported by Melvold and others (1998) based on stake readings. On a local scale accumulation rates are temporally as well as spatially highly variable mainly because of a coincidental redistribution of snow material by wind activity, already initiated by wind speeds of about 5 m s^{-1} (Frezzotti and others, 2004).

Because of its remoteness and hostile conditions Antarctica remains fairly undisturbed by human activities. It serves as an important climate archive as well as sensitive indicator of climate change. Owing to their influence upon planetary albedo polar regions themselves play a crucial role in regulating global climate (Long and Drinkwater, 1999). The Antarctic ice sheet including ice shelves covers an area of ~12.4 x 10^6 km² (Massom and Lubin, 2006) and stores ~90% of the Earth's ice (25.7 x 10^6 km^3), equivalent to ~70% of the entire fresh water reservoir. During winter sea ice enlarges the ice covered area to more than 30 million km² (Comiso, 2003). The average thickness of the grounded ice sheet is ~2.5 km with a maximum of ~4.7 km observed in the Wilkes sub-glacial basin, East Antarctica (Drewry and others, 1982). If it was to melt completely, this huge glacial mass has the potential to rise sea level by about 61 meters (Huybrechts and others, 2000). With respect to these dimensions, concerns raised that even a small imbalance in mass budget could significantly affect the mean global sea level. The latter is currently believed to rise at an average rate of 1.5-2 mm a^{-1}, however with large uncertainty (Bentley, 2004). Based on geological data, this is about 10 times the average rate occurring over the last 3,000 years (0.1 to 0.2 mm a^{-1}), according to the Intergovernmental Panel on Climate Change (IPCC) assessment in 2001 (IPCC, 2001). Major factors of an accelerating sea-level rise are the combined effects of thermal expansion of the oceans and loss of mass from land ice in response to global warming. Antarctica's contribution in this respect remains a matter of debate despite nearly half a century of intensive research on ice-sheet mass balance and dynamics, since the International Geophysical Year 1957/58. Only recently, it was suggested that the Antarctic ice sheet is nearly in balance with the present climate, with a slightly negative contribution of -0.1 ± 0.1 mm a^{-1} to global sea level rise during the past century (IPCC, 2001). There was a tentative agreement that the Antarctic ice sheet will probably gain mass during the 21st century because of increased precipitation as a consequence of a greater amount of moisture in a warming atmosphere. Surface-height

measurements carried out by radar altimeters first confirmed this assumption showing an increase in the overall thickness of the East Antarctic Ice Sheet (EAIS) interior north of 81.6°S between 1992–2003 (Davis and others, 2005).

However, new findings made possible by improved remote sensing techniques now reveal a much higher spatial variability in the Antarctic mass balance than previously assumed. Recent studies show various Antarctic ice drainage basins to be strongly out of balance (Van den Broeke and others, 2006), evident by a substantial grounding line retreat (Rignot, 1998; Rignot, 2001), significant glacier-thinning rates (Shepherd and others, 2002), loss of buttressing ice shelves and consequently acceleration of outlet glaciers along the edge of the West Antarctic Ice Sheet (WAIS) (Rignot and others, 2002; Thomas and others, 2004). The latter has attracted special attention because it is grounded below sea level and might therefore turn instable in case the surrounding ice shelves are weakened. The WAIS alone contains enough ice to raise sea level by 6 m, which is in the same order as for the Greenland ice sheet. Similar observations were made for the northeastern and western coast of the Antarctic Peninsula, where over the last 6 decades most of the marine glacier fronts have retreated (Vaughan and Doake, 1996; Scambos and others, 2003; Rott and others, 2002). In particular, the rapid collapse of the vast Larsen B shelf ice (3250 km^2) east side of the Antarctic Peninsula in January and February 2002 made aware of an increased activity at the margin of the Antarctic continent (Rack and Rott, 2004). However, the observed changes might reflect just a natural variability around a mean state. In order to detect a significant trend, long-term monitoring must be carried out.

In consequence of the controversial debate and to better define the ice-sheets sensitivity to climate change research is the more focused on identifying the present mass-balance status of the ice sheet as well as the timescales of ice-volume variability. Both parameters are difficult to determine because of the ice sheet's remoteness, size and complexity. The total mass budget of an ice sheet is traditionally estimated from individual mass balance terms using the *budget method*, which weights losses by *ablation* against the total net input from snow accumulation at the surface and refreezing of ocean water on the ice-shelf bottoms. The grounded Antarctic ice sheet looses mass mainly by glacier/ice stream discharge into floating ice shelves or glacier tongues, where it experiences basal melting, i.e. shelf-bottom melting, and calving of icebergs at the ice-shelf front. The borderline between grounded continental ice sheet and ice shelves is referred to as the *grounding line*. Melting at the surface with subsequent runoff or evaporation of the melt water is uncommon for Antarctica due to very low temperatures even during summer (IPCC, 2001). The term *accumulation* as used in this study refers to snow that is finally deposited directly by precipitation or by wind transport (Paterson, 1994). On a local scale, redistribution of snow due to wind drift can contribute significantly to both, gain or loss of mass. The mass balance is zero for a steady state. The specific mass balance is the mass balance for an individual body of ice averaged over the surface area. To account for density variations it is usually expressed as the rate of change of the equivalent mass of liquid water, in kg m^{-2} a^{-1}. The individual mass balance terms all show considerable temporal and spatial variability and can currently be estimated only with large uncertainty.

Recent technical advances and the accelerating implementation of satellite and airborne remote sensing techniques are likely to reduce the uncertainties in future estimates of ice-sheet mass balance and sea-level change. Radar altimeters enable direct monitoring of surface elevation changes that can be translated into mass balance changes, provided that temperature-driven variations in snow density as well as the vertical motion of the underlying ground associated with isostatic rebound or tectonics

are small or can be determined (e.g. Arthern and Wingham, 1998; Wingham and others, 1998; Zwally and Li, 2002; Thomas and others, 2004; Zwally amd others, 2005). This approach is referred to as *'direct volume change'* method. However, spatial coverage is currently limited to the smooth interior regions of the Antarctic ice sheet north of 81.5°S, because of the poor performance of such sensors over steep-sloping terrain (Rignot and Thomas, 2002). Yet, major thickness changes occur just at the steeper ice-sheet margins. NASA's ICESat, launched in January 2003, carries onboard a laser-ranging instrument (GLAS), providing improved measurement accuracy and spatial coverage. The European Cryosat, supposed to carry a small-footprint radar altimeter, is now unfortunately delayed due to a mission failure in October 2005, but will be rebuild. Furthermore, interferometric synthetic-aperture radar (InSAR) has been applied to infer detailed topography, ice flow dynamics and exact grounding-line positions (e.g. Massonnet and Feigl, 1998; Mohr and others, 1998; Joughin and others, 1999). InSAR can be utilized for precise assessment of mass flux across the grounding line when combined with local ice thickness measurements. Another approach is to determine mass variations of the ice sheet by using gravity-change measurements, as derived by the NASA Gravity Recovery and Climate Experiment (GRACE) satellites (Bentley and Wahr, 1998; Velicogna and Wahr, 2006) or by CHAMP (CHAllenging Minisatellite Payload), a joint venture of the German GFZ and DLR institutes.

Despite these improvements, there is still a lack of data that captures the high spatial variability of surface-mass balance, for instance needed to accurately reconstruct paleoclimate records from ice cores if drilling took place on flowing ice. Recent continent-wide accumulation compilations are inferred primarily from firn-core measurements, which remain sparse for large parts of Antarctica due to the time-consuming and often costly drilling procedure. Estimates of the total Antarctic net snow accumulation have been regularly adjusted upward, because improved prediction methods and new data have become available. Vaughan and others (1999a) applied passive microwave data from satellites as forcing field to control the interpolation of more than 1800 in-situ measurements, yielding 1811 Gt a^{-1} over grounded ice and 2288 Gt a^{-1} including all ice shelves. Giovinetto and Zwally (2000) visually interpolated accumulation rates from an isopleth map using practically the same field data, but different interpolation criteria, resulting in 1883 Gt a^{-1} and 2326 Gt a^{-1}, respectively (IPCC, 2001). Huybrechts (2000) presented an updated version of Giovinetto and Bentley (1985) with incorporation of new data giving 1924 Gt a^{-1}, and 2344 Gt a^{-1}. The reliability of such estimations suffers not only from a poor spatial coverage of in-situ measurements, but also from an uncertain degree of spatial and temporal validity for each single point observation.

Ice and firn-cores serve as a useful tool because they provide long-term averaged accumulation rates that are not effected by the high temporal and spatial noise on a local scale introduced mainly by wind redistribution. Typical year-to-year variations preserved in firn core stratigraphy were found to range from 30% over the gently sloping plateau area (Sommer and others, 2000) to as high as 250% within the steep escarpment regions (Melvold and others, 1998). On top of such noise longer-term trends in accumulation history may be detected from annual layer-thickness changes within deeper cores. However, if the drilling did not take place on a geographically fixed location, i.e. on an ice dome or summit, the observed accumulation changes over time might be modulated by the horizontal movement of the bore-hole site through a spatial accumulation pattern that is controlled by stationary surface undulations associated with bedrock topography (Melvold and others, 1998; Sommer and others, 2000; King and others, 2004). Therefore, to evaluate the significance of detected temporal trends the

spatial accumulation variability upstream of a bore-hole site should be explored and considered together with the ice-velocity.

Ice-penetrating radar (IPR) studies are recently applied to resolve spatial accumulation variations in high resolution along continuous profiles (e.g. Reeh, 1990; Nereson and others, 2000; Richardson-Näslund, 2004; Spikes and others, 2004). Such information not only give a means to determine how representative the results interpreted from a single firn core are. They also provide valuable ground-truth for satellite radar observations. The interaction of microwaves with snow generates signals that can be linked to snowpack properties like water content, grain size, subsurface layering, or surface roughness (Mätzler, 1987; Rott and others, 1993; Legrésy and Rémy, 1998; Rémy and others, 1992; Jezek and others, 1994; Long and Drinkwater, 1994; Wisman and Boehnke, 1997). Within the dry snow zone, the accumulation rate is seen as a key factor that determines the morphological structure of the snowpack. Consequently, radar backscattering was found to be sensitive to accumulation changes (Forster and others, 1999; Drinkwater and others, 2001; Munk and others, 2003) leading to the central question of this study, whether synthetic aperture radar (SAR) could be utilized to quickly map the spatial accumulation distribution two-dimensionally in high-resolution.

Area of investigation was Dronning Maud Land (DML) within the Atlantic sector of Antarctica that has been under investigation by several nations over the last 50 years resulting in a large body of available literature. Field activities increased in the 1990's in the framework of the International Trans-Antarctic Scientific Expedition (ITASE), established in order to gain a better understanding of Southern Hemisphere climate within the last 200 years, and in the course of pre-site surveys for the European Project for Ice Coring in Antarctica (EPICA), aiming at locating a suitable deep ice-core drilling site in the Atlantic sector of East Antarctica. The later consisted of detailed mapping of the surface and bedrock topography (Steinhage and others, 1999), drilling of shallow and medium-length ice cores in combination with snow-pit studies, to infer the overall spatial accumulation distribution (Isaksson and others, 1999; Karlöf and others, 2000; Oerter and others, 2000), as well as IPR soundings to investigate the small-scale accumulation variability along continuous profiles (Eisen and others, 2004; Eisen and others, 2005). Furthermore, the meteorological conditions in DML were studied by means of automatic weather stations (AWS) (Reijmer and Van den Broeke, 2001; Reijmer and Oerlemans, 2002) and atmospheric modelling (Van den Broeke and others, 2002; Van Lipzig and others, 2002a, b). Taken together all this information provided an excellent basis for this study on spatial distribution of snow accumulation and snowpack properties in DML. Major goal was to compare and integrate results of complementing approaches to determine snow accumulation rates in polar environments.

2 Area of Investigation

These studies are focused on western Dronning Maud Land (DML), located between 20°W and 15°E and between 70°S and 80°S, roughly (Fig. 2.1). This region is of particular interest to glaciological investigations as e.g. the recently finished deep ice-core drilling at Kohnen station carried out in the frame of EPICA. There the meteorological regime reacts very sensitively to conditions over the South Atlantic, possibly providing a connection to northern hemisphere climate records (Stocker, 2003). Major landscape features in DML are the flat ice shelves along the coast, (e.g. Riiser-Larsenisen, Ekströmisen, and Fimbulisen), the escarpment areas Ritscherflya and Hellehallet, as well as the high-altitude plateau regions Amundsenisen and Wegenerisen. Coastal and interior regions are over long distances divided sharply by the mountain ranges of Heimafrontfjella, Kirwanveggen, and Mühlig-Hofmann-Gebirge. Those nunataks penetrate the ice sheet reaching heights of up to 2700 m a.s.l.. Jutulstraumen is the largest ice stream within DML with a catchment basin of approximately 124.000 km². The steadily increasing elevation from the coast towards the interior is associated with a drastic reduction in mean annual air temperature, i.e. from -16.1°C at Neumayer station on Ekströmisen (König-Langlo and others, 1998) down to only –48.3°C recorded on the plateau (75°S, 15°E) at an elevation of 3453 m a.s.l. (Reijmer and van den Broeke, 2001).

Antarctica is surrounded by a zone of sub-polar lows and strong westerlies, i.e. the circumpolar trough, generating cyclones that transport marine humid air masses onto the Antarctic Plateau (Reijmer and van den Broeke, 2001). However, cyclonic systems seldom penetrate far inland due to the elevated terrain of the Antarctic ice sheet. Within the steep escarpment regions and mountain ranges air masses approaching from the sea are forced to rise, resulting in enhanced snowfall (e.g. Bromwich, 1988; King and Turner, 1997; Noone and others, 1999). Deposition of snow was found to be generally accompanied by strong winds, making it difficult to differentiate between snowfall and

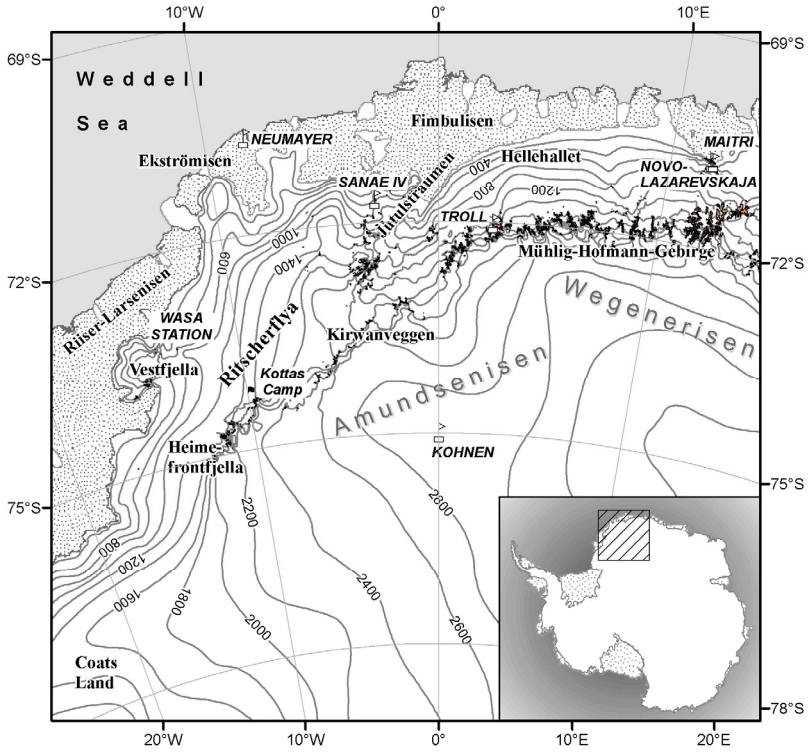

Figure 2.1. Area of investigation, western Dronning Maud Land.

snowdrift (Reijmer and van den Broeke, 2001). As observed by Reijmer and van den Broeke, 2003 using ultrasonic altimeters mounted on AWSs, for coastal areas most of the annual accumulation results from a few major snowfall events with extremes > 90 kg m^{-2} (~27 cm snow) occurring in the escarpment regions. Thereby 50% of the accumulation is deposited in ~7% of the events with large variability in event size. Furthermore, gravity-driven *katabatic* winds with predominant easterly directions form when cold, dense air-masses flow downhill from the interior plateau regions following orographic pathways. Slope and vertical temperature gradient of the moving air layer are the major components influencing the strength of such winds (King and Turner, 1997) that are primarily responsible for sastrugi formation and drift transport of snow. Local topography and associated differences in slope gradients and orientation induce a highly variable surface-wind field, which is the main reason for large regional to local variations in snowfall as well as erosion and re-deposition of snow, i.e. wind redistribution (Melvold and others, 1998; Van den Broeke and others, 1999). The resulting complex accumulation pattern of coastal DML and adjacent escarpment regions is revealed by field observations carried out by several nations over the last 5 decades. Long-term averaged accumulation rates obtained from firn cores vary between 46 kg m^{-2} a^{-1} to 491 kg m^{-2} a^{-1}.

In the Antarctic interior most precipitation is associated with radiative cooling of moist air instead of orographic lifting. Here, little ice crystals fall out as *clear-sky precipitation*, also referred to as *diamond dust*. The annual snow accumulation on the plateau is usually small and occurs in numerous small events, i.e. 75% of the accumulation is deposited in events of < 10 kg m^{-2} (~3 cm snow) (Reijmer and van den Broeke, 2003). Annual accumulation rates revealed by firn core data range from as low as 19 kg m^{-2} a^{-1} at the south-eastern corner of the study area (Picciotto and others, 1971) to 171 kg m^{-2} a^{-1} in the southern vicinity of Mühlig-Hofmann-Gebirge (Isaksson and others, 1999). A spatial trend running from northwest to southeast can be observed corresponding to a general accumulation decrease with increasing distance to the open ocean and elevation, and with decreasing mean annual air temperature, respectively (Giovinetto and others, 1990; Vaughan and others, 1999a). The primary precipitation pattern is modulated by wind-activity in combination with surface undulations leading to preferential accumulation in topographic depressions rather than on crests (e.g. Sommer and others, 2000; Arnold and Rees, 2003; Frezzotti and others, 2005; Karlöf and others, 2005). Such undulations show amplitudes on the metre-scale and wavelengths on the kilometre-scale and have been linked to bedrock morphology (e.g. Budd and Carter, 1971). For the DML plateau wind speeds are moderate with values less than ~5 m s^{-1} on average (Reijmer and others, 2002), also indicated by little surface roughness with wind-shaped features only of small-size (10-15 cm high) (Stenberg and others, 1998). However, during singular events, caused by the advection of warm, humid air-masses, wind speeds may increase to 15 m s^{-1} comparable to the speed of katabatic wind systems (Reijmer and others, 2002). A detailed discussion of weather conditions and related snow accumulation characteristics in DML was presented by Noone and others (1999).

3 Observation of the Cryosphere from Space Using Active Microwave Instruments

This study took advantage of data acquired by active microwave sensors, i.e. radars that measure the returned backscatter from electromagnetic pulses transmitted to the ground. This chapter gives a short overview of satellite techniques and missions applied in this study, i.e. Escat and Nscat scatterometry and Envisat ASAR. Radar principles are addressed and related terms defined as far as concerning this study. For a further description see for instance Ulaby and others (1982), Elachi, 1988, Lillesand and Kiefer (1994), Sabins (1997), Henderson and Lewis (1998). At the beginning a brief introduction is given into advantages and selected applications of radar techniques for cryospheric studies. An extensive summary on most recent technical advances and applications in polar remote sensing, in particular SAR, is given by Massom and Lubin (2006).

3.1 Cryospheric Applications

Spaceborne radar missions are meanwhile well-established in many fields investigating ocean dynamics or land surface properties. Compared to smaller-wavelength optical and infrared systems, microwave sensors offer a number of advantages that make them attractive particularly for land ice and sea ice studies. Most space- and airborne systems operate with frequencies that pass almost unaffected through cloud cover and rain what makes them nearly independent of atmospheric conditions. In consequence, data collection can continue untainted by the frequent ice clouds of Southern oceans or by snow drift over continental ice sheets. Most imaging and scatterometer systems use frequencies below 40 GHz, thereby avoiding a narrow absorption band caused by water vapour at 22 GHz. Common remote sensing radar-band designations are given in Table 3.1. By providing their own "illumination" radar systems become independent from sun light and enable data acquisition day and night what is a major benefit with regard to the long darkness during polar winter. Because of their all-weather, day-night and year-round imaging capability microwave radar sensors have the potential to provide frequent and continuous coverage of any given sector of the Earth, provided that it is included within the sensor's imaging area. Particularly when monitoring short-term phenomena radar sensors are therefore an essential tool. As a further major advantage, system characteristics as frequency, viewing geometry and polarisation can be adjusted to the desired application.

Table 3.1. Band designations for satellite radars (Hall, 1998)

Band Designation	Wavelength λ (cm)	Frequency ν (GHz)
Ka[1]	0.71-1.1	26.5-40.0
Ku[1]	1.67-2.4	12.5-18.0
X	2.4-3.75	8.0-12.5
C	3.75-7.5	4.0-8.0
S	7.5-15.0	2.0-4.0
L	15.0-30.0	1.0-2.0
P	30.0-100.0	0.3-1.0

[1] Ku/Ka - underneath / above 22 GHz

Therefore, spaceborne radar missions play an increasingly important role in cryospheric studies. They have contributed largely to overcoming remoteness and inaccessibility of polar regions by providing valuable information where direct measurements and monitoring of desired parameters are logistically difficult, costly

and/or time-consuming. Such systems support glaciological studies in the first line by mapping and monitoring the extent, volume changes, surface properties as well as individual surface features (e.g. ice-flow lines, crevasses, surface undulations) of the Earth's ice cover. Because of the penetrating capability of microwaves in dry snow and firn, radar images give a different view than visible/near infrared imagery. They have been utilized for retrieving a variety of important geophysical parameters connected to the snowpack, such as water content, density, internal layering, grain size, and surface roughness (e.g. Rott and others, 1993; Rémy and others, 1992; Long and Drinkwater, 1994; Wisman and Boehnke, 1997). Microwave energy emitted or reflected from dry snow was found to be sensitive to the annual snowfall because of its influence on snowpack morphology, in the first line grain size and stratification. This fact has been used earlier to this study to map the amount and distribution of accumulation across the Greenland ice sheet using scatterometry (Drinkwater and others, 2001) and SAR (Forster and others, 1999; Munk and others, 2003). However, a routine satellite retrieval of snow accumulation rates that provides a realistic picture of the spatial variations was not yet developed. Related studies are carried out using passive microwave data (Surdyk and Fily, 1993; Zwally and Giovinetto, 1995; West and others, 1996; Flach and others, 2005). Other selected applications of active microwave systems are summarized in Table 3.2.

Table 3.2. Selected cryospheric applications of active microwave instruments with references

Instrument	*Application*	*Reference*
Scatterometers	Mapping of snow/ice facies	Long and Drinkwater, 1994; Drinkwater and others, 2001
	Sea-ice monitoring	Ezraty and Cavane, 1999; Remund and Long, 1999; Remund and others, 2000; Zhao and others, 2002
	Iceberg tracking	Stephen and Long, 2000; Long and others, 2002; Ballantyne, 2002
	Ice-sheet surface roughness and near surface wind field	Rémy and Minster, 1991; Rémy and others, 1992; Ledroit and others, 1993
SAR	Mapping of glacier boundaries	Rott and Davis, 1993; Adam and others, 1997; Partington, 1998; Demuth and Pietroniro, 1999
	InSAR for ice-sheet surface topography and flow velocity fields	Fahnestock and others, 1993; Joughin and others, 1996; Massonnet and Feigl, 1998; Mohr and others, 1998; Joughin and others, 1999
	Sea-ice monitoring	Drinkwater and others, 1991; Kwok and others, 1992; Rignot and Drinkwater, 1994; Haverkamp and others, 1995; Tsatsoulis and Kwok, 1998
Altimetry	Ice-sheet elevation changes	Van der Veen, 1993, Wingham and others, 1998; Thomas and others, 1999; Davis and others, 2000; Davis and others, 2005; Zwally and others, 2005

3.2 Imaging Principles of Scatterometers and SAR

3.2.1 Imaging Geometry

Spaceborne radar systems transmit microwave pulses and receive backscattered power from the Earth's surface which is recorded together with the Doppler shift of frequency as a function of travel time. The latter precisely determines the *slant range* (R), i.e. the line of sight distance between the antenna and each illuminated ground target, i.e. *scatterer*, when multiplied with the speed of light c (3×10^8 m · sec^{-1}). In opposite, the *ground range* is the true horizontal distance along the ground between scatterer and subsatellite track. The term *range* also refers to the across-track dimension, i.e. in the direction normal to the flight direction of the spacecraft. The term *azimuth* refers to the along-track dimension parallel to the flightline. The radar antenna beam is pointed sideways, typically nearly perpendicular to the spacecrafts flight direction, thereby illuminating a *swath* on the ground with specific width, i.e. the sensors instantaneous *field of view*. This side-looking viewing geometry is typical of air- and spaceborne imaging radar systems. The portion of the image swath closest to the nadir track is called the *near range*, while on the reverse portion there is the *far range*. The incidence angle (θ), defined as the angle between the radar line-of-sight and the surface vertical, increases moving across the swath from near to far range. In the near range, the viewing geometry is referred to as being steep, whereas at the far range it is shallow. In general, the backscattering from distributed targets on the ground decreases with increasing θ. For image interpretation of sloping terrain the *local incidence angle* must be considered because it accounts for effects of the curvature of the earth and local topography. The *look angle* (ϕ) refers the angle between the radar line-of-sight and the vertical of the antenna to the ground. Another term often used is the *depression angle* (γ) which is the complement of ϕ. A radar system is characterized by its depression angle at midpoint of the image swath. The *azimuth angle* is defined as the angle between the flightline and the ground-range direction of the radar beam. Figure 3.1 illustrates the radar viewing geometry.

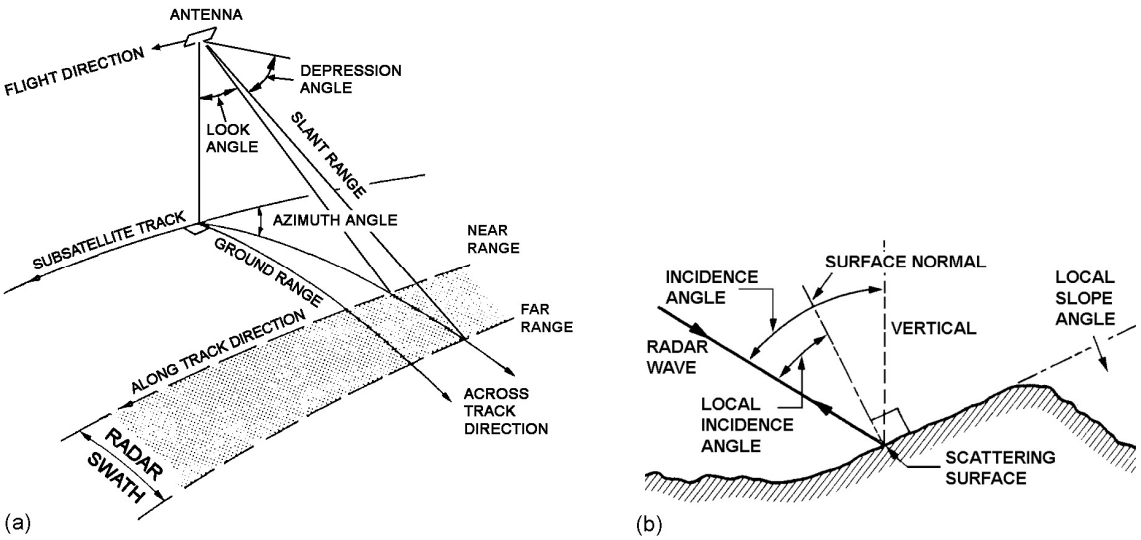

Figure 3.1. Viewing geometry: (a) side-looking radar system and (b) local incidence angle (θ) (modified after Henderson and Lewis, 1998).

The side-looking imaging geometry may lead to a number of distortions within radar image products in dependence on local topography. Slopes facing towards the sensor are shortened (foreshortening) or in extreme cases not resolved (layover). However, if terrain elevation is available by means of a Digital Elevation Model (DEM), those effects can be minimised using image processing routines. For the smooth terrain of the Antarctic ice sheet geometrical distortions play only a minor role and were corrected during the SAR geocoding (Chapter 5.4).

3.2.2 Range and Azimuth Resolution

Two targets on the ground can be resolved, i.e. distinguished as individual features, if their separation distance is greater than the resolution of a radar system. The latter is determined by the systems viewing geometry, wavelength, pulse duration, and antenna size and results from different operational parameters in azimuth and range directions. The ground resolution in range direction (R_r) is a function of depression angle γ and pulse duration Δt according to (e.g. Sabins, 1997):

$$R_r = \frac{\Delta t \cdot c}{2 \cos \gamma} \tag{3.1}$$

Because the depression angle is decreasing with increasing distance to the nadir track, R_r improves from near to far range. Shorter pulses result in finer resolution, which is achieved by a linear frequency chirp, as applied for SAR and altimeter systems. The best attainable time resolution is inversely proportional to the bandwidth B of the transmitted signal with a corresponding slant range resolution as given in Eq. (3.2) (Oliver and Quegan, 1998). E.g. for the ERS SAR system (B = 15.5 MHz) R_s corresponds to 9.68 m.

$$R_S = \frac{c}{2B} \tag{3.2}$$

The azimuth resolution (R_a) for a Real Aperture Radar (RAR) is determined by the radar beam width β_h which is a function of the systems wavelength λ and antenna length l as in

$$\beta_h = \lambda / l \tag{3.3}$$

Since β_h is getting wider with increasing slant range distance R from the sensor, R_a can be determined according to:

$$R_a = \beta_h \cdot R \tag{3.4}$$

Because

$$R = \frac{H}{\cos \phi} = \frac{H}{\sin \gamma} \tag{3.5}$$

where H is the altitude of the sensor, R_a can be expressed as

$$R_a = \left(\frac{H}{\cos\phi} \right) \frac{\lambda}{l} = \left(\frac{H}{\sin\gamma} \right) \frac{\lambda}{l} \tag{3.6}$$

Accordingly, R_a can be improved by using longer antennas and smaller wavelengths. R_a decreases with increasing altitude and from near to far range. For RAR systems operating on satellites, R_a is in the order of several kilometres. As an example, for the ERS satellites with an altitude of 800 km, λ = 5.6 cm (C-band), l = 10 m, and γ = 67° the azimuth resolution would be ~4.9 km, too low for many applications. Synthetic aperture systems synthesize a longer antenna using *Doppler processing* by taking advantage of the relative motion between sensor and target causing a Doppler shift of the observed frequency. While within the SAR's view each location on the ground is pulsed many times, e.g. about 1000 times for the ERS satellites. By recording the signals phase shift together with signal strength and travel time individual scatterers, contributing simultaneously to the radar echo, can be discriminated. This way, a large multi-antenna array is synthesized which equals in size to the distance the satellite travelled while viewing a particular target. R_a is thereby improved to only half the antenna length and becomes independent of slant-range distance:

$$R_a = l/2 \tag{3.7}$$

However, multiple scattering within each resolution cell results in noise within a SAR image product, i.e. *speckle* also referred to as “salt and pepper” texture , caused by a random constructive and destructive interference of individual backscatter signals. In consequence, adjacent ground cells might show dissimilar backscattering efficiency in spite of corresponding surface properties. Speckle reduction can be achieved in three ways: (1) multi-look processing during data acquisition, (2) spatial filtering performed on the output image, or (3) summing and averaging of independent multi-temporal SAR images, provided that surface phenomena did not experience major changes during consecutive data acquisitions.

3.3 Systems and Missions

The interaction of microwaves with the Antarctic snow cover was studied by means of scatterometry and SAR. Those two sensor types differ in their specific system characteristics, e.g. number of antennas, viewing geometry, and spatial resolution. Table 3.3. gives a brief overview of spaceborne radar instruments used in this study together with orbital and instrument characteristics.

3.3.1 Escat and Nscat Scatterometers

Scatterometers are RAR systems, which measure the backscattering from the Earth’s surface with a set of antennas over a wide incidence and azimuth angle range at low spatial but high temporal resolution. Low data rates allow on-board recording and thus a operational capability of up to 100% of the orbit. Scatterometers have been originally

designed to infer near-surface wind speed and direction over the oceans based on empirical models, e.g. described by Lecomte and Attema (1993) for Escat and Naderi and others (1991) and Wentz and others (1984) for Nscat. Ocean surface roughness caused by wind activity, is responsible for an azimuthal modulation of the backscattering, what can be detected using scatterometry. However, from their early beginnings with the NASA/JPL Seasat-A experiment in 1978, scatterometers have been found useful also for broad-scale cryospheric investigations (Long and Drinkwater, 1999). E.g. the variation of radar returns over azimuth angle can be utilized to determine surface roughness and associated dominant katabatic wind direction across an ice sheet (Rémy and others, 1992). One of it's main advantages is the continent wide frequent coverage of polar regions from a variety of perspectives, thus providing a whole set of different looking and incidence angles on a certain ground location. A detailed review of space- and airborne scatterometer experiments, missions and instrumental characteristics is given in Moore and Jones (2004).

Table 3.3. Spaceborne radar missions with orbital and instrument characteristics

Satellite	*Launch*	*Altitude*	*Inclination*	*Period*	*Frequenc y*	*POL*	*Microwave sensors*
ERS-2	20 April 1995	780-785 km	98.5°	100 minutes (~14.3 orbits/day)	5.3 GHz (C-band)	VV	Scatterometer (Escat), SAR
ADEOS-1	17 Aug. 1996	805 km	98.6°	101 min	14 GHz (Ku-band)	VV/HH	Scatterometer (Nscat)
ENVISAT	1 March 2002	799.8 km	98.55°	101 min	5.3 GHz (C-band)	VV/HH	ASAR

The European Space Agency (ESA) launched the Earth Resources Satellites ERS-1/2 in 1991 and 1995, respectively, from Kourou, French Guiana. With a service life of about 8 ½ years for ERS-1 and ERS-2 still operating to the date of writing, these satellites together recorded the longest continuous scatterometer dataset available for long-term studies in many fields. ERS-1 also provided the first wide-spread access to spaceborne SAR data. Due to a tape recorder failure in June 2003 data is now available only for the North Atlantic and a small parts of the Pacific within the reception zone of ESA ground stations. The satellites carried onboard a suite of instruments (Fig. 3.2a), among them the Active Microwave Instrument (AMI) operating in wind scatterometer or in SAR imaging and wave modes. A detailed summary of the ERS-1 satellite concept is provided on the ESA web pages at http://earth.esa.int/ers/satconc/satconc.html.

The AMI operating at a frequency of 5.3 GHz (C-band) combines the functions of a SAR and a scatterometer (Escat) with a set of four antennas (Attema, 1991). The polarization in each case is vertical transmit and vertical receive (VV). The Escat sensor measures the surface backscattering with three right-looking antennas across a single 500 km-wide swath to a southernmost extent of 79.5°S, and with a nominal resolution of 50 km. The three antennas point the beams 45° forward, 90° sideways and 45° backward with respect to the satellite's flight direction with a swath offset of 200 km from the subsatellite track. Covered incidence angles range from 18° to 47° for the mid beam and from 25° to 59° for fore and aft beams, respectively. Fig. 3.2b illustrates the

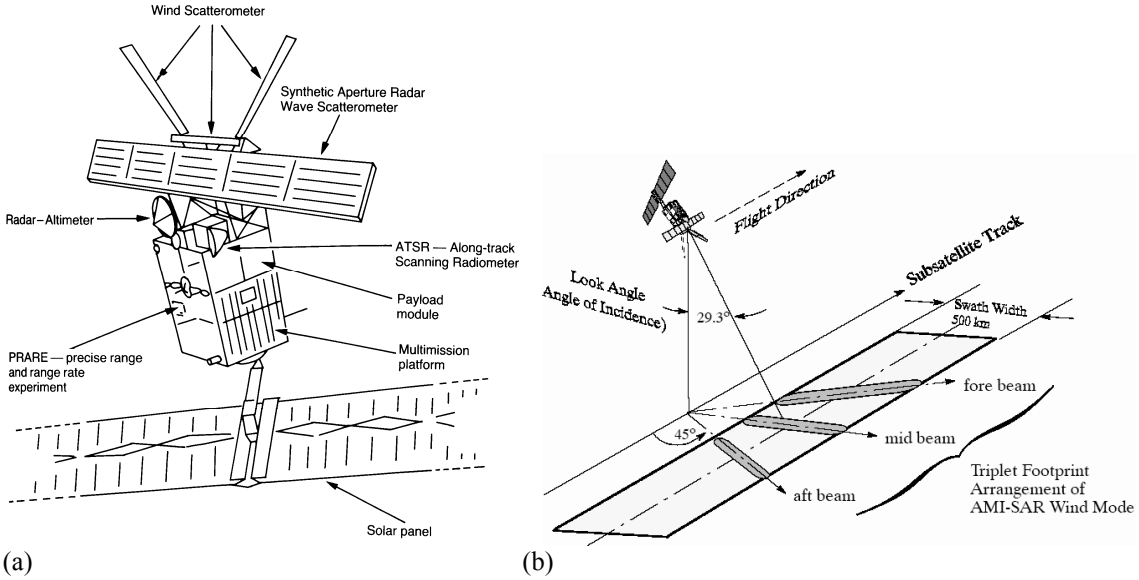

(a) (b)

Figure 3.2. ERS satellites: (a) ERS-1 instruments (Barrett, 1992) and (b) ERS Scatterometer observation geometries (Kramer, 2002).

Escat observation geometry.

Following the ERS missions, the NASA Scatterometer (Nscat) was launched in Aug.1996 on Japan's Advanced Earth-Observation Satellite (ADEOS), later renamed Midori (Fig. 3.3a). The mission ended due to an early spacecraft power system failure in June 1997, after only nine months of operation. The Nscat instrument was the first dual-swath, Ku-band (14 GHz) scatterometer to fly since the Seasat-A experiment in 1978. A full description of this system is given by Naderi and others (1991). The sensor collected backscatter data across two 600-km wide swaths on both sides of the subsatellite track separated by a 400-km wide gap. The sensor was designed to measure the backscatter over land surfaces at 25 km resolution, and retrieve wind vectors over the oceans at 50 km resolution. Its measurement geometry was chosen to meet Nscat's

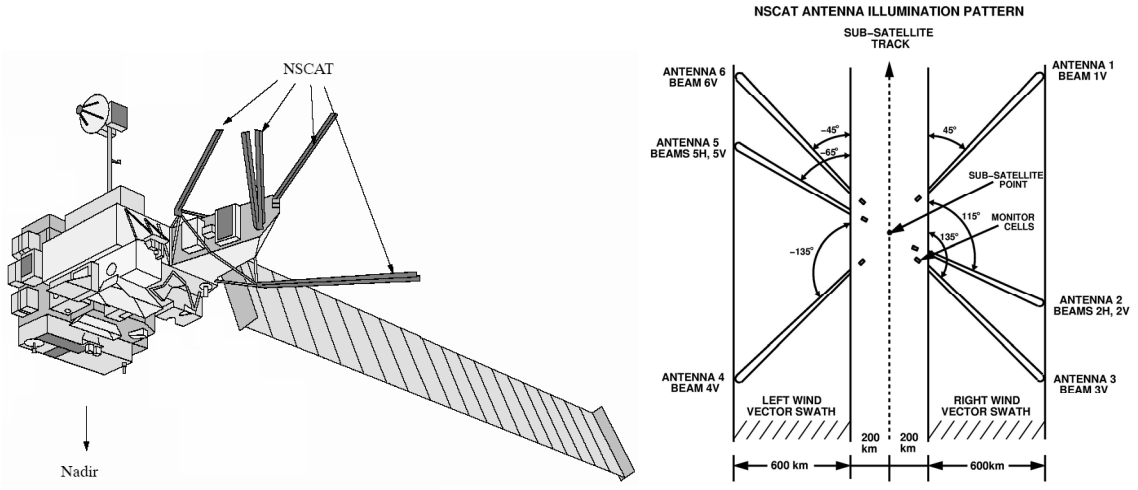

(a) (b)

Figure 3.3. Nscat satellite: (a) Advanced Earth Observing Satellite (ADEOS) general design with Nscat instrument (Kramer, 2002) and b) Nscat beam configuration (Dunbar, 1996).

primary mission of retrieving the ocean's wind field with full coverage every three days. The polar regions were observed several times each day, thereby covering Antarctica to within 1.2° of the pole. Long and others (1993) utilized this rapid repeat coverage to develop resolution enhancement algorithms that increased the efficacy of NSCAT data in polar ice studies. On each side of the instrument, two VV-polarized antennas pointed at ±45° relative to along-track and one dual-polarized mid-beam (VV/HH) pointed at 20° between these directions (Fig. 3.3b). Observations were made over a 17° to 62° incidence angle range.

3.3.2 Envisat Advanced Synthetic Aperture Radar (ASAR)

The ESA ENVIronmental SATellite (Envisat) was launched in March 2002 from Kourou, French Guiana. Operating with the same ground track and frequency as the ERS-1/2 satellites, Envisat ensures the continuity of the AMI image and wave mode observations, but with improved accuracy and ground coverage. Its lifetime is planned to be 5 years. With a number of 10 optical and radar instruments, a launch mass of 8140 kg, and a length of 25 m Envisat is the largest and most complex spacecraft ever build for earth observation. The satellite design is shown in Fig. 3.4. For further technical details of instruments see ESA webpages at http://www.envisat.esa.int/instruments.

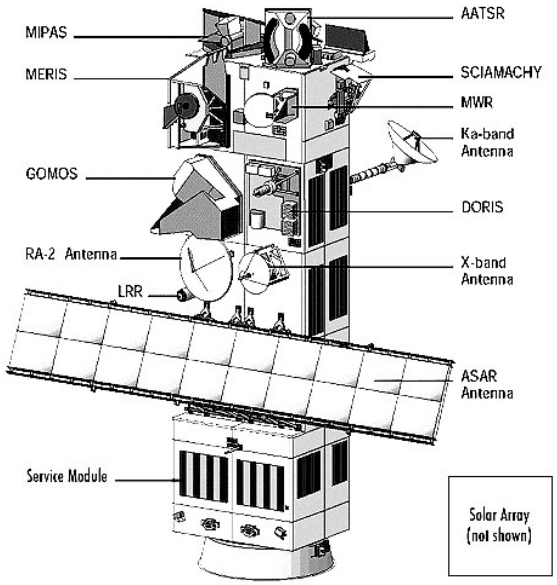

Figure 3.4. Envisat instruments with ASAR sensor. (31Hhttp://www.envisat.esa.int/instruments/tour-index/).

Envisat's largest single instrument is the dual-polarized C-band Advanced Synthetic Aperture Radar (ASAR). The name "Advanced" SAR refers to the ability to select various swath widths, resolutions and look angles from a number of 5 beam modes made possible by radar beam elevation steerage (similar to RADARSAT ScanSAR techniques). On user request ASAR operates in high (IM, AP, WM), medium (WS), and reduced (GM) resolution. For each mode up to 7 subswaths are selectable within a viewing area of ~485 km. Nominal characteristics of the five ASAR principal operating modes are summarised in Table 3.4. The operation modes are divided into two categories: (1) low data rate Global Mission Modes (GM and WM) with systematic on-board recording and operational capability of up to 100% of the orbit and (2) high data rate Regional Mission Modes (IM, AP, WS) with operation time up to 30 minutes per orbit. The latter are transmitted in real-time or after using on-board recording as a buffer either under visibility of an ESA station on a direct X-band link or via the Artemis Ka-band link using the Artemis Data Relay Satellite to the ESA ESRIN Station in Italy. The lower resolution modes are valuable for monitoring broad-scale phenomena in high temporal resolution. ASAR Wide Swath and Global Monitoring Mode provide near daily revisit capability for polar regions.

Table 3.4. Nominal ASAR operating modes and imaging characteristics

Mode	*Image Mode (IM)*	*Wide Swath (WS)*	*Alternating / Cross Polarisation (AP)*	*Wave Mode (WM)*	*Global Monitoring (GM)*
Swath Width	up to 100 km 7 subswaths	≥ 400 km 5 subswaths	up to 100 km 7 subswaths	5 km vignette 7 subswaths	≥ 400 km 5 subswaths
Spatial Resolution	≤ 30 m	≤ 150 m	≤ 30 m	≤ 10 m	≤ 1000 m
Radiometric Resolution	≤ 2.5 dB	≤ 2.0 dB	≤ 3.6 dB	≤ 2.3 dB	≤ 1.6 dB
Polarisation	VV or HH	VV or HH	VV/HH, VV/HV or HH/HV	VV or HH	VV or HH
Data rate	≤ 100 Mbit/s	≤ 100 Mbit/s	≤ 100 Mbit/s	0.9 Mbit/s	0.9 Mbit/s
Mission	regional	regional	regional	global	global

4 Snowpack – Microwave Interaction

For understanding the potential of active microwave instruments for sensing snowpack properties, the ruling factors of the snowpack-microwave interaction must be considered. In this chapter fundamental relationships between physical snowpack properties and associated backscatter characteristics are summarized. Section 4.1 gives an overview of processes that govern snowpack morphology and its spatial variation across an ice sheet. Section 4.2 introduces the normalized radar cross section σ^0, which is the primary parameter for the description of the backscattering principles in section 4.3. For more detailed information on microwave properties of snow see e.g. Ulaby and others (1982), Hallikainen and Ulaby (1986), Mätzler (1996, 1998), Mätzler and Wiesman (1999), West and others (1996).

4.1 Snowpack Morphology

An ice sheet is successively build up by individual layers of snow that gradually turn into firn and ice while being buried and compressed over time by the pressure of newly deposited material as well as by *recrystallization* (Gow, 1969). Physical properties of such layers vary depending basically on accumulation rate and atmospheric conditions, i.e. wind velocity, solar radiation and air temperature, during and shortly after deposition. Those influencing factors show seasonal variations that are preserved in the snowpack in the form of a typical sequence of grain size and density changes, i.e. *seasonal layering*. According to Repp (1978) within coastal DML a typical annual cycle consists of a high-density, wind-packed winter layer with fine grains alternating with a low-density, coarse-grained summer layer. Intensified grain growth dominated by vapour transport processes occurs in the upper snow layers during summer driven by temperature gradients within the snowpack induced by solar radiation. At firn depths of

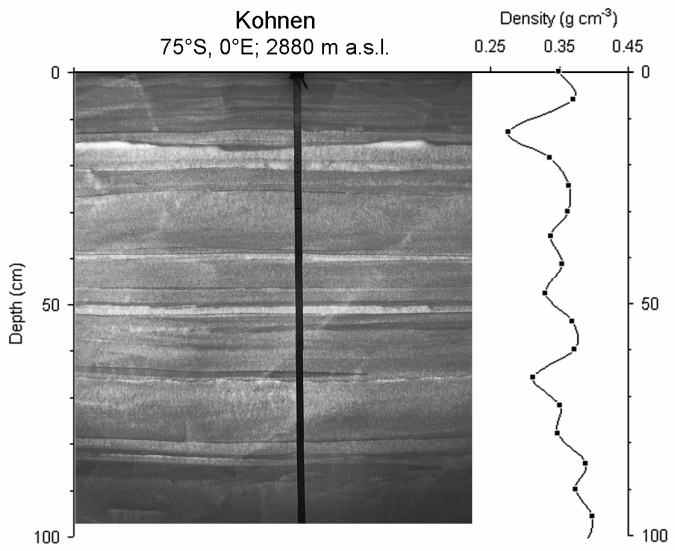

Foto: Jochen Schmitt

Figure 4.1. Snowpack morphology and depth-density distribution near Kohnen station.

>10m the seasonal temperature cycle is largely damped out and grain growth is controlled by sintering mechanisms (Gow, 1969). The density contrast between summer firn and winter firn decreases with depth because of settling and compression, i.e. *densification*, taking place over time. In consequence, the annual firn layers are thinner at greater depths. Typically the surface density is about 300-400 kg m^{-3} increasing to about 500-600 kg m^{-3} at 10 m depth (Gerland and others, 1999; Oerter and others, 1999). Pronounced density contrasts within the snowpack might result from heavy storms causing thin wind-glazed surface crusts and associated formation of depth hoar layers, preferably on the crests of large surface undulations (Gow, 1965). Because of a lower albedo the opaque wind crusts absorb more solar energy than a snow surface. According to Frezzotti and others, 2004 this is causing a warming of the subsurface snow layer, initiating an upward transport of water vapour, sublimation of vapour, and the growth of loose depth hoar ice crystals below the crust. Another feature within the snowpack might result from intense insolation, melting a thin film over the snow surface (~0.5 mm thick), referred to as *sun* or *radiation glaze* (Goodwin, 1991).

In the interior regions, where annual accumulation rates are very low, the burial rate is much smaller. Individual years might miss accumulation totally. Consequently, accumulated snow is exposed much longer to seasonal temperature-gradient effects. As a result of long-lasting metamorphism, snow grains grow larger in the upper snow layers (Partington, 1998; Legrésy and Rémy, 1998) and individual layers of depth hoar tend to merge into a single thick layer (Gow, 1965). The accumulation of only thin annual layers and the frequent development of sun and wind glaze are responsible for an intensified stratification, i.e. a higher number of strata per depth unit. For example, from traverse studies within the Antarctic interior Surdyk and Fily (1993) found the number of strata within the upper 2 m to reach up to 60, with an average of 35. Snow pit studies provide information on density variations with depth and number of strata within the upper few meters of a snowpack. Figure 4.1 gives an impression of snowpack morphology and depth-density distribution within the upper one meter at Kohnen station (75°S, 0°E; 2893 m a.s.l.) showing an intense stratification on the scale of centimetres. Detailed discussions of snow pit stratigraphic studies have been given by e.g. Alley (1988), Gow (1965), and Picciotto and others (1971).

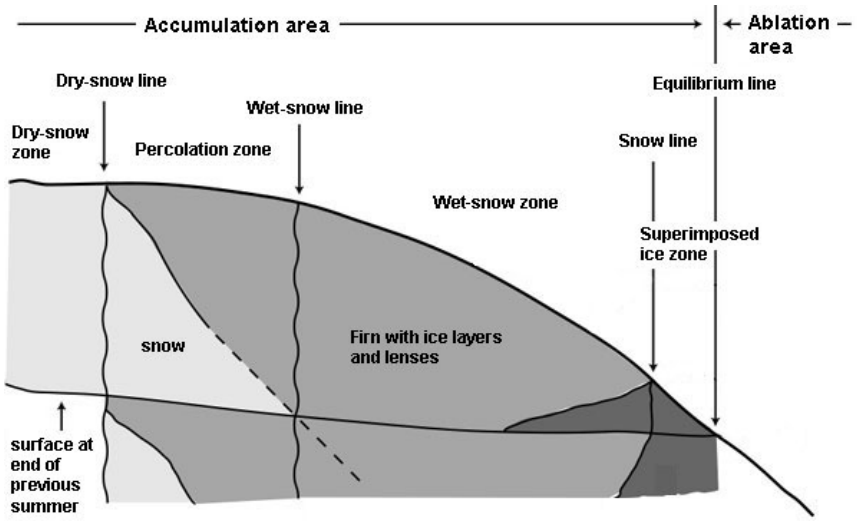

Figure 4.2. Ice/snow facies as illustrated by Paterson, 1994.

Steadily decreasing summer temperatures with increasing elevation from the coastal margins to the elevated interior regions result in the development of physical snow zones or "facies" with zonal alignment across an ice sheet (Fig. 4.2). The boundaries between such snow facies are defined with respect to maximum summer-melt conditions (Benson, 1962; Paterson, 1994). The highest elevation limit of surface melt is marked by the *dry-snow line*. At higher regions the snowpack remains completely frozen throughout the entire year, forming the *dry-snow zone*. Moving downwards from the dry snow line, melt-water percolation occurs first localized in little amounts, but constantly increasing with mean summer temperatures near 0°C until a complete saturation of the annual accumulation layer takes place. As long as the latter is neither completely wetted nor raised to the melting point it is part of the *percolation facies,* characterized by refrozen melt water in the form of ice lenses and ice pipes permanently buried within the snowpack. In winter such melt features act as strong scatterers for microwaves. Below the *saturation line* (wet-snow line) there is the *soaked facies* (wet-snow zone) with its lower margin defined by the *snow line* delineating it from the region in which summer melting removes the entire annual snow accumulation thereby exposing glacial ice, i.e. the *superimposed ice zone*. Due to its very cold climate the Antarctic ice sheet is dominated by the dry-snow zone with the percolation zone forming only a narrow belt along the coastline. Patches of wet-snow zone and superimposed ice zone occur only in small areas.

Furthermore, local topography, i.e. surface slope and orientation with respect to dominant surface winds, introduces spatial variations in snow-pack genesis and in consequence, the formation of certain *snow-pack types* within the dry-snow zone. Due to their snow-penetrating capabilities microwave are sensitive to both, surface as well as subsurface characteristics giving a means to map the extent and variations of snow facies and snowpack types across an ice sheet (Jezek and others, 1994; Long and Drinkwater, 1994).

4.2 Normalized Radar Cross Section (σ^0)

Surfaces with a roughness on the order of microwave radar wavelengths will rather scatter than reflect the incoming signals. The term *backscatter* refers to the amount of energy of a radar pulse that is redirected back towards the sensor from a distributed

target on the ground. The backscattering includes all processes by which backscatter is formed. Other portions of the incident radar energy may be scattered away from the radar or absorbed. The radar equation provides an explanation for system and target related properties that determine radar power return (Henderson and Lewis, 1998). The energy P_r of a radar echo returned from an assumed isotropic point target without absorption and with a slant range distance R from the antenna can be calculated according to (Ulaby and others, 1982)

$$P_r = P_t \cdot \frac{G^2 \cdot \lambda^2}{(4\pi)^3 R^4} \cdot \sigma \quad [\mathrm{W}] \tag{4.1}$$

where P_t is the instantaneous peak transmitter power in Watt, λ the radar wavelength, σ the backscattering cross section of the target in m², and G is the antenna gain. The latter describes how well the antenna beam is focused compared to an isotropic radiator and is defined as

$$G = 4\pi \cdot A_A / \lambda^2 \tag{4.2}$$

with A_A the antenna cross section. In Eq. (4.1) σ characterizes the backscattering efficiency of an isotropic scatterer with reflectivity $\rho = 1$. The scattering from a real target, however, is usually anisotropic and involves absorption. Its true cross section will therefore mostly be larger than σ to generate the same amount of backscattered energy P_r. In remote sensing of the Earth the focus is usually on surface properties rather than on single targets. Therefore, σ is usually normalized with respect to a unit area on the horizontal ground plane, A_G in m², giving the *normalized radar cross section* σ^0, also referred to as the *backscattering coefficient*. The latter is a measure for the average reflectivity of a specific radar ground resolution cell defined as per unit area on the ground:

$$\sigma^0 = \frac{P_r}{P_t} \cdot \frac{(4\pi)^3 R^4}{G^2 \cdot \lambda^2 \cdot A_G} \tag{4.3}$$

Since $A_G = R_a$ x R_r and according to Eqs. (3.1), (3.3) and (3.4) σ^0 can be calculated as in

$$\sigma^0 = \frac{P_r}{P_t} \cdot \frac{2(4\pi)^3 R^3 \cdot l \cdot \cos\gamma}{G^2 \cdot \lambda^3 \cdot c \cdot \Delta t} \tag{4.4}$$

Measurements of σ^0 are usually given on a logarithmic scale with σ^0 (dB) = 10log(σ^0). Off-nadir radar measurements ($\theta \geq 15°$) of natural surfaces usually result in negative σ^0 (dB) values. σ^0 (dB) can be a positive number if there is a focusing of backscattered energy towards the radar antenna, e.g. in case of a corner reflector, rough water surfaces or refrozen firn in the percolation zone.

The image mosaic in Fig. 4.3 shows σ^0 measurements of Antarctica and the surrounding sea-ice cover, with data acquired by the Envisat ASAR instrument working in Global Monitoring Mode (GM) during April and May 2004. The white circle in the centre of the image is where no data was collected due to Envisat's orbital and sampling

geometry. Areas which scatter more energy appear brighter in the image. In winter the brightest region is the percolation zone forming a belt of very high σ^0 at the margins of the continent due to intensive backscattering on refrozen melt features in the form of

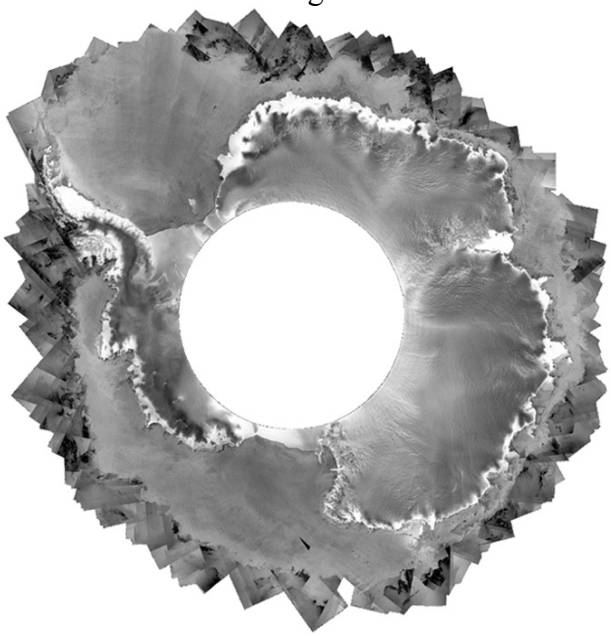

Figure 4.3. Envisat ASAR mosaic of Antarctica acquired during April and May 2004. (32Hhttp://www.esa.int/esaEO/SEMRB9BWC4E_planet_1.html).

buried ice lenses and pipes within the snowpack (Long and Drinkwater, 1994). A lower level of radar backscattering is typical for high accumulation areas within the dry-snow zone, whereas low accumulation results in higher σ^0 due to increased stratification and development of thick depth hoar layers.

The relative brightness can be utilized to trace spatial accumulation variations as done in this study. The image reveals spatial variations in backscattering due to changes in snowpack morphology, i.e. density, subsurface layering, grain size, water content or surface roughness (Rott and others, 1993; Wismann and Boehnke, 1997; Jezek and others, 1994; Legrésy and Rémy, 1998; Long and Drinkwater, 2000; Drinkwater and others, 2001). Reasons for that are treated in the following chapters.

4.3 Snow as Scattering Media

4.2.1 Dielectric Properties of Snow

Snow is an inhomogeneous medium consisting of ice particles, air, and if wet, liquid water. The propagation of electromagnetic waves through a snowpack is governed by the number of internal reflectors, grain size and dielectric properties. The latter are usually described by the dielectric constant or *permittivity*, $\varepsilon = \varepsilon' - i\varepsilon''$, where ε' is the ordinary relative permittivity and the imaginary part $i\varepsilon''$ is the dielectric loss factor of the medium. The higher the dielectric constant, the higher the reflectivity of a medium. For snow the permittivity is primarily a function of frequency, snow wetness, temperature, and density. For *dry snow* ε_{ds} is a function of snow density and of the dielectric constants of air ($\varepsilon_a = 1$) and ice. For frequencies from 1 MHz to well above

the microwave region $\varepsilon_{ice} = 3.17 \pm 0.07$ (Hallikainen and Ulaby, 1986). From empirical studies Tiuri and others, 1984 found the ε'_{ds} to be nearly independent of frequency and temperature within the microwave region. Therefore, ε'_{ds} is governed by density ρ_s. Widely used relations between snow density and ε'_{ds} are:

$$\varepsilon'_{ds} = 1 + 1.7\rho_s + 0.7\rho_s^2 \qquad \text{Tuiri and others, 1984} \qquad (4.5)$$

$$\varepsilon'_{ds} = 1 + 1.60\rho_s + 1.86\rho_s^3 \qquad \text{for } \rho_s < 0.45 \text{ gcm}^{-3} \qquad \text{Mätzler, 1996} \qquad (4.6)$$

Dielectric loss of ice and dry snow are very small, but increase with increasing temperature and density whereat ε''_{ds} can be written as in Eq. (4.7). ε''_{ice} is usually approximated with 8×10^{-4} (slightly impure ice at –20°C, at 2 GHz).

$$\varepsilon''_{ds} = \varepsilon''_{ice}(0.52\rho_s + 0.62\rho_s^2) \qquad \text{Tuiri and others, 1984} \qquad (4.7)$$

The situation is totally different for wet snow, which is highly *absorptive* since ε''_{ws} increases considerably due to the presence of liquid water (Ulaby and others, 1982). For that reason, only radar measurements of the Antarctic snow cover taken during winter, when the snowpack is completely frozen, were used in this study.

4.2.2 Snowpack Surface and Volume Scattering

When the radar signals interact with ground surfaces, they can be reflected, scattered, absorbed, or transmitted. In general, microwave backscattering occurs where ε changes at dielectric interfaces, such as the boundary between adjacent layers or the air-ice interface of ice grains within the volume of each layer (Drinkwater and others, 2001). The total backscatter is the sum of surface scattering at the air/snow interface and of volume scattering at internal layer boundaries, larger grains or grain clusters, and buried melt features within the snowpack. Surface scattering is determined by surface roughness, which is defined in terms of system wavelength and incidence angle according to the *Fraunhofer criterion*:

$$h < \frac{\lambda}{32\cos\theta} \qquad \text{for a smooth surface, and} \qquad (4.8)$$

$$h > \frac{\lambda}{32\cos\theta} \qquad \text{for a rough surface.} \qquad (4.9)$$

where h is the standard deviation of surface height for a random surface (Ulaby and others, 1982). Little backscattering is to be expected from a smooth surface because of a specular reflection of the radar signal away from the satellite. The rougher the surface, the stronger the radar backscatter return. E.g. for Escat C-band (λ = 5.66 cm, θ = 18°-59°) and Nscat Ku-band (λ = 2.1 cm, θ = 17°-62°) the threshold for a smooth or rough surface ranges across the swath from 0.18-0.34 cm and from 0.07-0.14 cm, respectively. Consequently, a polar snow surface can generally be considered rough for both frequencies. Floricioiu and Rott (2001) estimated the scattering at the air–snow interface σ_{vv}^{0as} of several alpine snowpack type using the single scattering term of the integral equation model (IEM) (Fung and Chen, 1992) for L-, C- and X-band assuming

a random rough surface. According to their findings, the surface scattering plays only a minor role within the incidence angle range of our observations (θ > 20°). Therefore, surface scattering was not considered in this study.

For a *dry snowpack* the largest portion of the incoming radar signal is volumetrically scattered back to the antenna. Volume scattering increases with number of strata per depth unit and grain size as illustrated in Fig. 4.4. Since the snow accumulation rate determines both, grain size and stratification via layer thickness, spatial accumulation changes might be inferred from backscattering patterns within a radar image. Since within the dry-snow zone regions with low accumulation show larger grains and more distinct stratification, this should result in stronger backscattering and vice versa (Drinkwater and others, 2001). For the interpretation of radar images, an estimate about the volume contributing to the measured signal strength is vital, but difficult to obtain because of the complexity of the scattering mechanisms.

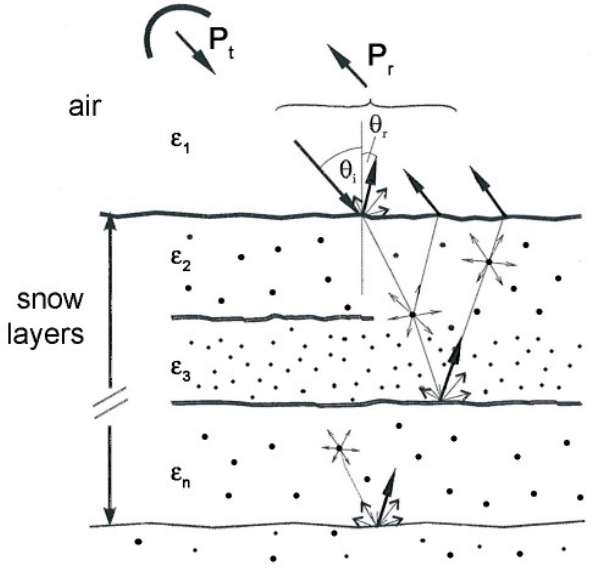

Figure 4.4. Dry-snow backscattering processes.

The p*enetration depth* (d_p) for a dielectric medium is defined as the depth below the surface by which an incident electromagnetic wave is damped to 1/*e* of its initial power (~37 %). For a snowpack the ruling factor of d_p is liquid water content beside frequency, layering, density and grain size. E.g. for melting snow with liquid water content of about 5% by volume d_p is of the order of one wavelength only (Rott and Sturm, 1991). The penetration depth is related to the volume extinction coefficient k_e by

$$d_p[m] = k_e^{-1} \tag{4.10}$$

where k_e is the sum of volume absorption and volume scattering coefficients k_a and k_s. The penetration depth can be estimated for media with $i\varepsilon'' << \varepsilon'$ by (Stiles and others, 1982):

$$d_p \cong \frac{\lambda_0 \sqrt{\varepsilon'}}{2\pi\varepsilon''} \tag{4.11}$$

If taking into account only scattering processes at snow grains, Eq. 4.11 would be valid for dry snow at frequencies below 10 GHz, where particles are significantly smaller than the wavelength (Ulaby and others, 1982). However, due to reflections at internal density boundaries and grain-clusters the scattering loss may become significantly larger also for low frequencies. In this case Eq. 4.11 can be taken as the upper limit of the penetration depth. For dry polar firn d_p at C-band is in the order of tens of meters (Partington, 1998; Bingham and Drinkwater, 2000) and 6-7 m at Ku-band (Legrésy and Rémy, 1998). From field measurements within the dry-snow zone of DML with p=0.435 g cm^3 d_p was found to be in the order of 20 m at 5.2 GHz (k_e = 0.046 m^{-1}) and 8 m at 10.3 GHz (k_e = 0.123 m^{-1}), respectively (Rott and others, 1993). For wet snow the influence of volume scattering can be neglected since k_s << k_a in the GHz region.

The volume scattering was estimated for alpine snow covers by Floricioiu and Rott (2001) using a first-order model with permittivity and extinction properties of dry snow (ε', ε'', κ_e, κ_s, κ_a), which were calculated based on the dense medium transfer theory (Wen and others, 1990) for VV polarization by

$$\sigma_{vv}^{0vol} = 0.75\omega\cos\theta_i\left[1-\exp\left(-2k_e d/\cos\theta_t\right)\right] \tag{4.12}$$

where ω is the single scattering albedo and d the snow depth. The assumption of Rayleigh scattering is valid for frequencies below 15 GHz if grain size is below 5 mm (Ulaby and others, 1981). According to snow pit studies, grains as large as this value have not been observed in DML. The total backscatter from a deep snowpack with uniform density calculates as $\sigma_{vv}^{0tot} = \sigma_{vv}^{0vol} + \sigma_{vv}^{0as}$. According to (Wen and others, 1990) the volume scattering of dry snow is controlled by the size of snow grains. Using typical grain size field observations as model input the magnitude of backscattering differences between Ku- and C-band can be explained. However, as snow stratigraphy is not considered, the absolute value of backscattering is underestimated. In order to obtain more realistic estimates of the backscattering of deep dry snowpacks, density-stratified layers have to be considered in model calculations (West and others, 1996; Flach and others, 2005). Because of the complex structure of the snowpack and the difficulties in parameterising its properties, satisfying numerical models on backscattering are still pending. Attempts to model the relationship between backscatter, grain size and accumulation rates have been made by Forster and others (1999), Drinkwater and others (2001), Munk and others (2003), and Flach and others (2005) with promising results for the Greenland dry-snow zone. A better understanding of the physical processes and extensive model validation using in-situ data, is required to obtain improved model results.

4.2.3 Viewing Angle Dependency of Backscattering

A change of the radar viewing angle usually affects the radar backscattering behaviour of a surface because different scattering mechanisms may occur in different angular regions. In general, reflectivity from distributed scatterers decreases with increasing incidence angle, i.e. from near to far range, with a lower rate of decrease for rougher surfaces (Sabins, 1997). In case of Envisat wide swath images the change of incidence angle for flat terrain across the imaging swath is about 20°. In scatterometry a larger number of possible incidence angles is covered by the antenna systems (Nscat: θ

= 17°-62°, Escat: θ = 18°-59°). For complex terrain with varying surface slopes and roughness features the local incidence angle might vary significantly between different portions of an image. For a polar ice sheet, the backscattering is affected by wind-generated surface roughness with heights on the decimetre-scale, likely also preserved within the snowpack. According to Frezzotti and others (2004) snow transportation starts at wind speeds of about 5 m s^{-1}, whereat wind speeds less than 15 m s^{-1} produce transverse depositional features such as ripples, waves and barchans, while those greater than 15 m s^{-1} produce longitudinal features such as dunes and sastrugi.

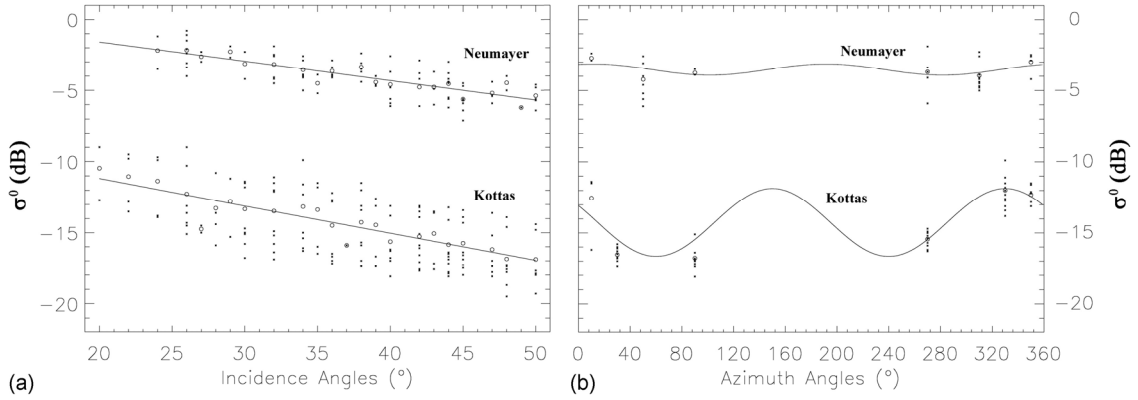

Figure 4.5. Escat scatterometer measurements during a 35-day acquisition period (May 28 to June 30, 1997) corresponding to the locations of Neumayer station (70°39'°S, 8°15'E) and Kottas Camp (74°12'S, 9°44'W): (a) σ^0 versus incidence angle averaged over all azimuth angles and (b) σ^0 versus azimuth angle within the incidence angle range of 30-40°. Single measurements are given as black dots; mean value as a circle.

In this study the angular dependence of backscattering was investigated by means of scatterometer data collected at C- and Ku-band. Following Rott and others (1993) the incidence angle gradient (*IG* in dB deg^{-1}) and the factor of anisotropy (*FA*) have been calculated as lined out in chapter 5.4. For example, in Fig. 4.5 Escat data obtained for the surrounding area of Kottas camp (74°12'S, 9°44'W) within the DML dry-snow zone and for Neumayer station (70°39'°S, 8°15'E) situated on the flat Ekström Ice Shelf within the percolation zone is presented in graphs of σ^0 (dB) versus incidence and azimuth angle, respectively. It can be seen that the backscattering within the percolation zone is more intense due to larger grains within the summer layers combined with buried melt-features. At the same time σ^0 at Neumayer is less dependent on viewing angles than at Kottas camp. Being located within the steeper escarpment region in the vicinity of Heimefrontfjella mountains, the latter area is affected by strong katabatic winds causing the formation of large erosional sastrugi, primarily affecting the azimuthal modulation of the backscattering coefficient. Concerning *IG*, for the incidence angle range covered by the Envisat ASAR sensor (θ = 18°-40°), the decrease of σ^0 with increasing θ would be in both cases the order of several dB.

In order to correlate the Envisat ASAR derived σ^0–measurements with in-situ accumulation data, such viewing angle effects needed to be removed prior to the analysis. Normalization of the ASAR data to uniform incidence (35°) and azimuth angle (0°) was carried out by making use of the information on viewing angle dependencies obtained by Escat derived parameters *FA* and *IG* as described in chapter 5.4. An example is given in Fig. 4.6c showing a transact of σ^0 measurements across track from near to far range prior to and after incidence angle normalization.

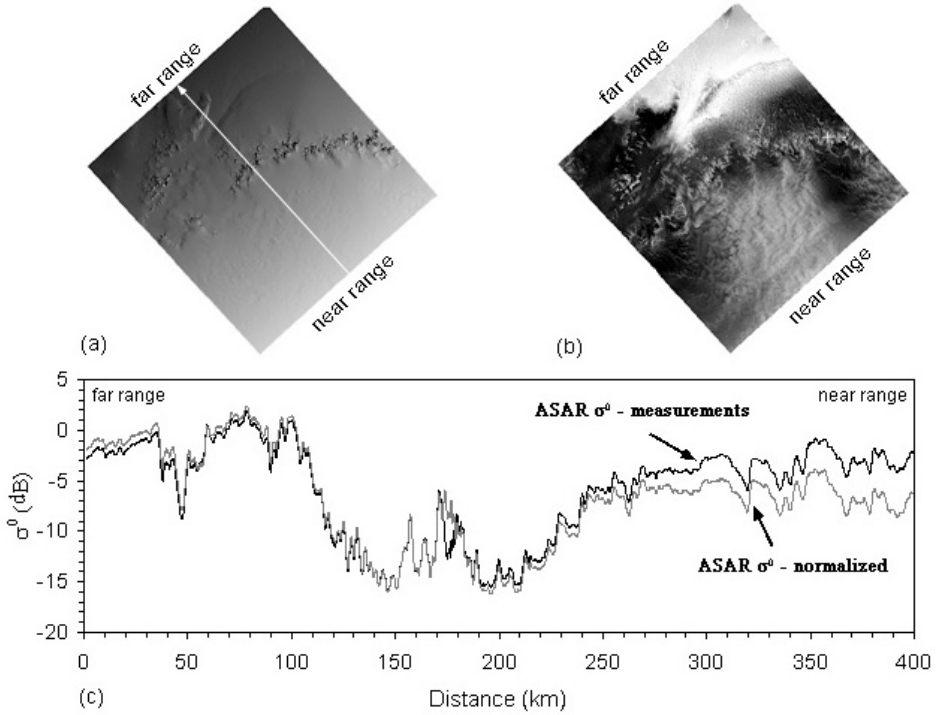

Figure 4.6. Incidence angle normalization for ASAR frame 5148, track 206, orbit 10781, acquisition date: 2004/03/23 (center coordinates: 72°20'S, 02°07'E). Visible are the Northern Amundsenisen / Jutulstraumen region as well as Kirwanveggen and Mühlig-Hofmann mountain ranges (see also Fig. 2.1): (a) Local incidence angle image, (b) Envisat ASAR WS image normalized to uniform 35° incidence angles and (c) comparison of σ^0 measurements prior to and after incidence angle normalization along transect from near to far range (white arrow in Fig. 4a).

5 Data and Methods

This chapter provides a brief introduction to data and methods used in this study. For satellite data the method part is covered extensively by chapter 3. Main processing steps and related software are summarized thereafter in chapter 5.4.

5.1 Firn Cores, Snow Pits and Stake Readings

Within an ice sheet, various physical and chemical parameters are stored that can be related to climate history (e.g. Jouzel and others, 1993). Firn and ice core drilling is used to access such information and to provide point accumulation records at the same time. The latter serve as key input to ice-sheet mass-balance estimates, ground truth for satellite observations, and, when interpolated over wider areas, reveal the broad-scale surface mass-balance variability within an region. Because they average the annual accumulation over longer time periods, firn-core data are less sensitive to the high spatial and inter-annual variability in snow deposition mainly due to wind activity (e.g. King and others, 2004; Frezzotti and others, 2005; Karlöf and others, 2005). They can therefore be considered to be temporally and spatially better representative than other point data such as snow pits, stakes and thermistors. Also local changes in accumulation rate over time can be reconstructed from changes in annual layer thickness of a firn

core, providing a means to look back into accumulation history over several decades up to millennia. However, if their position was not located on an ice dome, apparent temporal trends might be effected by the movement of a bore-hole site through a complex accumulation pattern related to bedrock topography upstream of a drilling site (Gow and Rowland, 1965; Melvold and others, 1998; Sommer and others, 2000).

In order to establish depth-age scales for firn and ice cores, accurate dating must be carried out by annual layer counting, based on multiple seasonally varying parameters, i.e. chemical compounds (e.g. Ca^{2+}, Na^{+}, SO_4^{2-}, NH_4^{+}, and NO_3^{-}), isotope ratios ($\delta^{18}0$ and δD), and mineral dust. For this the annual accumulation rate must be sufficiently high. e.g. >0.07 m ice a^{-1} for continuous flow analysis (CFA) measurements (Urs Ruth, pers. comm.). Dating is supported by absolute time markers that can serve as reference horizons. Well-known historic volcanic layers are usually used for this purpose, identified within the ice column by elevated sulphate concentrations or enhanced electrical conductivity using the electrical conductivity method (ECM), dielectric profiling (DEP) or CFA. Other stratigraphic-time horizons are deposition layers of radioactive fallout from atmospheric nuclear weapons tests, detected by β-activity or tritium measurements. Given the age and depth to such reference horizons, the average accumulation since deposition can then be calculated from integration of local depth-density profiles, as well provided by firn core data.

Within the upper soft layers firn cores are usually supplemented by snow pits that allow detailed studies on snow morphology, i.e. the stratigraphic distribution of internal summer and winter layers of varying density, depth-hoar, ice lenses as well as the specific grain size. Such information is urgently needed as ground-truth data for the analysis and interpretation of remotely sensed satellite observations within the microwave region. Investigations of small-scale spatial accumulation variations are traditionally carried out by repeated measurements of snow depth along a number of stakes. Also here, the calculation of accumulation rates depends on some assumption for the snow density within the upper few meters, provided for instance by density profiles of nearby snow pits.

For this study, shallow and medium depth firn-core and snow-pit data was used that was obtained mainly over the last 15 years by several European nations, in the first place during a number of EPICA pre-site surveys carried out in the 1990s. For a region wide interpolation of accumulation point data, those records were supplemented by earlier data taken from literature. Together they cover a wide variety of accumulation time periods, ranging from several years to several hundreds of years (as listed in detail in the Appendix of Paper III). Stake data originated from a line of 675 stakes at 500-m intervals set up along a traverse route leading from the German Neumayer station (70°39'S, 08°15'W) located on Ekströmisen to the German Kottas camp (74°12'S, 9°44'W), with annual readings carried out between 1999 and 2001.

5.2 Ice-Penetrating Radar Data

Ice-penetrating radar (IPR) soundings of internal horizons in the upper layers of polar ice sheets have the potential to provide long-term averaged accumulation data along continuous profiles (e.g. Richardson and others, 1997; Nereson and others, 2000; Pälly and others, 2002; Eisen and others, 2005). Therefore, IPR can be utilized to investigate spatial accumulation variations in high-resolution, providing a means to quantify to what degree a single point measurement (e.g. obtained from a firn core) within the same region can be considered representative for its surrounding. Operating

with longer waves at radio frequencies the radar signals can penetrate the upper hundreds of meters of the ice column, corresponding to several hundreds to thousands of years of accumulation history on the Antarctic inland plateau (Eisen and others, 2005). Distinct reflections horizons visible within the radar stratigraphy are considered to represent historical surfaces of equal age, i.e. isochrones (Gudmandsen, 1975; Hempel and others, 1993; Vaughan and others, 1999b; Frezzotti and others, 2002; Vaughan and others, 2004). Such features may result from periods with exceptional climatic or atmospheric conditions, such as intense storms, extremely high insolation, high temperatures or deposition of impurities (Richardson and others, 1997), leaving pronounced dielectric contrasts in the ice column. Within the upper hundreds of meters (~500-1000 m) reflections were found to be dominated by ice-density variations (Paren and Robin,1975), whereas at greater depths the governing causes are changes in impurity concentrations, e.g. due to acidic fallout from volcanic eruptions (Hammer, 1980; Millar, 1982). Also crystal fabric changes, as a third mechanism, might generate isochrones, as discussed in (Harrison, 1973; Fujita and Mae, 1994; Matsuoka and others, 2003). For a comprehensive description of IPR and the underlying theory the reader is referred to Bogorodsky and others (1985) and Dowdeswell and Evans (2004).

For inferring the depth values of distinct isochrones from the radar travel times information on local firn-density variations with depth should be applied for exact wave-speed calculations. Alternatively empirical relations between firn density and electromagnetic wave speed might be used as done by Richardson and others (1997). The integration of depth-density profiles then yields the distribution of cumulative mass with depth, i.e. the mass accumulated after formation of an IRH until present or during different periods between distinct time horizons. Dynamic layer thinning due to ice flow must be accounted for only for greater depths. Average annual snow-accumulation rates along the IPR profile can be derived only if the considered isochrone can be accurately dated in at least one location. Thus, for accumulation studies the radar soundings must be supported by ice core data, providing the required depth-density as well as depth-age information.

In this study, IPR data recorded in the vicinity of the EPICA deep-drilling site EDML near Kohnen station (75°S, 0°E; 2880 m a.s.l.) was used. They have been obtained as part of the Alfred-Wegener-Institute pre-site surveys in the years 1998/99 and 2000/01 using a monopulse bistatic radar system operated with antennae at 200 MHz and 250 MHz, respectively (Eisen and others, 2004; Eisen and others, 2005). Data acquisition was performed with a commercial RAMAC radar set (Mala˚ Geoscience, Sweden) between various shallow to medium depth firn-core drilling sites. Dielectric profiling (DEP measurements) of the firn cores at 5 mm intervals provided profiles of the depth-density distribution for wave-speed calculations as well as depth-age scales for isochrone dating (Wilhelms, 2000; Eisen and others, 2002). Accumulation rates were inferred from the uppermost strongly reflecting isochrone within the radar stratigraphy traced at an average depth of 20 m, corresponding to an age of about 185 years. The mapped isochrone is likely related to the Tambora (Indonesia) volcanic eruption in AD 1815.

5.3 Satellite Data

Escat C-band (5.3-GHz) data were recorded by the ERS-2 Active Microwave Instrument (AMI) in wind scatterometer mode from May 28 to June 30, 1997. Overlapping Ku-band measurements at a frequency of 14-GHz were gathered from May 20 to June 30, 1997 by the NASA scatterometer Nscat onboard the ADEOS-1 satellite. The acquisition time intervals of 35-days for Escat and 41-days for Nscat, respectively, cover full satellite repeat cycles in each case and were chosen to ensure a complete set of possible viewing angles for a particular footprint of each sensor. Both datasets are VV-polarized and cover incidence angles of 18°-59° for Escat and 17°-62° for Nscat. Scatterometer data are organized in a swath-based format, with Earth-located radar backscatter measurements collocated in 25 km x 25 km wind vector cells. Nscat data were delivered as "high resolution merged geophysical data product" (HR-MGDR) produced by NASA's Jet Propulsion Laboratory (JPL) and made available by the Physical Oceanography Distributed Active Archive Center (PO.DAAC), designed as JPL #084. Escat WNF (scatterometer WiNd Field) products were provided from the French Processing and Archiving Facility CERSAT (Centre ERS d'Archivage et de Traitement) managed by the department of Oceanography from Space at IFREMER Brest in France.

Envisat Advanced Synthetic Aperture Radar (ASAR) Wide Swath Medium-resolution C-band (5.3 GHz) images were acquired in March 2004 in VV-polarisation. Data were provided by the European Space Agency within the Cryosat Calibration/Validation Announcement of Opportunity (Cal/Val A0) They have been delivered as pre-processed Level-1 products (ASA_WSM_1P), which include slant range to ground range corrections. They cover a continuous area of 400 km x 400 km along the imaging swath at an resolution of 150 m.

5.4 Related Software and Processing Steps

Major data handling steps within this study included image reconstruction, exploratory spatial data analysis, pixel-to-pixel comparisons, raster and vector data set integration, format conversion, interpolation of point data and cartographic presentation of results. For this a number of specialized commercial software applications as well as stand-alone scripts have been used as specified in the following. The individual software modules were coupled through common data interfaces.

The selected scatterometer product types are organized in a swath based format with a number of three VV-polarized σ^0 measurements per ground resolution cell (footprint), corresponding to the fore, mid, and aft antenna beams. For image reconstruction and analysis of viewing angle effects, σ^0 measurements of multiple satellite passes had to be combined. For this, data were extracted from the storage medium (tape, CD or DVD) for the chosen acquisition times and area of interest (South of -50°S). In order to enable direct pixel-to-pixel comparisons between the different sensor measurements, the data was bound into identical SSM/I (Special Sensor Microwave Imager) south polar grids (Morris, 1992) with a pixel spacing of 25 km. To minimize distortion in our DML study are, the true scale was set at -71°S. The single beam measurements within the imaging period were allocated into grid cells using an simple "drop in the bucket" sum and average method. Multi-dimensional arrays served as a repository for the σ^0 measurements of 250 x 225 grid cells separated by their corresponding incidence angles in 1° steps and discrete azimuth-angle bins in 20° steps. From this dataset three

parameters have been calculated for each grid cell in order to characterize the backscattering: the mean backscattering coefficient σ^0_{mean} (dB) within the incidence-angle range of 30 to 40 degrees over all azimuth angles α, the factor of anisotropy *FA*, and the incidence angle gradient *IG* (dB deg^{-1}). The latter was evaluated by applying a first order least-square fit over all σ^0 measurements within the incidence angle range of $20° \leq \theta \leq 50°$, for which σ^0 (dB) was expected to decrease almost linearly. *FA* describes the azimuthal modulation of σ^0 and was calculated according to

$$FA = \frac{\sum_{j=1}^{18} \left| \sigma^0_{\Delta\alpha_j, mean} - \sigma^0_{mean} \right|}{\sigma^0_{mean}} \qquad \alpha_j = 20 \cdot \text{j}, \; \Delta\alpha_j = \alpha_{j-1} \ldots \alpha_j \tag{5.1}$$

where $\Delta\alpha_j$ stands for 18 azimuth-angle bins in 20° steps. For scatterometer data extraction, calculation of all three parameters (σ^0_{mean}, *FA* and *IG*) as well as for describing the azimuthal modulation of the backscattering by a second order polynomial function stand-alone scripts were developed using the Interactive Data analysis Language (IDL 6.x). For visualizing of the results the Environment for Visualizing Images (ENVI 4.x) was used, incorporated within the RSI (Research Systems, Inc.) IDL/ENVI software package.

For further image manipulation and spatial analysis geographical information system software ArcGIS 9.x (ESRI) and image analysis software Geomatica 9.x (PCI) were used. Correlation coefficients were calculated between C- and Ku-band σ^0_{mean}, *IG* and *FA* results as well as for all parameters to each other, separated for each sensor. To assess spatial differences between Escat and Nscat derived parameters corresponding images were subtracted or divided by each other. By applying data query functions provided within the ArcGIS Spatial Analyst extension the dry snow line could be delimited, i.e. the boundary between the dry snow zone and the narrow percolation zone at the margins of Antarctic ice sheet. For this a frequency-difference of $\sigma^0_{\text{ku}} - \sigma^0_{\text{c}} > 1.8$ dB together with Escat $FA < 0.3$ were defined as thresholds. Remaining scattered areas which have been misselected using this approach were removed manually. A Maximum Likelihood classification was applied to the scatterometer data by combining images of σ^0_{mean}, *IG* and *FA* in order to identify regions of comparable backscatter response across the Antarctic ice sheet. Signature values for 10 classes were forced by training areas with pronounced backscattering behaviour, which were delimited by first applying unsupervised K-Means and Isodata classification algorithms. Areas of agreement and disagreement between Escat and Nscat maximum-likelihood classification results were identified using the ArcGIS Raster calculator.

Envisat ASAR image processing included geocoding, viewing-angle normalizations and radiometric corrections, i.e. the speckle noise was reduced by applying a 3x3 running mean filter. The data was geocoded and gridded to a 100 m a raster using the GAMMA Differential Interferometry and Geocoding Software package. Geometrical transformation of the SAR ground range coordinates into orthonormal map coordinates was done using Polar Stereographic projection with the true scale set to –71°. Terrain correction was supported by the RAMP (Radarsat Antarctic Mapping Project) Digital Elevation Model (DEM) compiled by Liu and others (2000) at the National Snow and Ice Data Center, United States. As a by-product, the local incidence angle (θ) between surface normal and SAR look vector was computed for each image pixel. Normalization of the σ^0 measurements to an uniform incidence angle of 35° over an entire image was carried out according to

$$\sigma^0(35°)_{0°\le\phi\le360°} = \sigma^0(\theta) + IG(35° - \theta). \tag{5.2}$$

Variations of σ^0 versus azimuth angle were determined by a non-linear least square function of the form

$$\sigma^0(\alpha) = A + B\cos(2(\alpha - C)) \tag{5.3}$$

where α stands for the azimuth-look angle measured from north, and the coefficients A, B and C express the backscattering and its anisotropy. The function given in (3) was fitted to the Escat $\Delta\alpha_j$ values using IDL LMFIT sub-routine.

Figure 5.1. summarizes major processing steps, data integration and datasets generated in the course of this study.

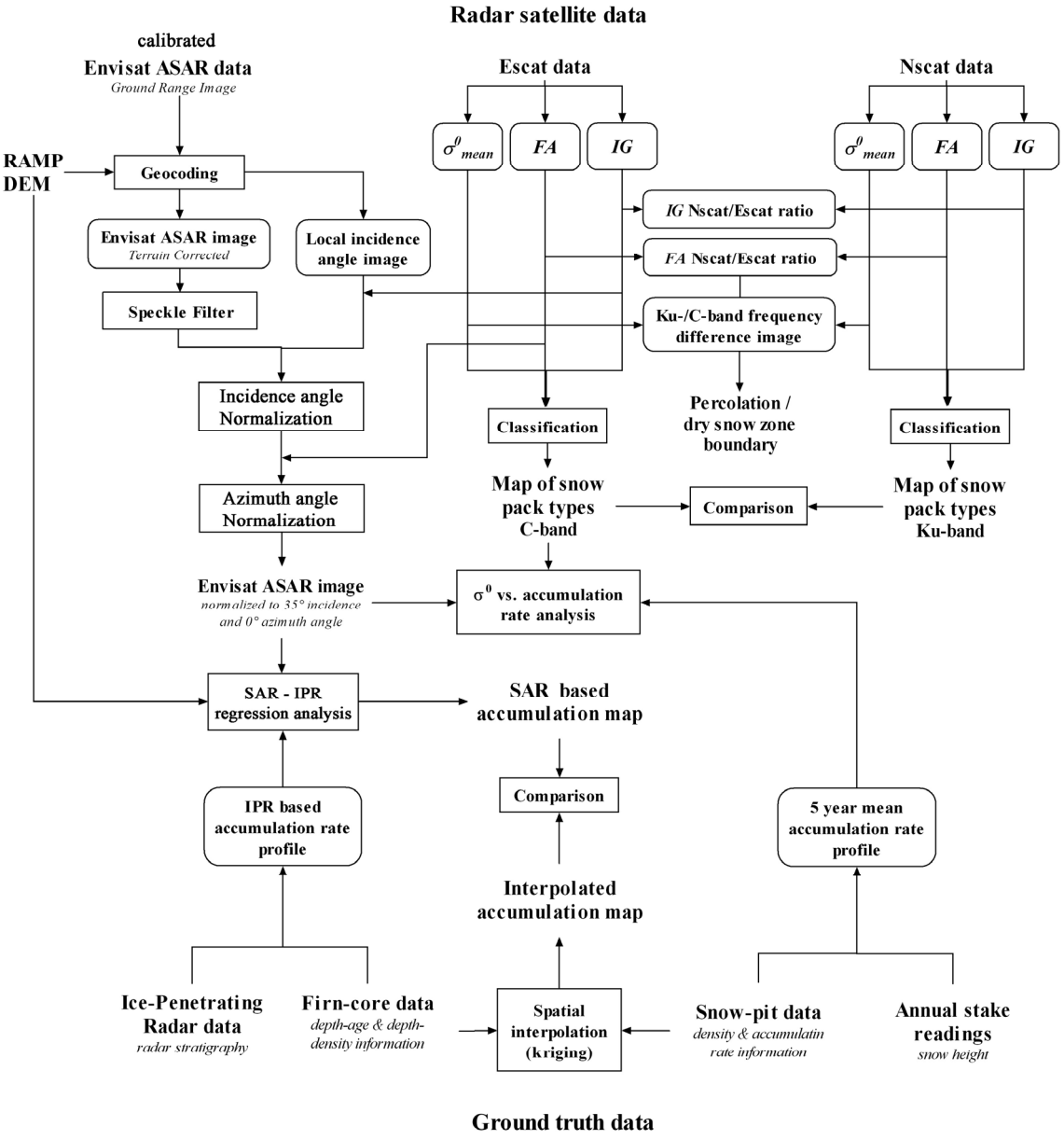

Figure 5.1. Processing steps, data integration and datasets generated in this thesis.

6 Publication Synopsis

In the following a short summary is given on the content of three papers that have been published or submitted for publication in the course of this study to present major results and achievements.

Paper I
Rotschky, G., O. Eisen, F. Wilhelms, U. Nixdorf, H. Oerter. 2004. Spatial distribution of surface mass balance on Amundsenisen plateau, Antarctica, derived from ice-penetrating radar studies. Ann. Glaciol., 39, 265-270.

In this study, the small-scale distribution of snow accumulation is investigated by means of IPR soundings in the vicinity of the EPICA deep-ice core drilling site EDML near Kohnen station (75°00', 0°00'E). The route passes a number of shallow to medium firn core sites over a distance of 320 km, what facilitates a direct comparison between the results of different approaches to assess the surface mass balance over an ice sheet. Both datasets were found to be generally in good agreement. The radar data confirm the high spatial variability of snow accumulation linked to kilometre-scale surface undulations that has been observed in earlier studies. From this it was possible to determine how representative single accumulation point measurements are at regional scale and to judge the validity of region-wide accumulation compilations based on interpolation from core data.

Paper II
Rotschky, G., W. Rack, W. Dierking, H. Oerter. 2006. Retrieving snowpack properties and accumulation estimates from a combination of SAR and scatterometer measurements. IEEE Trans. Geosci. Remote Sens., 44(4), 943-956.

Major goals of this study were (1) to identify and delimit individual Antarctic snowpack types by investigating spatial variations in radar backscattering signatures over the ice sheet as derived by scatterometers at low resolution, and (2) to empirically link the differences in SAR backscattering strength with changes in accumulation rate. The later is seen as a key factor determining snowpack morphology. For this, three parameters were extracted from C-band Escat and Ku-band Nscat scatterometer data to describe the backscattering and its dependency on viewing geometry. As a result, a first continent-wide snowpack classification was presented, which shows similar patterns for both frequencies. As a by-product the narrow percolation zone at the margins of the continent could be distinguished from the interior dry-snow zone. By taking advantage of continuous in-situ accumulation profiles mapped by IPR and stake line readings, Envisat ASAR data were calibrated to map the spatial variation of snow accumulation within the dry-snow zone, giving the first high-resolution accumulation map based on radar satellite imagery.

Paper III
Rotschky, G., P. Holmlund, E. Isaksson, R. Mulvaney, H. Oerter, M. R. Van den Broeke, J-G. Winther. A new surface accumulation map for western Dronning Maud Land, Antarctica, from interpolation of point measurements. submitted to J. Glaciol. in May 2006.

This paper presents a complete dataset of reliable accumulation point records for DML based on firn core drilling and snow pit studies, collected in the course of numerous field campaigns over a time span of about 5 decades. To obtain full spatial coverage those data were interpolated by applying geostatistical surface prediction

methods, i.e. kriging. Prior to the interpolation the data were analysed with respect to their statistical properties and spatial autocorrelation via variogram modelling. By this, two separate accumulation regimes could be distinguished as well as optimal interpolation settings defined. The result gives a picture of the broad-scale accumulation distribution over the area of investigation, reflecting overall spatial trends and topographic effects. The interpolation accuracy was assessed by producing a map of standard deviations between 10 predictions with slight variations of kriging parameters in each case. The latter can also be utilized to identify areas of insufficient sampling density and thus for locating new shallow drillings sites.

References

Adam, S. A. Pietroniro and M.M. Brugman. 1997. Glacier snow-line mapping using ERS-1 SAR imagery. *Remote Sens. Environ.*, **61**, 46-54.

Alley, R.B. 1988. Concerning the deposition and diagenesis of strata in polar firn. *J. Glaciol*., **34**(118), 283−290.

Arnold, N. and G. Rees. 2003. Self-similarity in glacier surface characteristics. *J. Glaciol.*, **49**(167), 547-554.

Arthern, R.J. and D.J. Wingham. 1998. The natural fluctuations of firn densification and their effect on the geodetic determination of ice sheet mass balance. *Climatic Change,* **40**(4), 605–624.

Attema, E.P.W. 1991. The Active Microwave Instrument on-board the ERS-1 Satellite. *Proc. IEEE*, **79**(6), 791-799.

Ballantyne, J. 2002. A multidecadal study of the number of Antarctic icebergs using scatterometer data. *In Proceedings of IGARSS'02, Toronto, Ont., Canada, June 24–28, 2002. Vol. 5*, 3029–3031.

Barrett, E.C., *ed.* 1992. *Introduction to environmental remote sensing.* Chapman & Hall, London.

Benson, C.S. 1962. Stratigraphic studies in the snow and firn of the Greenland ice sheet. U.S. Army Snow, Ice, and Permafrost Res. Establishment, Res. Rep. 70.

Bentley, C.R. and J. Wahr. 1998. Satellite gravimetry and the mass balance of the Antarctic ice sheet. *J. Glaciol.*, **44**(147), 207-213.

Bentley, C.R. 2004. Mass balance of the Antarctic ice sheet: observational aspects. In Bamber, J.L. and A.J. Payne, *eds. Mass balance of the cryosphere: Observations and modelling of contemporary and future changes.* Cambridge Univ. Press, Cambridge.

Bingham, A.W. and M. Drinkwater. 2000. Recent changes in the microwave scattering properties of the Antarctic ice sheet. *IEEE Trans. Geosci. Remote Sens.*, **38**(4), 1810–1820.

Bogorodsky, V.V., Bentely, C.R. and Gudmandsen, P.E., *eds.* 1985. Radioglaciology. Riedel Publishing Company, Dordrecht.

Bromwich, D.H. 1988. Snowfall in high southern latitudes. *Rev. Geophys.,* **26,** 149–168.

Budd, W. F. and D. B. Carter. 1971. An analysis of the relation between the surface and bedrock profiles of ice caps. *J. Glaciol.*, **10**(59). 197-209.

Comiso, J.C. 2003. Large-scale characteristics and variability of the global sea ice cover. In Thomas, D. and G. S. Dieckmann, *eds. Sea ice - An introduction to its physics, biology, chemistry and geology.* Blackwell Science, Oxford.

Davis, C.H., C.A. Kluever, B.J. Haines, C. Perez,and Y. Yoon. 2000. Improved elevation change measurement of the southern Greenland ice sheet from satellite radar altimetry. *IEEE Trans. Geosci. Remote Sensing*, **38**(3), 1367–1378.

Davis, C., Y. Li, J. McConnell, M. Frey and E. Hanna. 2005. Snowfall-driven growth in East Antarctic ice sheet mitigates recent sea-level rise. *Science*, **308** (5730), 1898 - 1901.

Demuth, M. and A. Pietroniro. 1999. Inferring glacier mass balance using Radarsat: Results from Peyto Glacier, Canada. *Geografiska Annaler*, **81A**(4), 521-540.

Dowdeswell, J.A. and S. Evans, 2004. Investigations of the form and flow of ice sheets and glaciers using radio-echo sounding. *Rep. Prog. Phys.,* **67**, 1821-1861.

Drewry D.J., S.R. Jordan and E. Jankowski. 1982. Measured properties of the Antarctic ice sheet: surface configuration, ice thickness, volume and bedrock characteristics. *Ann. Glaciol.* **3**, 83–91.

Drinkwater, M.R., R. Kwok, D.P. Winebrenner and E. Rignot. 1991. Multifrequency polarimetric synthetic aperture radar observations of sea ice. *J. Geophys. Res.*, **96(**C3), 20,679–20,298.

Drinkwater, M.R., D.G. Long and A.W. Bingham. 2001. Greenland snow accumulation estimates from satellite radar scatterometer data. *J. Geophys. Res.*, **106**(D24), 33,935–33,950.

Dunbar, R.S. 1996. NASA Scatterometer High-Resolution Merged Geophysical Data Product User's Guide, Jet Propulsion Laboratory, Pasadena, CA.

Eisen, O., U. Nixdorf, F. Wilhelms, H. Miller. 2002. Electromagnetic wave speed in polar ice: Validation of the CMP technique with high resolution dielectric-profiling and gamma-density measurements. *Ann. Glaciol.*, **34**, 150-156.

Eisen, O., U. Nixdorf, F. Wilhelms and H. Miller. 2004. Age estimates of isochronous reflection horizons by combining ice core, survey and synthetic radar data. *J. Geophys. Res.,* **109**(B4), B04106. doi:10.1029/2003JB002858.

Eisen, O., W. Rack, U. Nixdorf, F. Wilhelms. 2005. Characteristics of accumulation around the EPICA deep-drilling site in Dronning Maud Land, Antarctica. *Ann. Glaciol.*, **41**, 41-46.

Elachi, C., *ed.* 1988. *Spaceborne radar remote sensing: Applications and techniques*. IEEE Press, New York.

Ezraty, R. and A. Cavane. 1999. Intercomparison of backscatter maps over Arctic sea ice from NSCAT and the ERS scatterometer. *J. Geophys. Res.*, **104**(C5), 11,471-11,484.

Fahnestock, M., R. Bindschadler, R. Kwok and K. Jezek. 1993. Greenland ice-sheet surface properties and ice dynamics from ERS-1 SAR imagery, *Science*, **262**, 1530–1534.

Flach, J.D., K.C. Partington, C. Ruiz, E. Jeansou and M.R. Drinkwater. 2005. Inversion of the surface properties of ice sheets from satellite microwave data. *IEEE Trans. Geosci. Remote Sens.*, **43**(4), 743–752.

Floricioiu, D. and H. Rott. 2001. Seasonal and short-term variability of multifrequency, polarimetric radar backscatter of Alpine terrain from Sir- C/X-SAR and AIRSAR data," *IEEE Trans. Geosci. Remote Sens.*, **39**,(12), 2634–2648.

Forster, R., K.C. Jezek, J. Bolzan, F. Baumgartner and S. P. Gogineni. 1999. Relationships between radar backscatter and accumulation rates on the Greenland ice sheet. *Int. J. Remote Sens*., **20**, 3131–3147.

Frezzotti, M., S. Gandolfi and S. Urbini. 2002. Snow megadunes in Antarctica: sedimentary structure and genesis. *J. Geophys. Res.,* **107**(D18), 4344. doi: 10.1029/2001JD000673.

Frezzotti, M., M. Pourchet, O. Flora, S. Gandolfi, M. Gay, S. Urbini, C. Vincent, S. Becagli, R. Gragnani, M. Proposito, M. Severi, R. Traversi, R. Udisti and M. Fily. 2004. New estimations of precipitation and surface sublimation in East Antarctica from snow accumulation measurements. *Climate Dyn.*, **23**, 803–813.

Frezzotti, M., M. Pourchet, O. Flora, S. Gandolfi, M. Gay, S. Urbini, C. Vincent, S. Becagli, R. Gragnani, M. Proposito, M. Severi, R. Traversi, R. Udisti and M. Fily. 2005. Spatial and temporal variability of snow accumulation in East Antarctica from traverse data. *J. Glaciol.*, **51**(172), 113-124.

Fujita, S. and S. Mae. 1994. Causes and nature of ice-sheet radio-echo internal reflections estimated from the dielectric properties of ice. *Ann. Glaciol.*, **20**, 80-86.

Fung, A.K. and K.S. Chen. 1992. Dependence of the surface backscattering coefficients on roughness, frequency and polarization states. I*nt. J. Remote Sensing*, **13**(9), 1663-1680.

Gerland, S. H. Oerter, J. Kipfstuhl, F. Wilhelms, H. Miller and W.D. Miners. 1999. Density log of a 181 m long ice core from Berkner Island, Antarctica. *Ann. Glaciol.*, **29**, 215-219.

Giovinetto, M.B. and C.R. Bentley. 1985. Surface balance in ice drainage systems of Antarctica. *Antarct. J. U.S.*, **20**(4), 6-13.

Giovinetto, M.B., N.M. Waters, C.R. Bentley. 1990. Dependence of Antarctic surface mass balance on temperature, elevation, and distance to open ocean. *J. Geophys. Res.* **95** (D4), 3517– 3531.

Giovinetto, M.B. and H.J. Zwally. 2000. Spatial distribution of net surface accumulation on the Antarctic ice sheet, *Annals of Glaciology,* **31**, 171-178.

Goodwin, I.D. 1991. Snow-accumulation variability from seasonal surface observations and firn-core stratigraphy, eastern Wilkes Land, Antarctica. *J. Glaciol.*, **37**(127), 383-387.

Gow. A. J. 1965. On the accumulation and seasonal stratification of snow at the south pole. *J. Glaciol.,* 5(40), 467-477.

Gow, A.J. and R. Rowland. 1965. On the relationship of snow accumulation to surface topography at "Byrd Station" Antarctica. *J. Glaciol.,* **5**(42), 843-847.

Gow, A.J. 1969. On the rates of growth of grains and crystals in south polar firn. *J. Glaciol*., B(53), 241-252.

Gudmandsen, P. 1975. Layer echoes in polar ice sheets, *J. Glaciol.*, **15**(73), 95– 101.

Hall, D.K. 1998. Remote sensing of snow and ice using imaging radar. In Henderson F.M. and A.J. Lewis, *eds. Principles and applications of imaging radar. Manual of Remote Sensing.* John Wiley & Sons, New York.

Hallikainen, M. and F.T. Ulaby. 1986. Dielectric and scattering behaviour of snow and microwave frequencies, *Proceedings of the International Geoscience and Remote Sensing Symposium*, 8-11 September, Zurich, Switzerland, 87-91.

Hammer, C.U. 1980. Acidity of polar ice cores in relation to absolute dating, past volcanism, and radio-echoes. *J. Glaciol.*, **25**(93), 59-372.

Harrison, C. H. 1973. Radio echo sounding of horizontal layers in ice. *J. Glaciol.*, **12**(66), 383– 397.

Haverkamp, D., L.K. Soh and C. Tsatsoulis. 1995. A comprehensive, automated approach to determining sea ice thickness from SAR data. *IEEE Trans. Geosci. Remote Sens.*, **33**(1), 46–57.

Hempel, L., F. Thyssen, F. and M. Jonas. 1993. Accumulation during the last 2000 years along the EGIG line and to GRIP drill site derived from radio-echo soundings.

In Reeh, N. and H. Oerter, eds. *Mass balance and related topics of the Greenland ice sheet. Open File Ser. Grønlands geol. Unders.*, 93/5, 77-79.

Henderson F.M. and A.J. Lewis, *eds.* 1998. *Principles and applications of imaging radar. Manual of remote sensing. II.* John Wiley & Sons, New York

Hogan, A.W. and A.J. Gow. 1997. Occurrence frequency of thickness of annual snow accumulation layers at South Pole. *J. Geophys. Res.*, **102**(D12), 14,021-14,027.

Huybrechts, P., D. Steinhage, F. Wilhelms and J. Bamber. 2000. Balance velocities and measured properties of the Antarctic ice sheet from a new compilation of gridded data for modelling. *Ann. Glaciol.*, **30**, 52–60.

(IPCC) Intergovernmental Panel on Climate Change, IPCC Third Assessment Report, Climate Change 2001: The Scientific Basis, Cambridge Univ. Press, Cambridge.

Isaksson, E., M.R. Van den Broeke, J.-G. Winther, L. Karlöf, J.F. Pinglot and N. Gundestrup. 1999. Accumulation and proxy-temperature variability in Dronning Maud Land, Antarctica, determined from shallow firn cores. *Ann. Glaciol.*, **29**, 17-22.

Jezek, K.C., P. Gogineni and M. Shanableh. 1994. Radar measurements of melt zones on the Greenland ice sheet. *Geophys. Res. Lett.*, **21**(1), 33–36.

Joughin, I, R. Kwok and M. Fahnestock. 1996. Estimation of ice-sheet motion using satellite radar interferometry: method and error analysis with application to Humboldt Glacier, Greenland. *J. Glaciol.*, **42**(142). 564-575.

Joughin, I., L. Gray, R.A. Bindschadler, S. Price, D.L. Morse, C.L. Hulbe, K. Mattar and C. Werner, 1999. Tributaries of West Antarctic ice streams revealed by RADARSAT interferometry, *Science*, **286**, 283-286.

Jouzel, J. and 16 others. 1993. Extending the Vostok ice-core record of palaeoclimate to the penultimate glacial period. *Nature*, **364**(6436), 407-412. (doi: 10.1038/364407a0)

Karlöf, L., J.-G. Winther, E. Isaksson, J. Kohler, J.F. Pinglot, F. Wilhelms, M. Hansson, P. Holmlund, M. Nyman, R. Pettersson and M. Stenberg. 2000. A 1500 years record of accumulation at Amundsenisen western Dronning Maud Land, Antarctica, derived from electrical and radioactive measurements on a 120 m ice core. *J. Geophys. Res.*, **105**(D10), 12,471-12,483.

Karlöf, L., E. Isaksson, J-G. Winther, N. Gundestrup, H.A.J. Meijer, R. Mulvaney, M. Pourchet, C. Hofstede, G. Lappegard, R. Pettersson, R.S.W Van de Wal. 2005. Accumulation variability in a 8 by 8-km area, eastern Dronning Maud Land, Antarctica, as determined from shallow firn cores and snow pits: Some implications for ice core analysis. *J. Glaciol.*, **51**(174), 343-352.

King, J. C. and J. Turner, *eds.* 1997. *Antarctic Meteorology and Climatology.* Cambridge University Press., Cambridge.

King, J.C., P.S. Anderson, D.G. Vaughan, G.W. Mann, S.D. Mobbs and S.B. Vosper. 2004. Wind-borne redistribution of snow across an Antarctic ice rise. *J. Geophys. Res.*, **109**(D11104). doi:10.1029/2003JD004361.

König-Langlo, G., J.C. King and P. Pettre. 1998. Climatology of the three coastal Antarctic stations Dumont d'Urville, Neumayer, and Halley, *J. Geophys. Res.*, **103**(D9), 10,935-10,946.

Kramer, H.J., *ed.* 2002. *Observation of the earth and its environment: survey of missions and sensors.* Springer, Berlin.

Kwok, R., E. Rignot, B. Holt and R. Onstott. 1992. Identification of sea ice types in spaceborne synthetic aperture radar data. *J. Geophys. Res.*, **97**(C2), 2391–2402.

Lecomte, P. and E.P.W. Attema. 1993. Calibration and Validation of the ERS-1 Wind Scatterometer. Proc. First ERS-1 Symposium, *ESA-SP-359*, 19-29.

Ledroit, M, F. Rémy and J. F. Minster. 1993. Observation of the Antarctic ice sheet with the Seasat scatterometer: Relation to katabatic wind intensity and direction. *J. Glaciol.*, **39**(132), 385–396.

Legrésy, B., F. Rémy. 1998. Using the temporal variability of satellite radar altimetric observations to map surface properties of the Antarctic ice sheet, J. Glaciol, 147(44), 197-206.

Lillesand, T.M. and R.W. Kiefer, *eds.* 1994. *Remote Sensing and Image Interpretation*. John Wiley and Sons. Chichester.

Liu, H., K. Jezek, B. Li and Z. Zhao. 2001. Radarsat Antarctic Mapping Project digital elevation model version 2. Digital media, National Snow and Ice Data Center, Boulder, CO, USA.

Long, D.G., P.J. Hardin and P.T. Whiting. 1993. Resolution enhancement of spaceborne scatterometer data. *IEEE Trans. Geosci. Remote Sensing*, **31**(3), 700-715.

Long, D.G. and M. R. Drinkwater. 1994. Greenland ice-sheet surface properties observed by the Seasat-A scatterometer at enhanced resolution. *J. Glaciol*., **40**(135), 213–230.

Long, D.G. and M.R. Drinkwater. 1999. Cyrosphere Applications of NSCAT Data. *IEEE Trans. Geosci. Remote Sens.*, **37**, 1671-1684.

Long, D.G. and M.R. Drinkwater. 2000. Azimuth variation in microwave scatterometer and radiometer data over Antarctica," *IEEE Trans. Geosci. Remote Sens.*, **38**(4), 1857–1870.

Long, D.G., J. Ballantyne and C. Bertoia, 2002. Is the number of icebergs really increasing?. *EOS, Trans. American Geophysical Union*, **83**(42), 469,474-475.

Massom R. and D. Lubin, *eds.* 2006. *Polar Remote Sensing. Volume II: Ice Sheets*. Springer Verlag, Berlin.

Massonnet, D. and K.L. Feigl. 1998. Radar interferometry and its application to changes in the earth's surface. *Rev. Geophys.*, **36**(4), 441-500.

Matsuoka, K., T. Furukawa, S. Fujita, H. Maeno, S. Uratsuka, R. Naruse and O. Watanabe. 2003. Crystal orientation fabrics within the Antarctic ice sheet revealed by a multipolarization plane and dual-frequency radar survey, *J. Geophys. Res.*, **108**(B10), 2499. doi:10.1029/2003JB002425.

Mätzler, C. 1987. Applications of the interaction of microwaves with the natural snow cover. *Remote Sens. Rev*., **2**, 259–392.

Mätzler, C. 1996. Microwave permittivity of dry snow. *IEEE Trans. Geosci. Remote Sens.*, **34**(2), 573-581.

Mätzler, C. 1998. Microwave properties of snow and ice. In B. Schmitt, C. De Bergh and M. Festou, *eds. Solar System Ices.* Kluwer Adademic, Dordrecht.

Mätzler, C. and A. Wiesmann. 1999. Extension of the microwave emission model of layered snowpacks to coarse-grained snow. *Remote Sens. Environment*, **70**(3), 317-325.

Melvold, K., J.O. Hagen, J.F. Pinglot and N. Gundestrup. 1998. Large spatial variation in accumulation rate in Jutulstraumen ice stream, Dronning Maud Land, Antarctica. *Ann. Glaciol.*, **27**, 231-238.

Millar, D.H.H. 1982. Acidity levels in ice sheets from radio echo-sounding. *Ann. Glaciol.*, **3**. 199-203.

Mohr, J.J., N. Reeh and S.N. Madsen, 1998. Three dimensional glacial flow and surface elevations measured with radar interferometry. *Nature*, **391**, 273-276.

Moore, R.K., W.L. Jones. 2004. Satellite Scatterometer wind vector measurements – the legacy of the seasat satellite scatterometer. *IEEE Geosci. Remote Sens. Newslett.*, September 2004, 18-32.

Morris, C.S. 1992. "SSM/I polar grids," In: DMSP SSM/I brightness temperature grids for the Polar Regions on CD-ROM, User's Guide. National snow and ice data center, F1-F5.

Munk, J., K.C. Jezek, R.R. Forster and S.P. Gogineni. 2003. An accumulation map for the Greenland dry-snow zone facies derived from spaceborne radar. *J. Geophys. Res.*, 108(D9), ACL 8 1–12.

Naderi, F.M., M.H. Freilich and D.G. Long. 1991. Spaceborne radar measurement of wind velocity over the ocean—An overview of the NSCAT scatterometer system. *Proc. IEEE,* **79**, 850–866.

Nereson, N.A., C.F. Raymond, R.W. Jacobel and E.D. Waddington. 2000. The accumulation pattern across Siple Dome, West Antarctica, inferred from radar-detected internal layers. *J. Glaciol.,* **46**(152), 75–87.

Noone, D., J. Turner and R. Mulvaney. 1999. Atmospheric signals and characteristics of accumulation in Dronning Maud Land, Antarctica. *J. Geophys. Res.*, **104**(D16), 19,191-19,211.

Oerter, H., Graf, W., Wilhelms, F., Minikin, A. and Miller, H. 1999. Accumulation studies on Amundsenisen, Dronning Maud Land, Antarctica, by means of dielectric profiling and stable-isotope measurements: first results from the 1995– 96 and 1996–97 field seasons. *Ann. Glaciol.*, **29**, 1–9.

Oerter, H., F. Wilhelms, F. Jung-Rothenhäusler, F. Göktas, H. Miller, W. Graf and S. Sommer. 2000. Accumulation rates in Dronning Maud Land, Antartica, as revealed by dielectric-profiling measurements of shallow firn cores. *Ann. Glaciol.*, **30**, 27-34.

Oliver, C. and S. Quegan., *eds.* 1998. *Understanding Synthetic Aperture Radar images*. Artech House, Bosten.

Pälli, A., J. C. Kohler, E. Isaksson, J. C. Moore, J. F. Pinglot, V. A. Pohjola, and H. Samuelsson. 2002. Spatial and temporal variability of snow accumulation using ground-penetrating radar and ice cores on a Svalbard glacier, *J. Glaciol.*, **48**(162), 417– 424.

Paren, J.G. and G. de Q. Robin.1975. Internal reflections in polar ice sheets. *J. Glaciol.*, **14**(71), 251-259.

Partington, K.C. 1998. Discrimination of glacier facies using multi-temporal SAR data. *J. Glaciol.*, **44**(146), 42-53.

Paterson, W., *ed.* 1994. *The Physics of Glaciers*. Pergamon Press, Oxford.

Picciotto, E., G. Grozaz and W. De Breuck. 1971. Accumulation on the South Pole-Queen Maud Land Traverse, 1964-1968. Antarctic Snow and Ice Studies II, *Antarc. Res. Ser.*, **16**, 257-315.

Rack, W. and H. Rott. 2004. Pattern of retreat and disintegration of the Larsen B ice shelf, Antarctic Peninsula. Ann. Glaciol., **39**, 505-510.

Reeh, N., 1990. Past changes in precipitation rate and ice thickness as derived from age-depth profiles in ice-sheets; Applications to Greenland and Canadian Arctic ice core records. In Bleil, U. and J. Thiede, *ed. Geological History of the Polar Oceans: Arctic versus Antarctic.* Kluwer Academic Publishers. Dordrecht.

Reijmer, C.H. and M. van den Broeke. 2001. Moisture sources of precipitation in Western Dronning Maud Land, Antarctica, *Antarct. Sci.,* **13**(2), 210-220.

Reijmer, C.H. and J. Oerlemans. 2002. Temporal and spatial variability of the surface energy balance in Dronning Maud Land, East Antarctica. *J. Geophys. Res*., **107**(D24), 4759-4770 [ACL9-1 to ACL9-12]. doi: 10.1029/2000JD000110.

Reijmer, C.H., M. Van den Broeke and M.P. Scheele. 2002. Air parcel trajectories to five deep drilling locations on Antarctica, based on the ERA-15 data set, *J. Climate*, **15**, 1957-1968.

Reijmer, C. and M.R. Van den Broeke. 2003. Temporal and spatial variability of the surface mass balance in Dronning Maud Land, Antarctica, as derived from automatic weather stations. *J. Glaciol.*, **49**(167), 512-520.

Remund, Q.P. and D.G. Long. 1999. Sea-ice extent mapping using ku-band scatterometer data. *J. Geophys. Res.*, **104**(C4),11,515-11,527.

Remund, Q.P., D.G. Long and M.R. Drinkwater. 2000. An iterative approach to multisensor sea ice classification. *IEEE Trans. Geosci. Remote Sens.*, **38**(4), part 2, 1843-1856. doi: 10.1109/36.851768

Rémy F. and J. F. Minster. 1991. A comparison between active and passive microwave measurements of the Antarctic ice sheet and their association with the surface katabatic winds. *J. Glaciol.*, **37**(125), 3–10.

Rémy, F., M. Ledroit and J. F. Minster. 1992. Katabatic wind intensity and direction over Antarctica derived from scatterometer data. *Geophys.Res. Lett.*, **19**, 1021–1024.

Repp, K. 1978. Snow accumulation and snow stratigraphy on Riiser-Larsenisen, Dronning Maud Land, Antarctica. In *Results from Norwegian Antarctic Research 1974-1977*. Norsk Polarinstitutt, Skrifter Nr. 169, 81-92.

Richardson, C., E. Aarholt, S.E. Hamran, P. Holmlund and E. Isaksson. 1997. Spatial distribution of snow in western Dronning Maud Land, East Antarctica, mapped by a ground-based snow radar. *J. Geophys. Res.,* **102**(B9), 20,343–20,353.

Richardson-Näslund, C. 2004. Spatial characteristics of snow accumulation in Dronning Maud Land, Antarctica. *Global and Planetary Change*, **42**, 31-43.

Rignot E. and M.R. Drinkwater. 1994. Winter sea ice mapping from multiparameter synthetic aperture radar data. *J. Glaciol.*, **40**(134), 31–45.

Rignot, E. 1998. Fast recession of a West Antarctic glacier. *Science*, **281**, 549-551.

Rignot. E. 2001. Evidence for rapit retreat and mass loss of Thwaites Glacier, West Antarctica. *J. Glaciol.*, **47**(157), 213-222.

Rignot, E. and R.H. Thomas. 2002. Mass balance of polar ice sheets. *Science,* **297**(5586), 1502–1506.

Rignot, E., D. Vaughan, M. Schmeltz, T. Dupont and D. MacAyeal. 2002. Acceleration of Pine Island and Thwaites Glaciers, West Antarctica. *Ann. Glaciol.*, **34**, 189-1994.

Rott H. and K. Sturm. 1991. Microwave signature measurement of Antarctic and Alpine snow. In *11th EARSeL Symposium*, Graz, Austria, 1991, 140–151.

Rott, H. and R.E. Davis. 1993. Multifrequency and polarimetric SAR observations on alpine glaciers. *Ann. Glaicol.*, **17**, 98-104.

Rott, H., K. Sturm and H. Miller. 1993. Active and passive microwave signatures of Antarctic firn by means of field measurements and satellite data, *Ann. Glaciol.,* **17**, 337–343.

Rott, H., K. Sturm and H. Miller. 1993. Active and passive microwave signatures of Antarctic firn by means of field measurements and satellite data. *Ann. Glaciol.*, **17**, 337–343.

Rott, H., W. Rack, P. Skvarca and H. De Angelis. 2002. Northern Larsen Ice Shelf, Antarctica: further retreat after collapse. *Ann. Glaciol.,* **34**, 277–282.

Sabins, F.F., *ed.* 1997. *Remote Sensing Principles and Interpretation.* W. H. Freeman & Company, New York.

Scambos, T., C. Hulbe and M. Fahnestock. 2003. Climate-induced ice shelf disintegration in the Antarctic Peninsula, *Antarct. Res. Ser.*, **79**, 79– 92.

Schwerdtfeger, W, *ed.* 1984. Weather and Climate of the Antarctic. Developments in Atmospheric Sience, 15, Elsevier Science Publishers B. V., Amsterdam.

Shepherd, A. , D. Wingham and J. Mansley. 2002. Inland thinning of the Amundsen Sea sector, West Antarctica. *Geophys. Res. Lett.,* **29**(10), 1364-1367. doi: 10.1029/2001GL014183

Sommer, S., C. Appenzeller, C., R. Röthlisberger, M.A. Hutterli, B. Stauffer, D. Wagenbach, H. Oerter, F. Wilhelms, H. Miller and R. Mulvaney. 2000. Glacio-chemical study spanning the past 2 kyr on three ice cores from Dronning Maud Land, Antarctica. 1. Annually resolved accumulation rates. *J. Geophys. Res.*, **105**(D24), 29,411-29,421.

Spikes, V.B., G.S. Hamilton, S.A. Arcone, S. Kaspari and P. Mayewski. 2004. Variability in accumulation rates from GPR profiling on the West Antarctic plateau. *Ann. Glaciol.*, **39**, 238-244.

Steinhage, D., U. Nixdorf, U. Meyer and H. Miller. 1999. New maps of the ice thickness and subglacial topography in Dronning Maud Land, Antarctica, determined by means of airborne radio-echo sounding. *Ann. Glaciol.,* **29**, 267–272.

Stenberg, M., E. Isaksson, M. Hansson, W. Karlén, P.A. Mayewski, M.S. Twickler, S.I. Whitlow and N. Gundestrup. 1998. Spatial variability of snow chemistry in western Dronning Maud Land, Antartica. *Ann. Glaciol.*, **27**, 378-384.

Stephen, H. and D.G. Long. 2000. Study of iceberg b10a using scatterometer data. Geoscience and Remote Sensing Symposium, 2000. Proceedings. IGARSS 2000. *IEEE 2000 International Volume 3*, vol. 3, 1340-1342. doi: 10.1109/IGARSS.2000.858112

Stiles, W.H. and F.T. 1982. Ulaby, Dielectric properties of snow, In Proc. Workshop of the Properties of Snow, Snowbird, Utah, 8-10 April 1981, CRREL Special Report 82/18, 91-103.

Stocker, T.F. 2003. South dials north. *Nature*, **424**, 496-499.

Surdyk S. and M. Fily. 1993. Comparison of the passive microwave spectral signature of the Antarctic ice sheet with ground traverse data. *Ann. Glaciol.*, **17**, 161-166.

Thomas, R., C. Davis, W. Krabill, and J. McConnell. 1999. Greenland Ice Sheet Elevation Change Since 1978 from Radar and Laser Altimetry, *Polar Geography,* **23**(3), 169-184.

Thomas, R., E. Rignot, G. Casassa, P. Kanagaratnam, C. Acuña, T. Akins, H. Brecher, E. Frederick, P. Gogineni, W. Krabill, S. Manizade, H. Ramamoorthy, A. Rivera, R. Russell, J. Sonntag, R. Swift, J. Yungel and J. Zwally. 2004. Accelerated Sea-Level Rise from West Antarctica. *Science,* **306**, 255-258.

Tsatsoulis C. and R. Kwok. 1998. *Analysis of SAR Data of the Polar Oceans*. Springer-Verlag, Berlin 1998.

Tuiri, R., A. Sihvola, E.G. Nyfors and M. Hallikainen. 1984. The complex dielectric constant of snow at microwave frequencies. *IEEE J. Oceanic Engin.*, **9**(5), 377-382.

Ulaby, F.T., R.K. Moore and A.K. Fung, *eds.* 1982. *Microwave remote sensing active and passive, vol. II, Radar remote sensing and surface scattering and emission theory.* Addison-Wesley Publishing Co., Reading.

Van den Broeke, M.R., J.-G. Winther, E. Isaksson, J.F. Pinglot, L. Karlöf, T. Eiken and L. Conrads. 1999. Climate variables along a traverse line in Dronning Maud Land, East Antarctica. *J. Glaciol.*, **45**(150), 295-302.

Van den Broeke, M.R., N. P.M. van Lipzig and E. van Meijgaard. 2002. Momentum budget of the East-Antarctic atmospheric boundary layer: results of a regional climate model. *J. Atmos. Sci.*, **59**(21), 3117-3129.

Van den Broeke, M. R., W. J. van de Berg and E. van Meijgaard. 2006. Snowfall in coastal West Antarctica much greater than previously assumed, *Geophys. Res. Lett.,* **33**, L02505. doi:10.1029/2005GL025239.

Van der Veen, C.J., 1993. Interpretation of short-term ice-sheet elevation changes inferred from satellite altimetry. *Climate Change*, **23**. 383-405.

Van Lipzig, N.P.M., E. van Meijgaard and J. Oerlemans. 2002a.The effect of temporal variations in the surface mass balance and temperature-inversion strength on the interpretation of ice-core signals. *J. Glaciol.*., **48**(163), 611-621.

Van Lipzig, N.P.M., E. van Meijgaard and J. Oerlemans. 2002b.The spatial and temporal variability of the surface mass balance in Antarctica: results from a regional climate model. *Int. J. Climatol.*, **22**,1197-1217.

Vaughan, D.G. and C.S.M. Doake. 1996. Recent atmospheric warming and retreat of ice shelves on the Antarctic Peninsula. *Nature,* **379**(6563), 328–331.

Vaughan, D.G., J.J. Bamber, M.B. Giovinetto, J. Russell and A.P.R. Cooper. 1999a. Reassessment of net surface mass balance in Antarctica. *J. Clim.*, **12**, 933–946.

Vaughan, D.G., H. F.J. Corr, C.S.M. Doake and E.D. Waddington. 1999b. Distortion of isochronous layers in ice revealed by ground-penetrating radar. *Nature*, **398**(6725), 323-326.

Vaughan, D.G., P.S. Anderson, J.C. King, G.W. Mann, S.D. Mobbs and R.S. Ladkin. 2004. Imaging of firn isochrones across an Antarctic ice rise and implications for patterns of snow accumulation rate. *J. Glaciol.*, **50**(170), 413-418.

Velicogna I. and J. Wahr. 2006. Measurements of time-variable gravity show mass loss in Antarctica, *Science*, **311**, 1754-1756.

Wen, B., L. Tsang, D.P. Winebrenner and A. Ishimaru. 1990. Dense Medium Radiative Transfer Theory: Comparison with experiment and application to microwave remote sensing and polarimetry. *IEEE Trans. Remote Sens.,* 28(1), 46-59.

Wentz, F. J., S. Peteherych and L. A. Thomas. 1984. A model function for ocean radar cross-sections at 14.6 GHz. *J. Geophys. Res.*, 86(C7), 3689-3704.

West, R.D., D.P. Winebrenner and H. Rott. 1996. Microwave emission from density-stratified Antarctic firn at 6 cm wavelength, *J. Glaciol.*, **42**(140), 63-76.

Wilhelms, F. 2000. Messung dielektrischer Eigenschaften polarer Eiskerne *Ber. Polarforsch./Rep. Pol. Res.* 367, 1–171.

Wingham, D.J., A.L. Ridout, R. Scharroo, R.J. Arthern and C.K. Shum. 1998. Antarctic elevation change 1992 to 1996. *Science,* **282**(5388), 456–458.

Wismann, V. R. and K. Boehnke. 1997. Monitoring snow properties on Greenland with ERS scatterometer and SAR, *Eur. Space Agency Spec. Publ*., *ESA SP-414*, 857–862.

Zhao, Y., A.K. Liu and D.G. Long. 2002. Validation of Sea Ice Motion from QuikSCAT with those from SSM/I and Buoy. *IEEE Trans. Geosci. Remote Sens.*, **40**, 1241-1246.

Zwally, H. J. and S. Fiegles. 1994. Extent and duration of Antarctic surface melt. *J. Glaciol.*, **40**, 463–476.

Zwally H.J. and M.B. Giovinetto. 1995. Accumulation in Antarctica and Greenland derived from passive-microwave data: a comparison with contoured compilations. *Ann. Glaciol.*, **21**, 123-130.

Zwally, H.J. and J. Li. 2002. Seasonal and interannual variations of firn densification and ice-sheet surface elevation at Greenland summit. *J. Glaciol.,* **48**(161), 199–207.

Zwally, H.J., M.B. Giovinetto, J. Li, H.G. Cornejo, M.A. Beckley, A.C. Brenner, J.L. Saba, D. Yi. 2005. Mass changes of the Greenland and Antarctic ice sheets and shelves and contributions to sea-level rise: 1992–2002. *J. Glaciol.,* **51**(175), 509-527.

Acknowledgements

I see this thesis as a milestone in my life. The years here at AWI gave me a lot and will leave a permanent impression. I gained not only theoretical knowledge and skills, but even more I learned the people, especially myself. I feel changed in many ways. Therefore, first of all I thank Enrico, my partner in life, for sticking by me in spite of all difficulties and a constant lack of time during four years of being away from home. Furthermore, I am grateful to my family and all the many good souls that have crossed my way and encouraged me to go on.

I thank Prof. Dr. Heinrich Miller, deputy director of AWI, for giving me the chance to start with a thesis in the field of glaciology and for becoming my doctoral advisor. Special thanks to Dr. Wolfgang Rack (AWI), Dr. Olaf Eisen (AWI) and Dr. Hans Oerter (AWI) for their very supportive, friendly and patient supervision of my studies. Their advice introduced me to science and first enabled this thesis. In addition, I appreciate the valuable comments on the manuscripts of my papers made by co-authors and anonymous reviewers. Last but not least, I thank the colleagues at AWI for being very cooperative and a good substitute for family and friends at home.

I am glad to be finished, but at the same time sad having to leave this place, polar sciences and close friends. I will keep it all in good memory, especially Novolazarevskaya.

PAPER I

Annals of Glaciology 39, 265-270, 2004. © 2004 IGS

Spatial distribution of surface mass balance on Amundsenisen plateau, Antarctica, derived from ice-penetrating radar studies

Gerit ROTSCHKY, Olaf EISEN, Frank WILHELMS, Uwe NIXDORF, Hans OERTER

Alfred Wegener Institute for Polar and Marine Research. P.O. Box: 120161, 27515 Bremerhaven, Germany

ABSTRACT. The distribution of surface mass balance on Amundsenisen, Dronning Maud Land, Antarctica, is investigated along a continous profile line. Ice-penetrating radar is used to map variations in ice-layer thickness within the upper 100 m of the ice sheet. The route passes several firn- and ice- core drilling sites over a distance of 320 km. Dielectric-profiling data of ice cores are used to calculate the depths of selected reflection horizons and the cumulative mass of the ice column. The local surface mass balance is determined as a temporal average, covering a time span of almost two centuries. The findings indicate a complex accumulation pattern superimposed on a general low surface mass balance, which is related to small-scale surface undulations. The results of the radar soundings are in general in good agreement with surface mass-balance data derived from firn-core studies. Discrepancies between these two datasets can be explained by spatial mismatch or by minor quality of either ice-core profiles or radar data. For regional comparison ofradar-based accumulation data we use an accumulation distribution interpolated from point measurements. The surface mass balance varies up to 50% over short distances, with correlation lengths of <10 km. We conclude that the current utilization schemes of point sampling are only capable of reproducing local values and regional trends, but provide no information on the small-scale variability of surface mass balance.

1. INTRODUCTION

The accumulation rate and its spatial pattern across Antarctica are the main influences determining the growth and movement of the ice sheet. The accumulation distribution is needed as a fundamental input factor in glacier mass balance studies, necessary to, for instance, estimate current sea level changes. The interpretation of physical and chemical properties measured along ice cores, used for paleo-climatic reconstruction, also relies on an exact knowledge about present and past surface mass balance distribution across the Antarctic continent.

Surface mass balance calculations are usually based on stake readings, snow-pit samples, and shallow firn cores. These measurements yield parameters to estimate the spatial variability of the Antarctic surface mass balance, as well as its variation over the last few decades. Use of this information has the disadvantage that it is uncertain how these irregularly and sparsely collected data sets are able to represent general climatic trends of precipitation and wind drift patterns for larger areas.

Over recent years, the traditional methods have been supplemented by methodological ice-penetrating radar (IPR) studies to improve the understanding of spatial accumulation patterns (e.g. Richardson and others, 1997; Nereson and others, 2000; Richardson-Näslund, 2001; Frezzotti and Flora, 200; Pälli and others, 2002). High-frequency IPR is capable of imaging the physical structure of the upper hundreds of metres of the ice column. On the Antarctic inland plateau, this provides a means to derive information about the local surface mass balance over the last 100-1000 years. It has thus become possible to map accumulation rates and their spatial variations along continuous profiles within the upper parts of the snow pack.

The studies underlying this paper were carried out within the European Project for Ice Coring in Antarctica (EPICA), but are likewise a contribution to the International Trans-Antarctic Scientific Expedition programme (ITASE). The latter was

established in order to improve the collection and understanding of environmental parameters, representing the spatial variability of the Antarctic climate within the last 200 years. IPR data collected on Amundsenisen, Dronning Maud Land (DML), the Atlantic sector of Antarctica, allow us to derive spatial characteristics of the distribution of accumulation. Moreover, we estimate the spatial representativity of accumulation rates derived from point measurements, like firn and ice-core studies located on or near the profile line, by comparison with the IPR-based results. This enables us to judge the suitability of regional surface mass balance estimation for Amundsenisen.

2. ORIGIN OF DATA

2.1. Deriving accumulation rates from IPR surveys

Coherent internal radar reflection horizons (IRHs) detected with IPR systems are generally considered to be features of equal age, often referred to as isochrones. The processes forming electromagnetic reflectors take place at or near the glacier surface at approximately the same time, with the submergence rate of the isochronic surface being determined by interaction of the flow field and surface accumulation rate (Robin and others, 1969; Gudmandsen, 1975; Millar, 1981). Knowledge of the depth of an IRH in respect to the surface, its age, and the density-depth profile of the firn enables us to calculate the mass accumulated after formation of the IRH, and thus the average surface mass balance.

IPR data analyzed here result from common-offset measurements between various borehole locations and were performed with a commercial RAMAC radar set (Malå Geoscience, Sweden). The monopulse bistatic radar system was operated with antennae at 200 and 250 MHz: unshielded dipoles in a fixed distance of 60 cm in the former, and shielded antennae at a distance of 36 cm in the latter case. Both set-ups are permanently mounted in skid-boxes and connected with the central processing unit via light-conducting cables, thus avoiding noise from ohmic conductors. The processing unit was operated by a Husky FC PX5 personal computer, using the radar

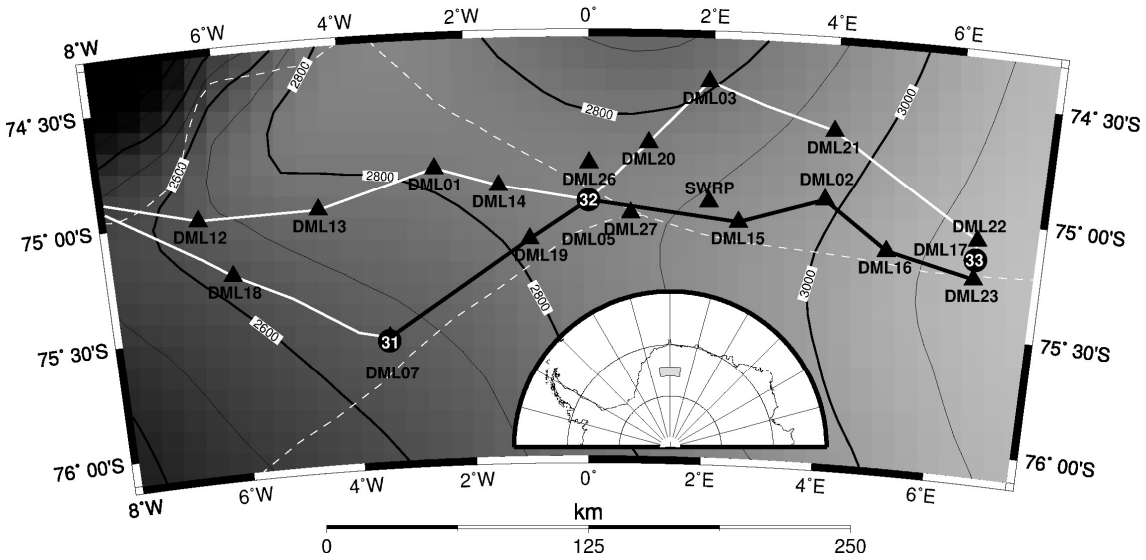

Fig. 1. Radar profiles and surface topography (Liu and others, 2001) in the region of interest on Amundsenisen plateau. Elevation contours (100m interval and grey code) are given as thin solid black lines; the position of ice divides is indicated by the dashed white lines. The route of the radar survey (1999 and 2001) is shown as solid straight lines. The section of the radar profile analyzed here is shown as thick solid black line, extending from the ice-core drilling sites (circles) DML07 (B31) to DML17 (B33), passing DML05 (B32), near the EPICA deep-drilling camp Kohnen. Other firn-core sites in the vicinity of radar profiles within the study area are shown as triangles including site labels: DML: Alfred-Wegener-Institut pre-site surveys (Oerter and others, 2000); SWRP: Swedish Antarctic Research Programme (Isaksson and others, 1996). The location of the study area on the Antarctic continent is indicated as the shaded region in the inset.

system software. The 200 MHz survey was carried out in 1999 between the ice cores B32 and B33, using a snow tractor for pulling at an average speed of 8 km h^{-1} (Fig. 1). Traces were recorded every 1.5 m, triggered by a distance wheel, in a 1500 ns time window consisting of 2400 samples. The 250 MHz data were recorded in 2001 between B32 and B31, pulling the device by a snowmachine at 12 km h^{-1} with traces recorded every meter in a 1570 ns time window with 2048 samples. For either measurement set-up the stored traces consist of eight vertically stacked pulse recordings. Continuous geographical positioning of the IPR profiles was obtained from kinematic global positioning system (GPS) measurements.

Post-recording processing was performed using Paradigm Geophysical FOCUS version 4.2 software and includes five-fold horizontal stacking, bandpass filtering and automatic gain control. IRHs were semi-automatically tracked in the processed data with the Landmark OpenWorks release 2003.0 software, exploiting the coherency of signal features. IRHs were observed at numerous travel times and tracked continuously between the boreholes.

Dielectric profiling of the firn and ice cores in 5 mm intervals provides profiles of the wave speed-depth and the density-depth distribution (Wilhelms, 2000; Eisen and others, 2002). Wave speeds are used to convert radar data from travel time to depth, integration of density profiles yield the distribution of cumulative mass with depth. The travel-time and cumulative mass profiles of all three ice cores are quasi-identical (Fig. 2) and show differences only on a high-resolution depth scale. It is therefore justified to assume a homogeneous density-depth distribution within the area of interest and thus using the data from B32, located between B31 and B33, for the whole radar profile.

Datings of IRHs are obtained by transferring the ice core ages to the respective depth of the IRH at each drilling location. The ice cores are dated by annual-layer counting of multi-parameter chemical records combined with identification of volcanic horizons (Sommer and others, 2000). For further analysis in this study, we use the uppermost strong IRH that is continuously trackable along the whole profile. Near B32 it is located at around 25 m depth. Dating estimates of this IRH are AD 1815 at B31, AD 1822 at B32, and AD 1813 at B33, indicating that the IRH is likely related to the Tambora volcanic eruption in AD 1815. The mean of all three datings, AD 1817, is used as the time of origin of this IRH, with an uncertainty of ± 5 years. This error accounts for uncertainties in the travel-time depth conversion, ice-core dating, and age transfer from ice-core depth to IRH depth (Eisen and others, 2004), as well as the 1-2 year delay of aerosol deposition related to the volcanic eruption (Traufetter and others, 2004). The total error of the IRH age and depth is thus a combination of different uncertainties, resulting from the resolution of the radar system (0.8 m), the error related to tracking of IRH (about 1 m), and dating accuracy, as described above.

Finally, we transfer the cumulative mass corresponding to the depth of the IRH at each

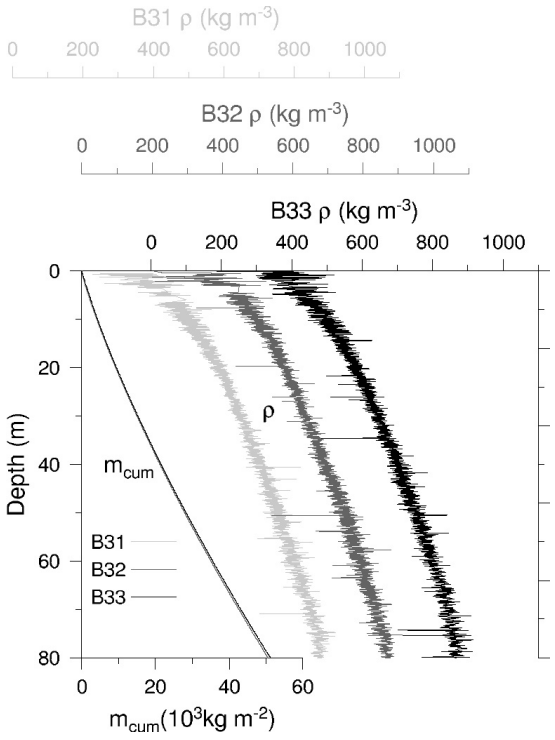

Fig. 2. Depth profiles of density ρ derived from dielectric profiling (x axes at top of graph) of ice cores B31 (light grey), B32 (dark grey) and B33 (black). Note the different x-axis offset for each density profile. The cumulative mass profiles (m_{cum}, bottom axis) result from integration of the density profiles. They are virtually indistiguishable, as small differences in density are smoothed out by integration. As the cumulative mass profiles are plotted without offset, only the black profile on top of the other two is visible.

point along the profile. The average surface mass balance then results from dividing the cumulative mass by the respective age of the reflector, i.e. 184 years for section B31-B32 (survey 2001) and 182 years for section B32-B33 (survey 1999).

2.2. Accumulation data based on point sampling

A compilation of accumulation data, consisting of 121 data points, is available for the DML region (Ühlein, 1999) and roughly comprises 10^6 km². It is based on snow-pit studies and firn-core data taken from the literature. The distribution of accumulation in our region of interest has been presented and discussed by Oerter and others (2000). The averaging period of the different data points varies between 5 years for snow pits and up to 200 years for ice cores.

3. RESULTS

For comparison purposes we focus on the accumulation measurements adjacent to our IPR route near the ice divide (Fig. 1). Profiles of surface topography, accumulation, internal structure, and bedrock topography along the route are shown in Fig. 3a-d. Before comparing and discussing the results of the two different methods in respect to accumulation rates, we briefly describe typical characteristics of each data set separately.

3.1. IPR-based surface mass-balance profiles

In total, five strong IRHs are continuously tracked from B31 to B33. The variation of travel times around the mean increases from ~100 ns for the uppermost reflector to ~500 ns for the deepest (Fig. 3c). This amounts to changes in the horizons' depths between about 10 and 50 m, respectively, over short distances along the surveyed profiles. The annual surface mass-balance rate calculated from the AD 1817 horizon at around 20 m depth is shown in Figure 3b, together with accumulation rate estimates of firn and ice cores along the same profile line. The accumulation derived from the radar data varies between 32.6 and 74.3 kg m^{-2} a^{-1}. The resulting mean accumulation is 53.8 kg m^{-2} a^{-1}, with a standard deviation of 7.7 kg m^{-2} a^{-1} for an average sampling rate of 1.3 m. The autocorrelation function calculated from the IPR-based accumulation rate along the whole profile shows a strong decrease to 0.65 over the first 3 km separation (Fig. 4). The decrease continues less steep to around 10 km, to level out at a value of about 0.4.

The mass-balance information is complemented by surface and bedrock topography given along the IPR route (Fig. 3a and d). Bedrock heights are taken from Steinhage and others (1999), and surface altitude data were taken from RADARSAT Antarctic Mapping Project (RAMP) digital elevation model version 2.0 (Liu and others, 2001). The elevation along our route gently rises from about 2650 to 3150 m a.s.l. over a distance of 320 km from DML07 to DML17. To emphasize small-scale surface variations of just a few metres over 10 km within the smooth surface topography, the difference of local surface elevation from a 50 km running mean is also calculated. They can be linked to undulations in the bedrock relief, a well-known phenomenon (Robinson, 1966; Budd and Carter, 1971; Robin and Millar, 1982), being on the order of hundreds of metres over the same distance. As most sections of our survey profiles are not parallel to the mean flow directions, the bedrock and surface undulations are slightly shifted.

3.2. Regional distribution of accumulation rates from point sampling

The accumulation distribution for the Amundsenisen plateau as derived from point measurements covers a 150 km wide stripe along both sides of latitude 75°S, between 5° W and 5° E. As described by Oerter and others (2000), the distribution shows a continuing general trend of decreasing accumulation rates from the coastal area towards the interior of the ice sheet. Along the whole profile, the mean surface balance between B31 and B33 is 56 kg m^{-2} a^{-1}, with a standard deviation of 9 kg m^{-2} a^{-1}. In the east as well as in the west of the studied area, spots with accumulation rates <45 kg m^{-2} a^{-1} are found. In the centre, mainly eastwards of point DML05 along the ice divide, the accumulation rates vary between 45 and 65 kg m^{-2} a^{-1}. Towards the north, the accumulation rates increase to values around 90 kg m^{-2} a^{-1}, as determined at point DML03. The value of 77 kg m^{-2} a^{-1} reported by Isaksson and others

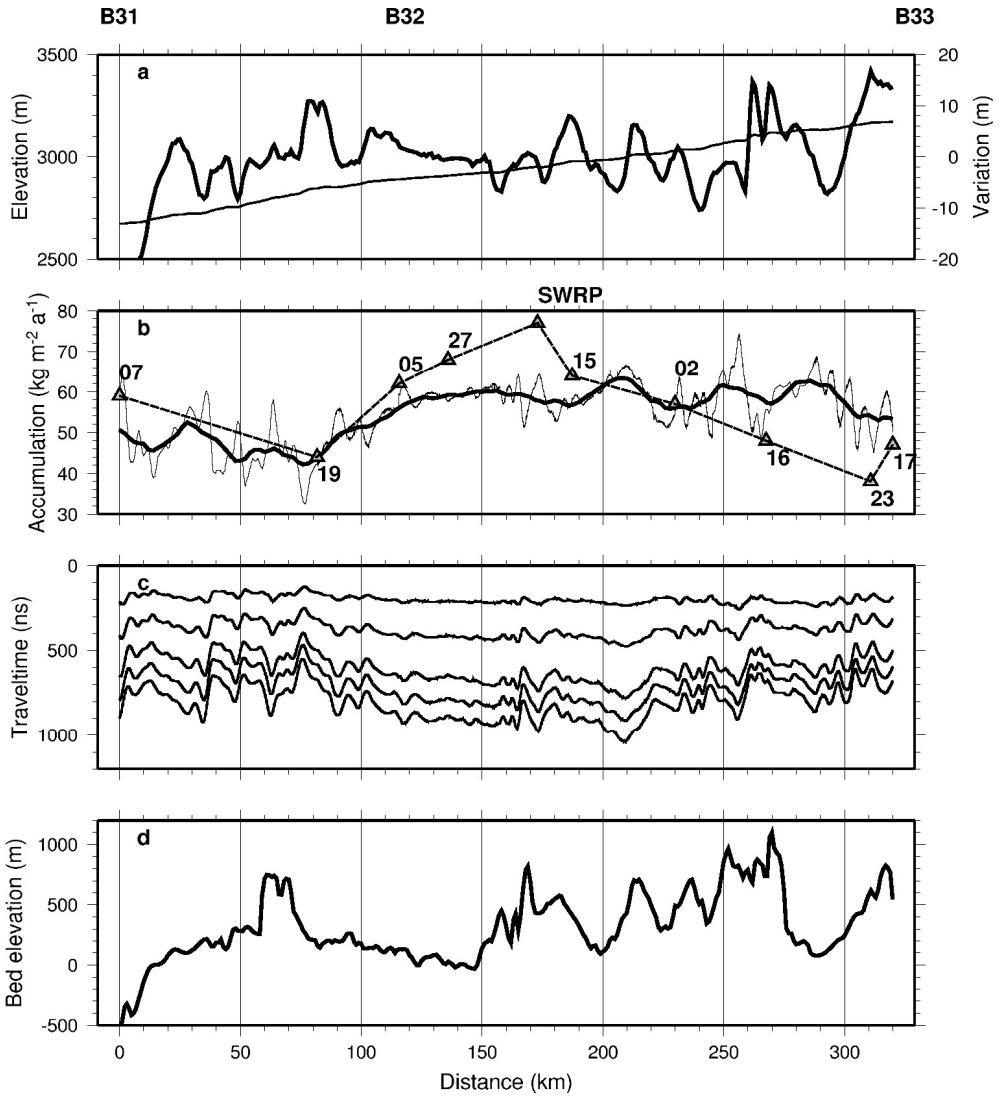

Fig. 3. (a) Surface topography (Liu and others, 2001) given as World Geodetic System 1984 ellipsoid (WGS84) elevation (thin line, left axis), and its variation as difference of local height from the 50 km running mean of the surface elevation (thick line, right axis). (b) Surface mass-balance profiles based on radar (thin line), its 50km running mean (thick line) and linearly interpolated point samples (dashed line). Location and values of firn and ice cores are shown as triangles, with their site labels next to them (numbers: DML sites; see Fig. 1). (c) Depth distribution of selected internal horizons as a function of two-way travel time. The uppermost horizon, dated to AD 1817, is used to derive the surface mass balance shown in (b). (d) Bedrock topography (Steinhage and others, 1999). The location of the three ice cores B31–33 is shown on top of the graph.

(1996) at the site SWRP in Figure 1 is exceptional compared to surrounding values of 65 kg m^{-2} a^{-1}.

3. DISCUSSION

The mass balances obtained from IPR data agree well with values gathered from several firn and three shallow ice cores which are located along the IPR travel route (Fig. 3). The values are nearly identical to most of the point samples. Exceptions are the locations DML15, DML23, DML27, and SWRP, where larger discrepancies of up to 13 kg m^{-2} a^{-1} are observed. The reasons for this will be discussed later.

Between the single core locations, the IPR results show large variations in layer thickness and thus local surface mass-balance rates, revealing a rather complex accumulation pattern for our study area. The standard deviation of 14% compares well with observations of Richardson and Näslund

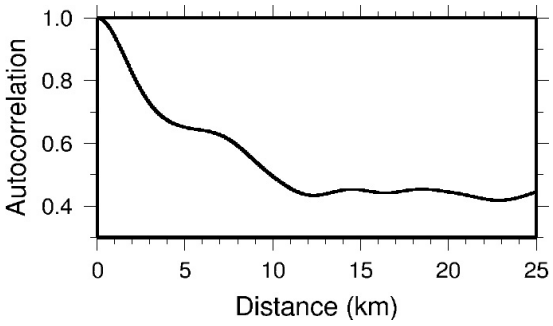

Fig. 4. Autocorrelation function of the unfiltered accumulation rates derived from tracking of the AD 1817 IRH.

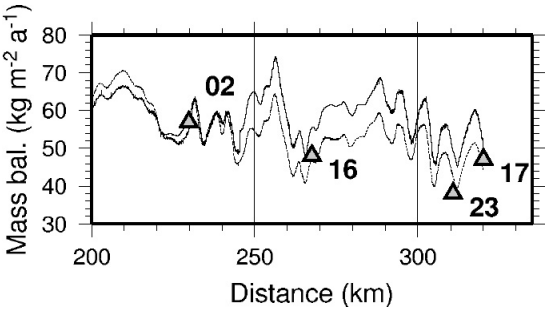

Fig. 5. Surface mass-balance profiles obtained from two IRHs of different age, dated to AD 1817 (upper solid line) and AD 1619 (lower dashed line). The deeper buried reflection horizon (dashed line) better reproduces mass-balance values obtained from core analysis (triangles) at locations DML16, DML23 and DML17 (indicated next to the symbols).

(2001), who quantified the spatial variability of the net snow accumulation to around 10% for undisturbed plateau areas of DML.

As the observed changes in accumulation are irregular in character beyond a separation of 10 km (Fig. 4), they cannot be systemized in terms of wavelength, unlike other features, e.g. snow megadunes: Frezzotti and others, 2002). Nevertheless, it seems likely that the surface mass-balance variations are related to small-scale undulations of the surface topography. In some parts of the survey profile (e.g. between DML07 and DML19), an increase in mass balance occurs at apparent surface depressions, while a lower accumulation rate can be observed where the elevation is higher then the average. In other parts, accumulation maxima occur rather in phase with surface heights. Care needs to be taken with these observations, however. An accurate relation between surface topography and accumulation rates requires a two-dimensional map of elevations in high resolution, as the topography along track is not necessarily the same in other directions.

Linear interpolation of the point data along the IPR profile line shows an alternating over- and underestimation of accumulation rates in comparison to the IPR-derived mass balance data. Applying a 50 km running mean to the IPR surface mass balance results in a distribution that is approximately in phase with the interpolated point samples (Fig. 3b). Starting in the west, a gradual decrease in accumulation is followed after a minimum near km 80 (DML19) by a strong increase up to km170 in both profiles. However, whereas the smoothed IPR-based accumulation remains level with slight variations, the interpolated point samples continually decrease from km 175 (SWRP) to km310 (DML23). One reason for the differences in the eastern half of the profiles is the strong influence of individual sample points representing local extremes. For example, the interpolated maximum at km 170 is a consequence of the relatively high accumulation rate of 77 kg m^{-2} a^{-1} mentioned above, and the strong minimum at km 310 results from the low value of 38 kg m^{-2} a^{-1}. Near these sites, the IPR-based accumulation rate shows strong variations, but still very different values than the interpolated ones.

In two cases, the point samples are not directly located on the radar route. DML27 is about 5 km to the south, and on the other side of the ice divide the SWRP site is about 8 km north of the IPR route. Given the strong decorrelation of the surface mass balance over the first 3 km (Fig. 4), the differences to the radar-based mass balance are not surprising.

The disagreement between radar- and core-based mass-balance values at DML15 and DML23 originates from two different kinds of miscalculation. Examination of the firn-core profile retrieved at DML15 reveals that bad core quality lead to gaps within the upper part of the density-depth profile, which were closed by linear interpolation. Thus, the increase of density with depth is too strong, which in turn leads to an overestimation of the cumulative mass.

In contrast, at DML23, increased antenna ringing causes a noisy radargram in the upper 20 m (~200 ns) of the ice column. Hence, our reference IRH has likely been incorrectly

tracked, leading to an underestimation of the calculated accumulation rate. Noise caused by antenna ringing decreases with increasing travel time. Repeating the whole calculation process for a deeper reflection horizon, linked to the year AD 1619, produces an accumulation rate that again matches with the core data (Fig. 5), confirming that the AD 1817 IRH includes a larger error between DML16 and DML17.

5. CONCLUSIONS

We successfully used IPR to map the accumulation variation on the Amundsenisen plateau, increasing the spatial resolution of previous accumulation studies. Our results confirm findings of earlier studies that IPR surveys are capable of providing detailed information on surface mass-balance rates along continuous linear profiles, which cannot be provided by point sampling. Calculation of surface mass balance, however, still depends on an exact knowledge of the density–depth distribution along the survey route and dating of observed internal layers, which must be supplied by ice-core data. As radar surveys and point sampling of firn and ice cores along the route complement each other, the two methods should always be combined to ensure crosscheck measurements.

Naturally, small-scale variations cannot be resolved by wide-spaced sampling locations. In general, however, point measurements are capable of determining regional trends, associated with meteorological conditions rather than flow features. Interpolations may thus yield an overview of the general distribution of accumulation for wider areas. However, being susceptible to over- and underestimations due to outliers, these have to be taken with care. Future studies should be optimized by a well-balanced aerial sampling scheme, sufficient for applying more sophisticated interpolation algorithms based on geostatistical correlation analyses.

Small surface undulations caused by bedrock topography are likely responsible for variations of the accumulation pattern on the generally smooth high-altitude plateau of DML. Deriving the temporal variation of accumulation rates from either ice-core profiles or IRHs at different depths of the ice column therefore requires a detailed understanding of the interaction between bedrock relief and ice flow, resulting in surface undulations and thus disturbances in a homogeneous precipitation pattern. To overcome two-dimensional limitations of IPR surveys, either an aerial IPR survey set-up or satellite remote sensing should be applied to obtain a three-dimensional picture of the internal structure, and thus accumulation. This will require the interpretation of backscattering signatures of other radar sensors in connection with known accumulation patterns.

ACKNOWLEDEMENTS

Preparation of the manuscript profited greatly from discussions with W. Rack and D. Steinhage. The important contribution of the field parties during data acquisition is gratefully acknowledged. Preparation of this work was supported by Deutsche Forschungsgemeinschaft grant Ni493/1 and two scholarships of the Studienstiftung des Deutschen Volkes. This work is a contribution to the ‘European Project for Ice Coring in Antarctica’ (EPICA), a joint European Science Foundation (ESF))/European Commission (EC) scientific programme, funded by the EC and by national contributions from Belgium, Denmark, France, Germany, Italy, the Netherlands, Norway, Sweden, Switzerland and the United Kingdom. This is EPICA publication No. 116. Reprinted from the Annals of Glaciology with permission of the International Glaciological Society.

REFERENCES

Budd, W. F. and D. B. Carter. 1971. An analysis of the relation between the surface and bedrock profiles of ice caps. J. Glaciol., **10**(59), 197–209.

Eisen, O., U. Nixdorf, F. Wilhelms and H. Miller. 2002. Electromagnetic wave speed in polar ice: validation of the common-midpoint technique with high-resolution dielectric-profiling and γ-density measurements. Ann. Glaciol., **34**, 150–156.

Eisen O., U. Nixdorf, F. Wilhelms and H. Miller. 2004. Age estimates of isochronous reflection horizons by combining ice core, survey and synthetic radar data. J. Geophys. Res., **109**(B4). (10.1029/2003JB002858.)

Frezzotti, M. and O. Flora. 2002. Ice dynamic features and climatic surface parameters in East Antarctica from Terra Nova Bay to Talos Dome

and Dome C: ITASE Italian traverses. Terra Antartica, **9**(1), 47–54.

Frezzotti, M., S. Gandolfi and S. Urbini. 2002. Snow megadunes in Antarctica: sedimentary structure and genesis. J. Geophys. Res., **107**(D18). (10.1029/2001JD000673.)

Gudmandsen, P. 1975. Layer echoes in polar ice sheets. J. Glaciol., **15**(73), 95–101.

Isaksson, E., W. Karlén, N. Gundestrup, P. Mayewski, S. Whitlow and M. Twickler. 1996. A century of accumulation and temperature changes in Dronning Maud Land, Antarctica. J. Geophys. Res., **101**(D3), 7085–7094.

Liu, H., K. C. Jezek, B. Li and Z. Zhao. 2001. RADARSAT Antarctic Mapping Project digital elevation model. Version 2. Boulder, CO, National Snow and Ice Data Center.

Millar, D.H.M. 1981. Radio-echo layering in polar ice sheets and past volcanic activity. Nature, **292**(5822), 441–443.

Nereson, N. A., C. F. Raymond, R.W. Jacobel and E.D. Waddington. 2000. The accumulation pattern across Siple Dome, West Antarctica, inferred from radar-detected internal layers. J. Glaciol., **46**(152), 75–87.

Oerter, H. and 6 others. 2000. Accumulation rates in Dronning Maud Land, Antarctica, as revealed by dielectric-profiling measurements of shallow firn cores. Ann. Glaciol., 30, 27–34.

Pälli, A. and 6 others. 2002. Spatial and temporal variability of snow accumulation using ground-penetrating radar and ice cores on a Svalbard glacier. J. Glaciol., **48**(162), 417–424.

Richardson, C. 2001. Spatial distribution of snow in Antarctica and other glacier studies using ground-penetrating radar. (PhD thesis, Stockholm University.)

Richardson-Näslund, C., E. Aarholt, S.-E. Hamran, P. Holmlund and E. Isaksson. 1997. Spatial distribution of snow in western Dronning Maud Land, East Antarctica, mapped by a ground-based snow radar. J. Geophys. Res., **102**(B9), 20,343–20,353.

Robin, G. de Q. and D. H. M. Millar. 1982. Flow of ice sheets in the vicinity of subglacial peaks. Ann. Glaciol., **3**, 290–294.

Robin, G. de Q., S. Evans and J. T. Bailey. 1969. Interpretation of radio echo sounding in polar ice sheets. Philos. Trans. R. Soc. London, Ser. A, **265**(1166), 437–505.

Robinson, E. S. 1966. On the relationship of ice-surface topography to bed topography on the South Polar plateau. J. Glaciol., **6**(43), 43–54.

Sommer, S. and 9 others. 2000. Glacio-chemical study spanning the past 2 kyr on three ice cores from Dronning Maud Land, Antarctica. 1. Annually resolved accumulation rates. J. Geophys. Res., **105**(D24), 29,411–29,421.

Steinhage, D., U. Nixdorf, U. Meyer and H. Miller. 1999. New maps of the ice thickness and subglacial topography in Dronning Maud Land, Antarctica, determined by means of airborne radio-echo sounding. Ann. Glaciol., **29**, 267–272.

Traufetter, F., H. Oerter, H. Fischer, R. Weller and H. Miller. 2004. Spatio-temporal variability in volcanic sulphate deposition over the past 2 kyr in snow pits and firn cores from Amundsenisen, Antarctica. J. Glaciol., **50**(168), 137–146.

Ühlein, S. 1999. Anwendung verschiedener Interpolationsverfahren im Geografischen Informationssystem (GIS) auf Akkumulationsdaten in Dronning Maud Land (Antarktis). (Diploma thesis, Bayerische Julius-Maximilians-Universität, Würzburg.)

Wilhelms, F. 2000. Messung dielektrischer Eigenschaften polarer Eiskerne Ber. Polarforsch./Rep. Pol. Res. 367, 1–171.

PAPER II

 IEEE Trans. Geosci. Remote Sens., **44**(4), 943-956.

Retrieving Snowpack Properties and Accumulation Estimates from a Combination of SAR and Scatterometer Measurements

G. Rotschky, W. Rack, W. Dierking, and H. Oerter

Abstract— **This study combines two satellite radar techniques, low resolution C-/Ku-band scatterometer and high resolution C-band SAR for glaciological studies, in particular mass-balance estimations. Three parameters expressing the mean backscattering and its dependency on azimuth and incidence angle are used to describe and classify the Antarctic ice sheets backscattering behavior. Simple linear regression analyses are carried out between ground truth accumulation data and the SAR backscattering coefficient along continuous profile lines. From this we parameterize the accumulation rate separately for certain snow pack regimes. We find that SAR data can be used to map mass balance changes, however only within limited areas. Applying this method therefore generally requires accurate ground truth for regional calibration together with additional information regarding mean air temperature or elevation. This investigation focuses on the area of Dronning Maud Land (DML), Antarctica. We present the first high resolution accumulation map based on SAR data for the surrounding area of the EPICA deep ice core drilling site Kohnen, which is compared to reliable ground truth records as well as to a surface-mass balance map interpolated from these at low resolution.**

Index Terms— **Mass Balance, Satellite Radar, Snowpack Properties, Antarctica**

I. Introduction

THE knowledge of Antarctic ice mass balance and its temporal variations is at present still insufficient for determining the ice sheets contribution to global sea level rise with high accuracy [40]. Ice-sheet modeling is uncertain due to missing small-scale data for most regions. Recently, traditional methods of accumulation measurements, i.e. stake line readings, or point sampling by snow pits and firn core drilling have been supplemented by ice-penetrating radar (IPR) studies capable of retrieving mass balance information along continuous profile lines [12], [31], [33], [38], [39], [41]. Despite these efforts, there is still a lack of surface-mass balance data at a resolution that is mapping the high spatial variability of accumulation rate. The latter was found to reach up to 50% over distances of a few kilometers [41], even under the homogenous meteorological and topographic conditions of Dronning Maud Land's (DML) plateau region. Therefore it is questionable how representative single point measurements are for large-scale accumulation compilations, considering their coarse sampling scheme. The reconstruction of paleoclimate records from ice cores relies on detailed information of their accumulation history. If the drilling takes place on moving ice, the long term accumulation variability detected in an ice core arises as a combination of true climatical changes as well as movement of the core-hole site through a given surface-mass balance pattern upstream [20], [28], [44]. Since the latter depends on irregular surface undulations on a km scale [20], [41] a spatial resolution of accumulation data better than 1 km would be desirable in order to be able to identify and remove the effects of local topography and ice flow on accumulation time series. At present maps at this resolution are not available.

In order to overcome these uncertainties and to recover spatiotemporal ice sheet volume variations has become a major goal of current space borne earth observation methods, in the first instance carried out by passive, [5], [55], and active microwave instruments [6], [8], [11], [30], [47], [48], [53]. Although much effort has been done to assess the principles of microwave interaction with snow and ice, they are not yet completely understood in all their complexity [1]. In general, microwave signatures depend on the angular distribution of energy due to scattering at the surface and in the firn pack as well as on absorption

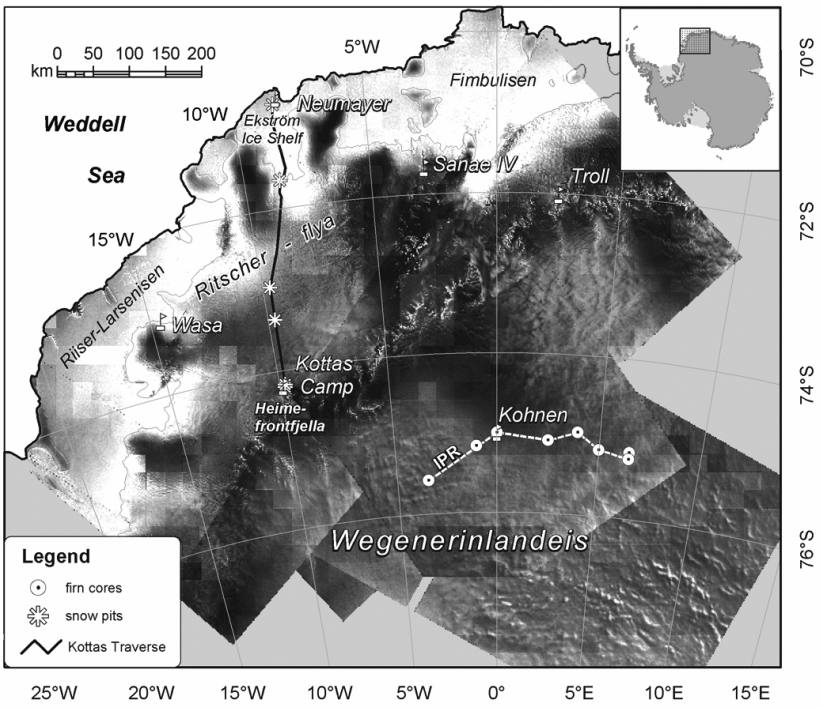

Fig. 1. Envisat ASAR mosaic of study region, Dronning Maud Land, showing several AWI snow pit and firn core sampling sites, as well as routes of stake readings (black line) and IPR (white striped line) providing ground truth data on accumulation rates. The ASAR images have been normalized to a single incidence angle of 35° and an azimuth angle of maximum backscattering for each pixel respectively as described in the text.

losses. Within the dry snow zone, the accumulation rate is seen as a key factor that determines the morphological structure of the snow pack. Spatiotemporal variations in snow deposition are therefore expected to have a major impact on the radar backscattering. The capability of microwave remote sensing for estimating snow accumulation has been recognized as a result of the reported inverse correlation between the backscattering coefficient σ^0 and accumulation rate [3], [8], [11], [23], [26], 30].

For the case of dry snow, the surface scattering in C- and Ku- Band can be neglected [10], [13]. The volume scattering is dominated by Rayleigh scattering, although Mie Scattering may play a role in Ku-Band for a grain size larger than 5 mm [50]. Taking into account the typical volume densities of the snow pack, permittivity and extinction properties are to be calculated based on the dense medium transfer theory [10]. In order to obtain more realistic estimates of the backscattering of deep dry snow packs, density-stratified layers have to be considered in model calculations [3], [52]. Reference [9] applied a least squares inversion technique to derive snowpack properties, such as accumulation for the dry snow zone of Greenland. Their method relies on simulating the variations of the microwave intensity due to seasonal changes of the snowpack. However, the absolute magnitude of backscattering intensity could not be reproduced by the model.

We aim at extending previous studies in order to classify regions with a similar nature of backscattering over the Antarctic ice sheet. Our attempt is the combination of overlapping scatterometer images at different frequencies in order to define snow pack classes by three parameters. Although the spatial resolution of scatterometers is low, they provide valuable information regarding backscattering at high temporal and geometrical resolution, which can be linked to snow pack properties, i.e. characteristics like snow grain size, density, subsurface layering, water content or surface roughness [8], [19], [21], [23], [25]-[27], [37], [42], [54]. Within defined snow regimes we investigated the relationship between SAR backscattering and snow pack properties, in the first place using accumulation rates derived by stake readings and IPR. This was conducted for two traverse routes, (1) leading from the German Neumayer station (70°39'S, 08°15'W) located on the Ekström Ice Shelf to the German Kottas camp (74°12'S, 9°44'W),

and (2) between various firn core locations on the high plateau of DML passing the Euopean Project of Ice Coring (EPICA) drilling camp Kohnen (75°S, 0°) (Fig.1).

II. DATA AND METHODS

A. Scatterometer Data & Image Reconstruction

We used VV-polarized 5.3 GHz (C-band) Escat and overlapping 14 GHz (Ku-band) Nscat data acquired during a full repeat cycle in winter 1997 to characterize the backscattering properties of the ice sheet, expressed by the normalized radar cross section σ^0. During this time, the snow pack is completely frozen and holds stable conditions [8]. Small variations due to wind drift were not considered. Both sensors have been reported to be steady in calibration, precise enough for our purposes [24], [49].

The Escat sensor (ERS-2 Active Microwave Instrument in wind scatterometer mode) measures the surface backscattering with three right-looking antennas over a single 500 km-wide swath to a southernmost extent of 79.5°S, and with a nominal resolution of 50 km [2]. The Nscat instrument onboard the Japanese Advanced Earth Observation Satellite (ADEOS-1) operated with two 600-km-wide swaths on both sides of the satellite track, separated by a 400 km gap. Six VV- and two HH-polarized antenna beams cover Antarctica to within 1.2° of the pole. Despite of the short mission duration (September 1996 to July 1997), the Nscat time series enable more detailed studies of electromagnetic scattering properties, due to its higher spatial resolution of 25 km and broader azimuth and incidence angle coverage.

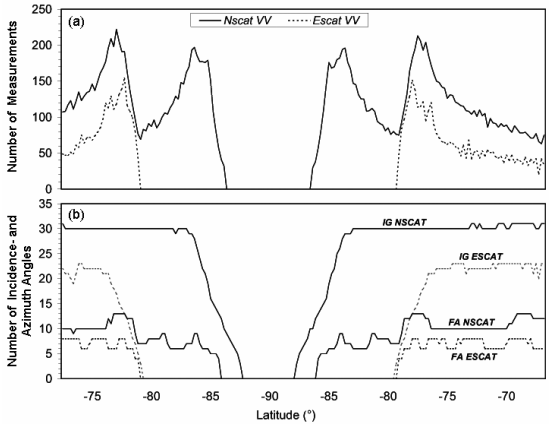

Fig. 2. Number of (a) σ^0_{mean} measurements and (b) covered incidence angles and azimuth-angle bins included in each image grid cell following the 90°E and 90°W meridians across Antarctica.

In order to obtain a complete set of possible viewing angles for a particular footprint of each sensor, the acquisition time intervals include a 35-day period for Escat (28th May to 30th June 1997) and 41-days for Nscat (20th May to 30th June 1997). Small acquisition gaps for Nscat were neglected. For the analysis, the single beam measurements were gridded at a resolution of 25 km, using a polar stereographic projection with the true scale set to 71°S for minimizing distortions within the DML study region. At each grid cell all observations within the imaging period are summed and then averaged in order to obtain a mean backscattering response.

Following [36] and [43], three slightly modified parameters have been calculated for each grid cell in order to characterize the backscattering: the mean backscattering coefficient σ^0_{mean} (dB) within the incidence-angle range of 30 to 40 degrees over all viewing angles α, the factor of anisotropy (*FA*), and the incidence angle gradient (dB·deg^{-1}), in the following named *IG*. The latter was evaluated by applying a 1st order least-square fit over all σ^0 measurements within the incidence angle range of $20° \le \theta \le 50°$, for which σ^0 (dB) was found to decrease almost linearly [3], [23], [26]. *FA* describes the azimuthal modulation of σ^0 and is calculated according to

$$FA = \frac{\sum_{j=1}^{18} \left| \sigma^0_{\Delta\alpha_j,mean} - \sigma^0_{mean} \right|}{\sigma^0_{mean}} \quad (1)$$

where $\Delta\alpha_j$ stands for 18 azimuth-angle bins in 20° steps. This way we obtained three images for each sensor, mapping the spatial distribution of backscattering characteristics. The number of measurements which enter the computation is represented in Fig. 2, following a meridian across the Antarctic continent. Variations occur according to the satellite-swath geometry, e.g. for calculating σ^0_{mean} the number of records ranges from 19 to 227 for Nscat and from 12 to 180 for Escat, respectively. Towards the imaging limits the number of covered incidence angles

decreases, e.g. for Escat, south of 78.8°S no incidence angles higher than 30° are available. Estimating Escat *FA* becomes critical at certain locations, because of the limited azimuth viewing geometry. At no point a number of 8 out of 18 possible azimuth-angle bins is exceeded for this sensor. Two sample locations, Neumayer station and Kohnen camp, give an impression on data density and distribution over the viewing angle ranges (Fig. 3).

B. ENVISAT ASAR Normalization

Envisat ASAR VV-Pol wideswath data acquired in March 2004 were calibrated and gridded to a 100 m and 250 m raster, respectively. Geocoding was done using the RAMP digital elevation model [22]. The speckle noise was reduced by applying a 3x3 running mean. The locational accuracy of the geocoded product is estimated to be within 100 m according to ground truth data. ASAR data were normalized to a uniform incidence angle (35°) and azimuth angle (0°), using our Escat backscattering parameters *IG* and $\sigma^0_{\Delta\alpha j}$. This approach is based on the assumption that the dependence of backscattering on viewing geometry as observed for larger areas from satellite is comparable to the small scale situation, which is justified by ground based scatterometer measurements for *IG* in DML [42]. We assume that the same is valid for *FA*. We carried out a pixel to pixel comparison of overlapping ASAR tracks covering homogenous areas near Kohnen station. By this process we found the local variations of *IG* to be in the order of 0.1 dB·deg^{-1}, inducing a normalization error small enough to be of minor significance in this area. We note that further field data are necessary to fully evaluate the uncertainty due to the use of low-resolution data in high-resolution applications. Normalization to an incidence angle of 35° for an entire image was carried out according to

$$\sigma^0(35°)_{0°\le\phi\le360°} = \sigma^0(\theta) + IG(35° - \theta). \quad (2)$$

Parameter θ describes the local incidence angle between surface normal and look vector at each image pixel. Variations of σ^0 versus azimuth angle are determined by a non-linear least square function of the form

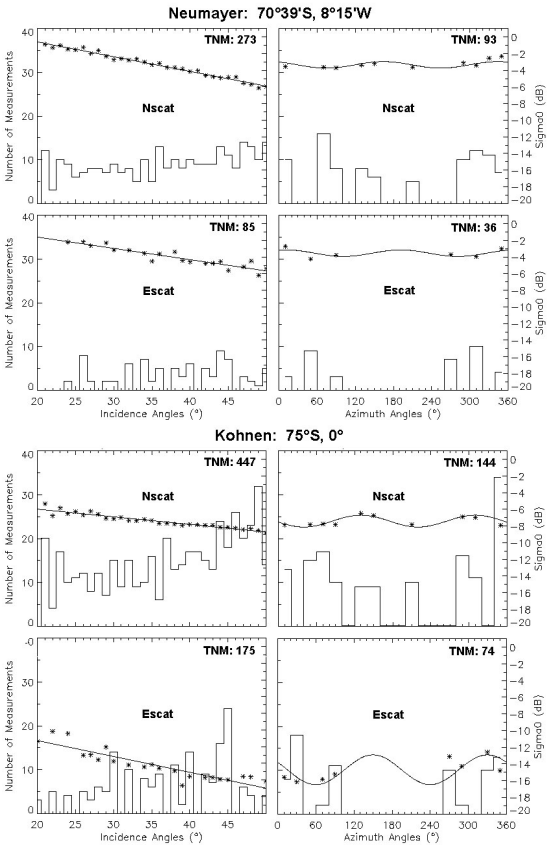

Fig. 3. σ^0 and number of measurements that entered computation of *IG* (left side) and *FA* as well as σ^0_{mean} (right side) as function of incidence and azimuth angles for two sample image pixels (25 x 25 km²), corresponding to the location of Neumayer and Kohnen station. The total number of measurements (TNM) is given at the upper right corners.

$$\sigma^0(\phi) = A + B\cos(2(\phi - C)) \quad (3)$$

where ϕ stands for the azimuth-look angle measured from north, and the coefficients A, B and C express the backscattering and its anisotropy. The function given in (3) was fitted to our Escat data within the incidence angle range of 30-40°, averaged for areas of 25 x 25 km² over the entire imaging period.

C. Ground Truth Data

Various ground truth data collected in DML in the framework of the EPICA pre-site survey are available for the period 1996 to 1999. The field studies have been continued and extended in the years after. Here we use data on the ice sheets annual surface mass balance and snow layer structure based on

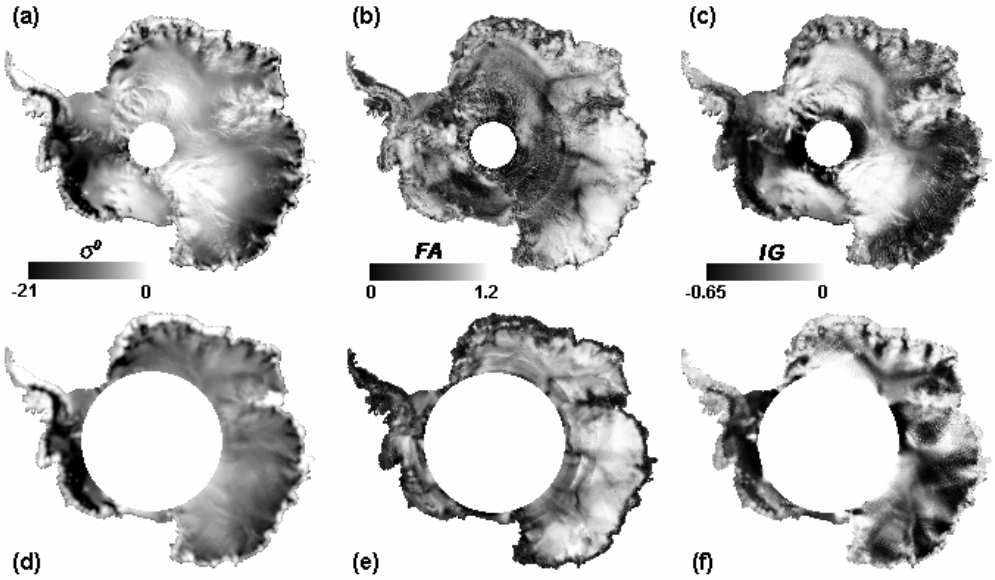

Fig. 4. Parameter images derived from VV polarized scatterometer images: a) Nscat σ^0_{mean}, b) Nscat *FA*, c) Nscat *IG*, d) Escat σ^0_{mean}, e) Escat *FA*, f) Escat *IG*.

snow pit studies, stake line readings, and IPR, making available an excellent basis for correlating accumulation rates with our satellite data.

A line of 675 stakes at 500-m intervals was set up along the Neumayer-Kottas camp traverse route, providing a mass balance transect of high spatial resolution with annual readings between 1999-2001. The stake measurements (in m) have been converted to accumulation rates (in kg m^{-2} a^{-1}) by integration of density profiles, derived from several snow-pit sites along the way (third order polynomial functions were fitted to density data for each site covering the upper 1.4 to 2 m of the snowpack). Together with the ice the stakes are moving towards the coast with an average speed of 52.4 m a^{-1}, increasing to 168 m a^{-1} beyond the grounding line on the Ekström Ice Shelf. Because of these position changes with time, the annual accumulation records were assigned to fixed geographic locations along the transect with 500 m spacing by linear interpolation. On the plateau around Kohnen station, an IPR derived surface mass balance profile serves as ground truth for comparison, covering a time span of 182 and 184 years, respectively [41].

TABLE I
CORRELATION COEFFICIENTS BETWEEN DERIVED PARAMETERS

Nscat / Escat			***Nscat***	***Escat***
σ^0_{mean}	0.84	σ^0_{mean} /*FA*	-0.51	-0.40
FA	0.72	σ^0_{mean} /*IG*	0.78	0.45
IG	0.48	*FA/IG*	-0.56	-0.15

III. RESULTS

A. *Frequency dependent differences in Backscattering*

The spatial patterns in our σ^0_{mean}, *FA* and *IG* parameter maps (Fig. 4) reflect differences in snow morphology, i.e. surface roughness, density, layering, and/or grain size [36]. This is due to variable conditions in local climate, wind and accumulation rate which are governed by geographic location, slope, elevation and orographic effects as well as surface undulations. Artefacts visible within the *FA* images are caused by sudden changes in the number of covered azimuth-angles subjected to the orbit geometry (see also Fig. 2b), e.g. for Nscat a drop from 13 to only 7 covered azimuth-angle bins causes a concentric feature at 79°S. We did not consider these distortions to be a crucial factor for the further analysis, since general changes in backscattering are still evident and no distortions are visible within the classification results, presented below.

Despite differences in spatial resolution and frequency between both sensors, the results display the same general features for all three parameters. They are consistent with previous findings [25], [26], [36], [43]. In Table I we list the correlation coefficients between the C- and Ku-band results as well as for all parameters to each other, separated for each sensor. The low correlation for *IG* between both sensors is likely due to differences in penetration depth within the dry snow zone. In general Escat derived parameters are less correlated to each other than those of Nscat, which could partly be a consequence of the lower spatial resolution and azimuth coverage. A significant correspondence is observed for the Nscat derived parameters σ^0_{mean} and *IG*. Field measurements in C-band show that low backscattering of a homogenous snow pack is often combined with high *IG* and vice versa [42]. In spite of this fact we used all parameters as input for a classification as described below, since the information used is not fully redundant.

Large areas of extremely high backscattering in the interior regions of East Antarctica can be observed in the Nscat result only (Fig. 4a). Consequently, here we find the strongest frequency differences in backscattering, reaching values of up to 8.5 dB (Fig. 5). Interestingly also the ice divides take shape clearly as regions of high σ^0_{mean} differences with $\sigma^0_c < \sigma^0_{ku}$ by 4-6 dB. Backscattering differences are small within regions affected by strong katabatic air flow, as well as within the percolation zone. In agreement with observations in Greenland [25], we find large areas with $\sigma^0_{Ku} < \sigma^0_C$ within the percolation zone (also marked in Fig. 5). During our imaging interval Ku-band is probably mainly reflected by a relatively homogenous winter snow layer, whereas for C-band buried layers of older firn and melt features act as strong scatterers. In opposite, within the dry snow zone, the backscattering level of Escat is in general lower compared to the Nscat data, as observed as well by [3], [26], [42]. An exception from this is a smaller region in Queen Mary Land (100°E), exhibiting at the same time high values for *FA*.

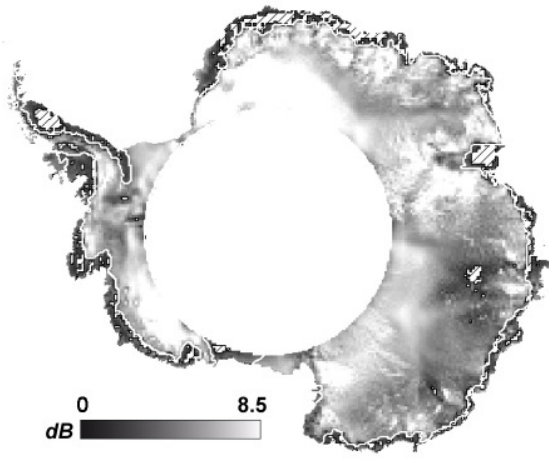

Fig. 5. Frequency difference image Nscat minus Escat including the percolation zone boundary as defined in the text. Areas of $\sigma^0_{ku} < \sigma^0_c$ are marked by white striped signatures.

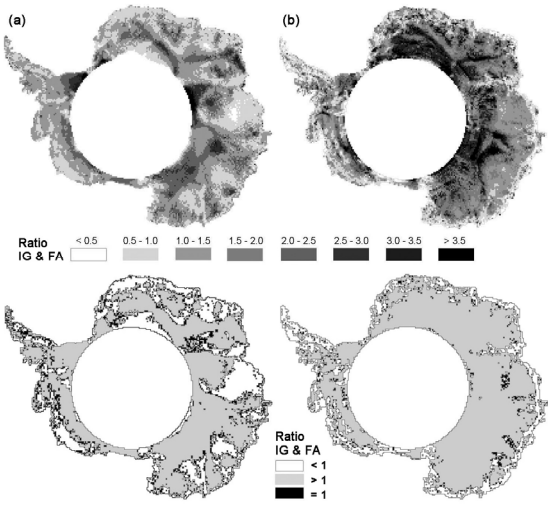

Fig. 6. (a) Ratio *IG* Escat / *IG* Nscat & (b) Ratio *FA* Escat / *FA* Nscat. Values < 1 indicate areas with higher dependence on viewing geometry (incidence and azimuth angles) for the smaller Ku-band wavelength.

In accordance to [8] for Greenland we defined the dry snow zone boundary as mapped in Fig. 5 by using a frequency-difference threshold of $\sigma^0_{ku} - \sigma^0_c > 1.8$ dB. In addition we utilized the fact that low values for *FA* are another specific feature of areas affected by summer melt. Therefore we used a value of Escat *FA* < 0.3 for further delimitation of the percolation zone. Remaining scattered areas which have been misselected using this approach were removed manually.

Smooth *IG* is observed at the high elevation areas of dense stratification on the East Antarctic Plateau. Large negative values of this parameter are found within the dry snow

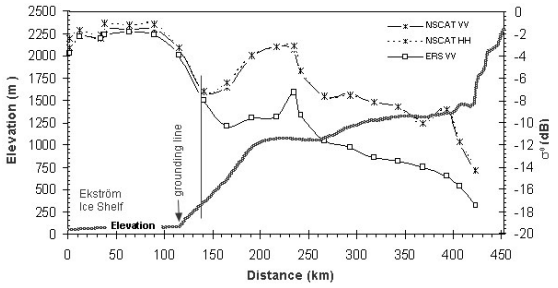

Fig. 7. σ^0_{mean} and elevation change along a traverse route from Neumayer station to Kottas camp. Topographic information was taken from RAMP Digital Elevation Model [22].

zone if the accumulation rate is relatively high. By looking at the lower image of Fig. 6a, it becomes evident that *IG* Nscat is steeper than *IG* Escat within regions where effective scattering layers close to the surface can be expected reducing the penetration depth especially for the higher frequency. Those are: (1) the katabatic wind regions of East Antarctica due to wind glazed surfaces and roughness features, such as sastrugi, (2) the percolation zone (buried ice lenses, pipes and layers), as well as (3) the high elevation plateau regions of intense backscattering, for which large snow crystals within the upper snow pack can be assumed [45]. In opposite, for regions missing such features *IG* Escat is generally steeper then *IG* Nscat, with biggest differences for flat regions, namely along the crest of the ice divides, as well as the Ronne ice shelf. Our findings agree with field studies carried out by [42], who found the incidence angle dependence increasing together with penetration depth. Reference [8] related a steeper gradient of σ^0 versus incidence angle with increasing accumulation rates, accompanied with a reduction of grain size and hence reduced backscattering.

Patterns of increased *FA* are generally accompanied by a steeper *IG* for both sensors, with the exclusion of Princess Elizabeth Land (70°-90°E) for Escat. Differences in *FA* betweenboth sensors are strongest in areas of largest penetration depth differences linked with very low accumulation rates. Regions of *FA* Nscat > *FA* Escat are restricted almost exclusively to the percolation zone near the coast (see lower image of Fig. 6b).

Figure 7 shows a comparison of σ^0_{ku} to σ^0_c along a transect from Neumayer station on the Ekström Ice Shelf to Kottas camp. From the grounding line at a distance of 120 km south of Neumayer, the ice sheet is rising in steps from the flat ice-shelf area to an elevation of about 2000 m a.s.l. The boundary between the coastal percolation zone to the dry snow zone is marked by the sudden divergence of our scatterometer profiles. Within regions affected by summer melt, buried ice lenses and hoar layers act as strong scatterers and prevent microwaves from deeper penetration into the snow pack. Further upslope above 400 m a.s.l., where mean annual air temperatures do not exceed –10°C [23], frequency differences in backscattering response become recognizable, due to differences in penetration depth. The cross over to dry snow conditions with increasing altitude occurs with a remarkable drop in σ^0 from –2 dB to –10 dB for Escat and to -7 dB for Nscat. Within the dry snow zone $\sigma^0_{ku} > \sigma^0_c$ is generally observed, but both curves progress parallel, with a differences of up to 6.2 dB. A notable sudden rise in backscattering between 150-250 km from the starting point can be observed for both wavelengths, but is less pronounced for the longer wave Escat data. This could partly be a consequence of the difference in spatial resolution between both sensors. Furthermore a comparison with accumulation measurements suggests that within this range of our transect a decrease in net mass balance to values as low as 60 kg m^{-2} a^{-1} (section *IV A*) might cause changes in grain size and layering in an order that primarily affects the shorter wave Ku-band [8]. The Nscat backscattering is almost independent of polarization which was also observed in Greenland [46], with slight differences in backscattering of up to 0.8 dB only within the coastal percolation zone.

B. Snow Pack Classification

We applied a Maximum Likelihood classification to our data by combining images of σ^0_{mean}, *IG* and *FA*. This way regions of comparable backscatter response could be delimited for the Antarctic ice sheet as shown in Fig. 8. As in [36] signature values for 10 classes were forced by training areas with pronounced backscattering behavior, which were identified by first applying unsupervised K-Means and Isodata classification algorithms. This way we compensated for missing a priori knowledge about the number,

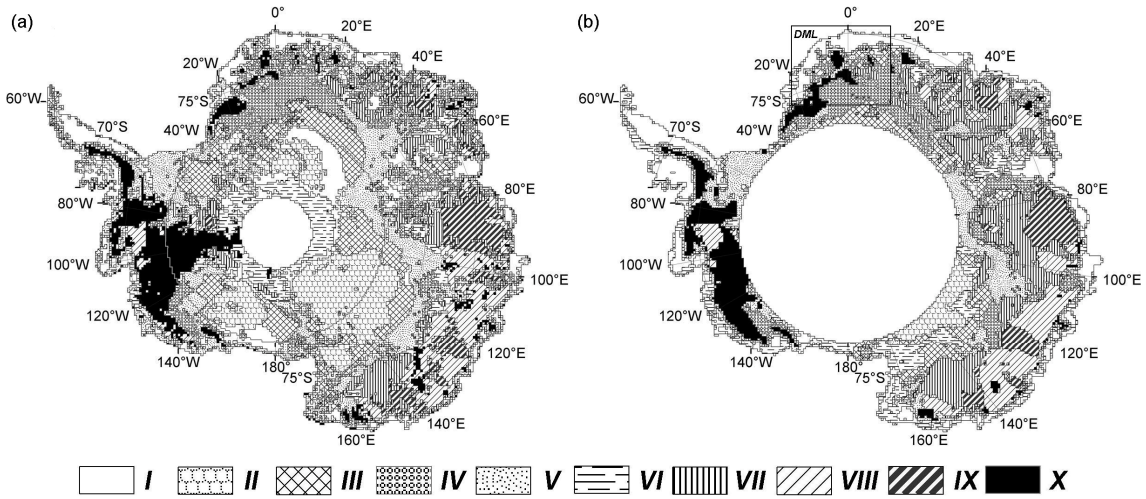

Fig. 8. Maximum Likelihood classification of Antarctic snow pack regimes, resulting from input parameters *FA, IG* and σ^0_{mean} for (a) Nscat with Escat viewing limits marked by a circle, and (b) Escat. The latter also shows the extent of our DML study region.

position and extent of existing unique backscattering types.

The results yield a similar general pattern of surface classes for both VV polarized Escat C-band and Nscat Ku-band scatterometer data, in spite of differences in spatial resolution, viewing angle coverage, and geometry between both sensor types. This implies that the dominant backscattering mechanisms are the same for both frequencies. Thus we consider this simple method as robust for mapping different Antarctic snow facies, even for the less well resolved Escat data. However, the higher resolution Nscat data enable a more detailed discrimination of the single classes shape and extent up to a southern limit of 86°S. Figure 9 maps areas that are classified as the same type by both sensors, making up 48.4% of the area common to both sensors.

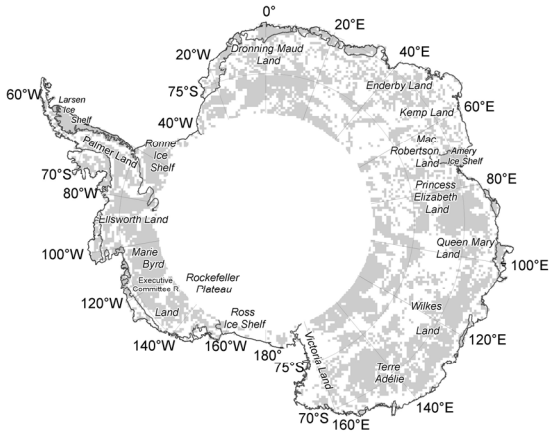

Fig. 9. Areas of agreement (gray) and disagreement (white) between Escat and Nscat Maximum Likelihood classification results.

Differences in the allocation of pixels to a certain class concern regions where the crossover from one surface type to another is not very distinct, expressed by similar cluster means for all three parameters as shown in Table II. Those are the low accumulation dry snow areas with homogenous snow pack

TABLE II
MAXIMUM LIKELIHOOD CLUSTER MEANS

Nscat

Class	σ^0_{mean}	*St. Dev*	***FA***	*St. Dev*	**IG**	*St. Dev*
I	-2.68	1.05	0.12	0.05	-0.16	0.02
II	-1.68	0.82	0.07	0.03	-0.11	0.01
III	-4.30	0.68	0.09	0.03	-0.14	0.02
IV	-6.35	1.23	0.16	0.04	-0.14	0.02
V	-6.72	1.36	0.14	0.05	-0.19	0.02
VI	-6.88	2.21	0.18	0.09	-0.23	0.07
VII	-6.93	1.29	0.34	0.06	-0.22	0.05
VIII	-11.88	1.54	0.39	0.12	-0.25	0.04
IX	-9.36	1.66	0.61	0.09	-0.23	0.03
X	-12.92	1.62	0.17	0.07	-0.26	0.08

Escat

Class	σ^0_{mean}	*St. Dev*	***FA***	*St. Dev*	***IG***	*St. Dev*
I	-3.23	1.59	0.10	0.05	-0.15	0.03
II	-6.31	0.73	0.25	0.08	-0.16	0.05
III	-9.75	1.24	0.28	0.10	-0.18	0.07
IV	-11.92	1.21	0.39	0.07	-0.19	0.05
V	-11.13	1.62	0.29	0.15	-0.32	0.10
VI	-8.01	1.28	0.13	0.05	-0.19	0.05
VII	-10.70	1.10	0.59	0.10	-0.24	0.06
VIII	-14.27	1.34	0.55	0.11	-0.33	0.06
IX	-12.91	1.70	0.85	0.13	-0.17	0.04
X	-17.34	2.01	0.25	0.09	-0.30	0.08

morphology, represented by classes III-VII. Here it was difficult to decide for training areas that we assumed to be most representative for both frequencies. Nearly no correspondence was found for class VI for which only 10% of all pixels are in common for both sensors. The best agreement in classification is reached in three cases: (1) high accumulation areas within the dry snow zone covered by class X (in common: 57.9%), (2) areas with reduced penetration depth due to effective near surfaces scatterers, i.e. regions affected by summer melt (class I with 51.8% common pixels), and (3) areas with significantly increased *FA* due to the preferential alignment of surface roughness features (sastrugi) caused by persistent katabatic air flow (enclosed by classes VIII and IX – in common: 40.4% and 44.8%, respectively). A short description of typical surface properties for all classes is provided in Table III. However, such specifications are limited, since the transition from one surface type to another is smooth, and the spectrum of possible physical characteristics is large even within one class. Furthermore, available information is still insufficient for some classes.

TABLE III
CHARACTERISTICS OF SNOW PACK CLASSES

Class	*Percentage of surface*			*Accum.*	*Typical phys. properties*
	Escat	***Nscat*[1]**	***Nscat***	kg m^{-2} a^{-1}	
Total Area	95 x 10^5 [km²]		135 x10^5 [km²]		
I	10.14	10.45	11.40	high, in general > 150	percolation zone, highly metamorphosed, varying grain sizes, distinct ice lenses and pipes
II	4.31	6.07	12.12	very low, < 50	coarse grained, distinct stratification
III	11.85	10.30	13.16	low, in general < 150	no striking features or only sparse information on surface structure for classes III-VI
IV	11.77	12.04	9.50		
V	10.85	16.18	14.48		
VI	13.14	7.81	10.00		
VII	14.41	9.55	7.59	variable[2]	transition zone from katabatic wind to high plateau regions
VIII	9.74	11.45	8.37	variable[2]	wind erosion, and redistributional surface, large sastrugi
IX	5.10	6.70	4.82	variable[2]	wind glazed surfaces, sastrugi, irregular layering
X	8.70	9.46	8.56	very high in general > 200	small grains, homogenous snowpack

[1] area common to Escat; [2] due to persistent katabatic winds

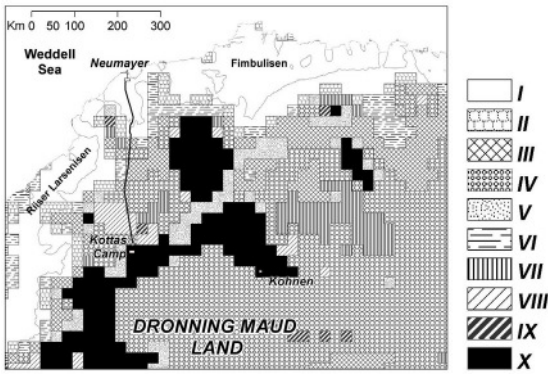

Fig. 10. Escat MLH Classification result for DML study region.

Regions exhibiting extreme values in one or more of our input parameters stand out clearly at both frequencies. The percolation zone is represented by class I, which is marked by a bright band of very high σ^0_{mean} at the margins of the continent, where the effects of rapid grain growth [17] and formation of ice lenses and pipes during the summer months combine to form strong scattering layers [8], [23], [42]. Examples are the Amery Ice Shelf (72°E) and the Larsen Ice Shelf on the Eastern coast of the Antarctic Peninsula (64°W), or several smaller ice shelf areas aligned along the DML coast. Small *FA* illustrates the isotropic scattering of this surface type. In addition frequency differences in σ^0_{mean} are small, suggesting that the penetration depth is similar for both frequencies, hence the scattering is dominated by an upper surface layer.

Also class II is evolving from high backscattering together with low *FA* and smooth *IG*. Here, Nscat σ^0_{mean} reaches its extremes of up to 0.5 dB, whereas Escat values are on the average 3 dB smaller than in the coastal area. Larger areas falling into class II are stretching from Victoria Land (160°E) up to the high plateau at 100°E, as well as starting on the Ross Ice Shelf up the slope toward the Rockefeller Plateau. Smaller areas are scattered on the high elevation plateau of DML south of 79°. Class II is restricted to regions exhibiting very low accumulation rates of generally less then 100 kg m^{-2} a^{-1} down to 5 kg m^{-2} a^{-1} [4], [14], [51] associated

with a dominance of coarse to very coarse snow grains, including the development of depth hoar. The steady increase in C-band backscattering observed towards the crest of the ice sheet was attributed to increased stratification of the snow pack by [42], as a result of decreasing accumulation rates and development of wind crusts. This assumption is confirmed by traverse studies [45] that found the number of strata within the upper 2 m to reach up to 60, with an average of 35. These findings compare with observations from central Greenland, where increased backscattering was also associated with intensified layering together with increased grain sizes due to low accumulation rates [11], [23]. Class I and II cluster means are not very distinct for Nscat and thus could not be correctly discriminated on the plateau area. The imaging geometry of Escat does not allow further mapping of this snow pack type.

In opposite, for the dry snow zone high accumulation rates can be linked to a compact firn-pack morphology with small grain sizes [7], [15], for which the penetration depth was described to be in the order of a few hundred times the wavelength [3]. Here the backscattering is only weak. Therefore, darker colours within the σ^0_{mean} parameter images (Fig. 4a) indicate regions of high accumulation and are mapped by class X, which is in addition characterized by an increased *IG*, confirming statements of [42] for a higher penetration depth. The largest connected areas of this kind are found in West Antarctica, i.e. Marie Byrd Land (100°-140°W), Ellsworth Land (80°-100°W), and Palmer Land (65°W). In agreement for both frequencies, the lowest values of σ^0_{mean} (Escat –22.5 dB / Nscat –17.4 dB) are observed in Marie Byrd Land at two locations within the Executive Committee Range between 76°30'S and 77°S at 121°W and 132°W, where an accumulation maximum of 560 kg m^{-2} a^{-1} has been reported by [29]. Scattered areas are found in DML, where values of up to 593 kg m^{-2} a^{-1} have been measured by stake line readings in the year 2001 near the Heimefrontfjella mountain range (74°23'S/9°22'W).

In East Antarctica striking patterns are generated by regions of strong katabatic air flow, which causes a higher surface roughness. They are represented by classes VII, VIII, and IX, characterized by significantly increased values for *FA*. The dependence of this parameter on wind-generated features, i.e. sastrugi [26], [37] and snow dunes is well known [16]. Stronger slope gradients account for a first order azimuthal modulation of σ^0_{mean} [3], as well as a steeper *IG*. Escat data generally exhibits a significantly higher variation of σ^0 with azimuth angle than observed for the Nscat

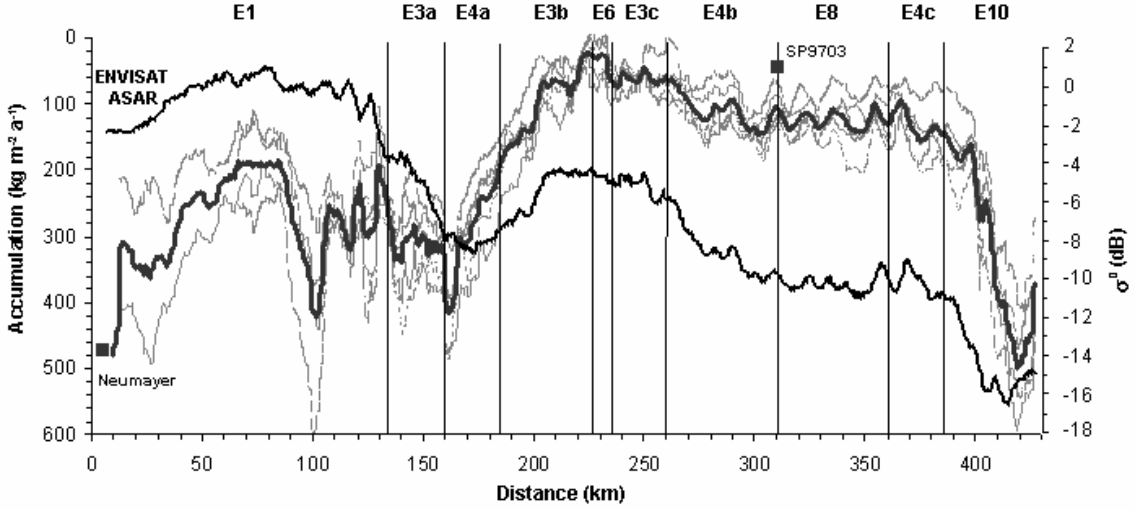

Fig. 11. Average net snow accumulation derived from stake readings along the Kottas Traverse route for the time period 1997-2001 (annual variability in gray), inversely plotted against ASAR wideswath σ^0 measurements (100 m pixel spacing) from March 2004 normalized to 35° incidence. Squares mark the locations of snow pits described in the text. The transect is subdivided into sections that correspond to the Escat derived snow pack classes with labels on top.

data, which might partly be an artefact of the lower azimuth-angle coverage (see Fig. 2b and Fig. 3) and therefore reduced accuracy in deduction of *FA*. Regions with highest anisotropy are combined in class IX, namely Wilkes Land (110°-130°E), Princess Elizabeth Land (70°-90°), and Terre Adélie (130°-145°E), known for their high wind-speeds near the margin of the ice sheet [34], [35], [37].

In East Antarctica, terrains on the coastal side of the ice divide exhibit strong variations in surface conditions. Here the classification algorithm produces a highly scattered small-scale pattern through all classes, especially for the Nscat data. No remarkable feature can be named from Mac Robertson Land (60°-80°E), over Kemb Land to Enderby Land (60-40°E). For DML (Fig. 10) our classification results differ between both sensors concerning the exact pixel location of a certain surface class only. This region is known for its high spatial variability in surface conditions, due to changes in local weather conditions, changing winds and accumulation rates [32], [39], governed by orographic effects and surface undulations. For this sample region ground truth data is available, crossing from the coastal percolation zone to the dry snow zone on the polar plateau. With these we can link our snow pack classes derived from satellite measurements and address uncertainties regarding their morphological differences.

IV. DETERMINING ACCUMULATION RATES VIA SAR

A. Transect Neumayer – Kottas

Annual stake readings covering a 5 year period from 1997 to 2001 provide detailed information on mass balance along a continuous profile line connecting the German station Neumayer, situated near the edge of the Ekström Ice Shelf, with the Kottas camp nearby the Heimefrontfjella mountain range. Traceable in Fig. 11 is the typical trend of decreasing snow accumulation with increasing elevation (also Fig. 7) and distance to the coast, described in further detail in [39]. Undulations appear on a km scale. Though a stronger inter-annual variability is recognizable, the general sequence of net accumulation rates along the transect is preserved over the years. A section of extraordinary strong variations can be observed between 90-170 km along the lower slope of the ice rise from the grounded coastal areas, probably due to increases in katabatic wind. Interestingly, years of above mean accumulation (1997, 1999, 2001) alternate with years of below mean accumulation (1998, 2000), with strongest amplitudes on the ice shelf in direct neighbourhood to the grounding line at a distance of 100 km from Neumayer station. Here, during the observation period, a maximum of 600 kg m^{-2} a^{-1} (1999) contrasts sharply with a

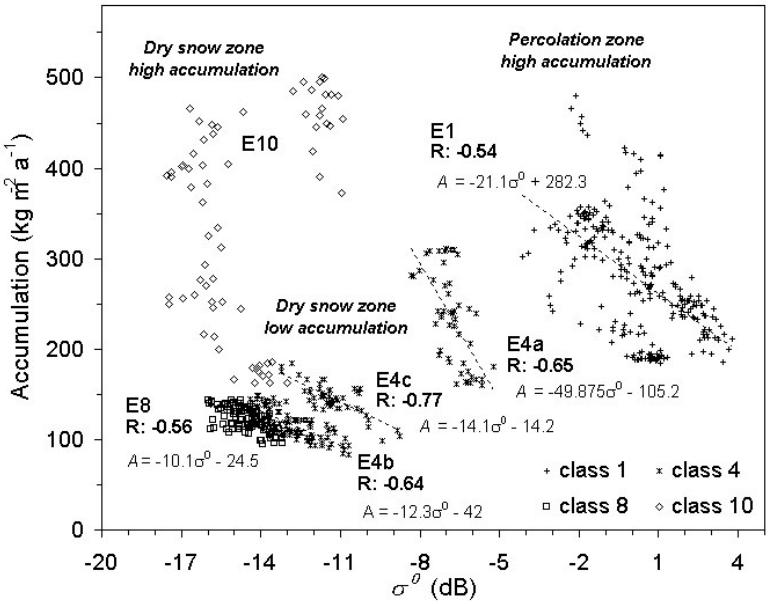

Fig. 12. Scatterplot of ASAR σ^0 values vs. stake line net accumulation rates. Clusters correspond to the Escat derived snow pack classes (also Fig. 11).

minimum value of only 273 kg m^{-2} a^{-1} in the following year, giving an indication for the high temporal variability of snow accumulation within this region. Within a section of lowest accumulation along the stake line (225-233 km) the situation is reversed. While during 1999 ablation is observed (-7 kg m^{-2} a^{-1}), a record of 84 kg m^{-2} a^{-1} is reached in the year 2000, emphasizing the role of snow redistribution by wind, which modifies the original precipitation pattern and causes a coincidental chronology of annual net mass balance rates for a certain location along a profile. In the Kottas mountains at the end of the stake line, the local terrain and wind field generate a sudden rise in net snow accumulation, reaching average values up to 500 kg m^{-2} a^{-1}.

A varying snow accumulation can be related with changes in snow pack properties, in particular the annual layer thickness, grain size and hence density-depth distribution. As observed earlier by Antarctic and Greenland ice sheet studies [3], [8], [11], [23], [30], [54], such changes are mirrored by the corresponding backscattering signatures, which show a clear rise in σ^0 with decreasing snow accumulation. Larger grain sizes and a higher number of strata per depth unit are thought to cause an increased volume scattering, accompanied with a reduction of penetration depth. Comparing the average snow accumulation rate along the Neumayer - Kottas camp stake line with our normalized ASAR data we also observe a remarkable reciprocal relationship between both datasets. Both curves progress in the same directions, when accumulation measurements are plotted inversely against the radar coefficient σ^0 (in dB) as shown in Fig. 11.

When looking at the correlation factors, the percolation zone (R: -0.55), with well-developed scattering layers near the surface, must be separated from the dry snow zone with R: -0.74. The crossover between those snow facies is roughly marked by the border between the Escat derived classes III and IV (km 160) at an elevation of around 650 m a.s.l.. Going more into the detail, we studied the relationship of accumulation and backscattering within our Escat derived snowpack classes separately as illustrated in Fig. 12. Distinct clusters form here according to differences in snow morphology. For those classes which exhibit a good correlation between radar backscattering and surface net balance, we established simple linear regression functions to parameterise the accumulation. Class I, representing the flat Ekström Ice Shelf, separates as an agglomeration of rather scattered points on the right side, exhibiting a correlation factor R of -0.54. Within this area σ^0 is generally higher than within the dry snow zone, regardless of snow accumulation rate. Snow pit studies at several points along our stake line reveal the snow packs typical stratigraphic layering and density distribution with depth, of which examples are presented in Fig. 13a. Near Neumayer station there is evidence that high summer temperatures alter the snow pack in a way that contributes to stronger backscattering response. The snow was described as coarse-grained material, containing a series of up to 2 cm thick ice lenses, starting at a distance of only a few centimetres from the surface. A mean density of 420 kg m^{-3} was found within the snow pack's upper 2 m.

In contrast, for class X which is in the sphere of influence of the Heimefrontfjella mountain range, the lowest values of σ^0 are recorded, although accumulation rates are comparably high. For this region no correlation between both datasets was observed, since local effects cause spatially highly variable snow deposition and hence snow pack conditions, which cannot be resolved in the classification procedure by scatterometer data. No density distribution is available for this surface type, but the snow pack is described as consisting mainly of loose, homogenous, fined grained (< 1 to 2 mm) snow crystals. Only one thin layer of consolidated material was found within the upper 1.5 m at a depth of 1 m.

The highest correlation of up to –0.77 was found for lower accumulation areas within the dry snow zone, covered by spatially separated sections of class IV. The different alignment of surface roughness features towards north (simulated sensor look direction) induces a parallel shift along the σ^0-axis from section E4b to E4c in Fig.12. Our findings are consistent with a previous study [11], that found backscattering to be generally more sensitive to changes in accumulation when the accumulation rate is low (100 to 250 kg m^{-2} a^{-1}). The correlation becomes highest for regions with little slope and smooth topography. Snow pit SP9703

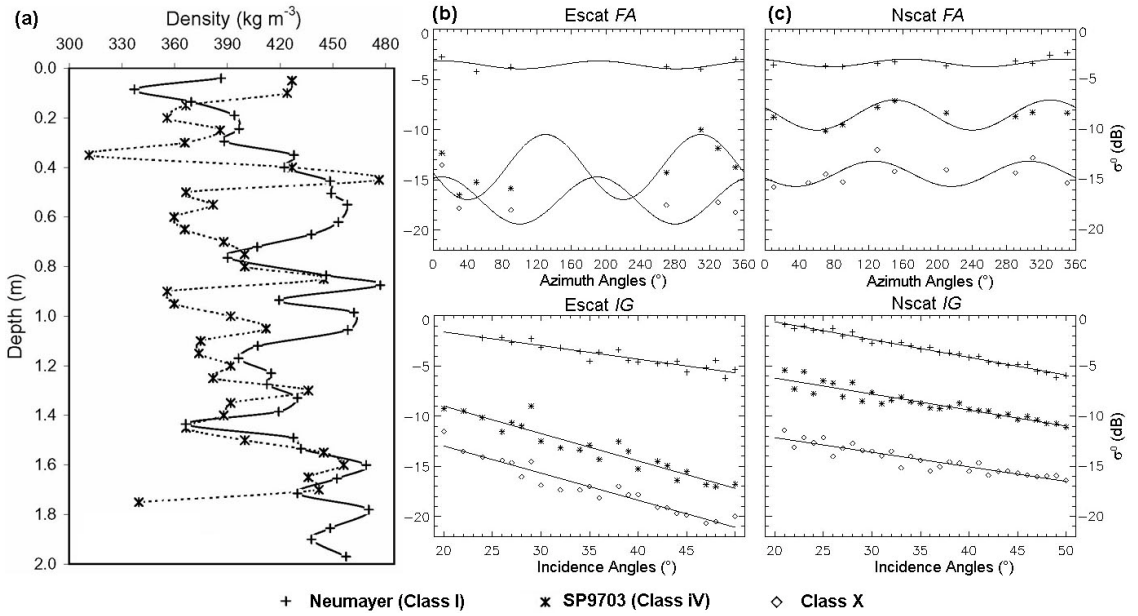

Fig. 13. (a) Depth-density profiles for 2 snow pits, located along Kottas Traverse route and corresponding (b) Escat and (c) Nscat scatterometer signatures *FA* (on top) and *IG* (on bottom).

(elevation: 1250 m a.s.l.) reveals for this snow pack type a series of alternating high-density layers of fine grains and lower density, coarse-grained firn, caused by annual and seasonal varying wind and temperature conditions. Additionally a number of 7 wind crusts of less than 1 mm thickness are found at several depths over the upper 2 m of the snow pack. The average density is 390 kg m^{-3}, significantly lower than within the percolation zone.

The corresponding scatterometer derived values for *FA* and *IG* (Fig. 13b and c) show for class I very little anisotropy and a flat decrease of σ^0 versus incidence angle, i.e. small *IG*, linked to a high backscattering level of up to 0 dB. Within the dry snow zone (class IV and X) we find the backscattering reduced with a significant change in *IG* only for the Escat data. *FA* is high for both sensors, with larger amplitudes in C-band.

B. Transect Kohnen

A second area arranged to class IV using Escat and Nscat data, is situated on the Wegenerinlandeis plateau around Kohnen station. For this region a transect of ground truth data obtained by IPR is available for comparison with ASAR data. In order to reduce noise both datasets have been smoothed using a 2 km running mean. In spite of similar backscattering characteristics, we find altered parameterisations between ground truth accumulation rates and ASAR measurements according to

$$A = a\sigma^0 + b. \quad (4)$$

Our transect of 320 km length can be subdivided into 3 sections using a scatterplot of accumulation versus ASAR σ^0 similar to Fig. 12. For these we find coefficients *a* and *b* as listed in Table IV. Here we compare our results with subdivision E4c along the lower elevation Neumayer-Kottas traverse, which exhibits comparable topographical conditions and slope (1.6 m km^{-1}). Again we find a clear inverse response of backscattering to changes in accumulation rate. Furthermore we notice a trend of increasing backscattering with elevation (Fig. 14a). This cannot be caused by accumulation changes, which exhibit irregular variations but show no certain tendency along the entire transect according to ground data

TABLE IV
REGRESSION COEFFICIENTS BETWEEN ACCUMULATION RATE *A* AND BACKSCATTERING COEFFICIENT σ^0 (SEE (4)) FOR SECTIONS OF CLASS 4

	a	***b***	***R***	***a′***	***b′***	***R′***
Kottas	-14.1	-14.2	-0.77	-	-	-
Kohnen						
S1 (0 – 48.5 km)	-6.53	-45.3	-0.88	-7.5	-61.3	-0.92
S2 (48.5 – 87 km)	-3.76	-1.0	-0.77	-4.4	-13.7	-0.82
S3 (87 – 320 km)	-0.73	49.4	-0.24	-2.3	23.6	-0.52

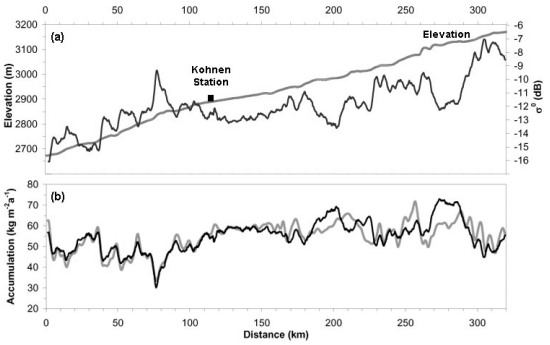

Fig. 14. (a) Elevation and ASAR σ^0 (on a 250 m grid) normalized to an overall incidence angle of 35° and 0° azimuth angle along the IPR route, and (b) IPR derived accumulation data (gray line) [41] compared to accumulation estimations based on ASAR data (black line).

(Fig. 14b). Removing this trend from our satellite data and adjusting the regression coefficients to a' and b', we can improve the correlation coefficients (R') between ASAR data and accumulation, especially for the third section (87 - 320 km).

Backscattering has also been linked to the mean annual air temperature [11], [30], for which elevation can serve as a proxy. Introducing the elevation H as a second parameter additional to the radar backscattering coefficient for performing a multivariate regression analysis, we yield good accumulation estimates based on

$$A = -6\sigma^0 + 0.088H - 275. \quad (5)$$

Our accumulation calculations resulting from ASAR and elevation data compare well with surface mass balance rates derived by IPR. Both curves progress parallel, with an average difference of ± 6.4%. The accuracy of IPR data has been estimated to be within 5-10% (personal communication Dr. Olaf Eisen). The maximum disagreement is -13.74 kg m^{-2} a^{-1} (21.73%) occurring at 302 km. This close approach is surprising, considering the difference in spatial resolution between IPR and our satellite data. The latter corresponds to an integration of backscattering responses over an area of 250 x 250 m².

The accuracy is higher as long as the transect is running parallel to satellite swath (up to km 150 from starting point), therefore differences within the second part of our profile line might partly result from an incomplete incidence angle normalisation. The latter introduces an error of up to 1 dB for incidence-angle corrections being in the order of 10 degrees along the transect (see section *II.B*), which corresponds to an accumulation error of about 6 kg m^{-2} a^{-1} according to (5) for a typical value of σ^0 along the transect. Another source of discrepancies are differences in temporal resolution between both datasets. Our IPR data cover a time span of about 185 years, based on an isochrone at an average depth of 25 m [41]. This corresponds roughly to the penetration depth of C-band in polar firn [42]. Thus, the volume contributing to the backscattering theoretically covers a comparable time span, but can easily vary due to effective scattering layers near the surface, e.g. caused by depth hoar. Such changes in penetration depth and therefore backscattering strength might be the reason for significant divergences of ground-truth and calculated accumulation-profile lines, e.g. occurring between 180 to 230 km or around 280 km from starting point. Since exact information on real penetration depth are not available, such estimates based on radar data must always be taken with care.

C. SAR based accumulation map

Based on (5), we calculated the spatial pattern of accumulation at a horizontal resolution of 250 m for an area as large as 70 x 10^3 km² surrounding our IPR transect (Fig. 15a) and being included in class IV. In order to assess the accuracy of our product we judge the accumulation obtained from SAR at locations for which independent field measurements are available (Table V). These data were mainly derived from shallow firn cores, many of which go back more than 180 years, thus covering a time span comparable to our IPR data. The difference between ground truth records and SAR derived accumulation rates varies on average by 19%, ranging from -42.7% to 31%. The accuracy is found to be non-systematic and irrespective of both (1) the distance between point accumulation measurements and IPR transect (used for calibrating the SAR signals), as well as (2) the accumulation time span that is covered by firn and snow pit samples. The same sources of discrepancies apply as mentioned above for the transect

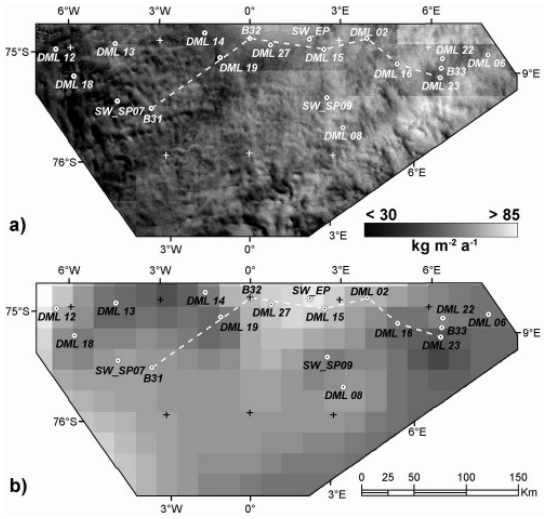

Fig. 15. Accumulation maps based on (a) SAR data and (b) interpolation from point records [18]. Firn core B32 is situated 1.6 km west of Kohnen station.

Kohnen including the accuracy of field measurements, which we cannot quantify.

The same field records were used to interpolate an accumulation grid at 20 km resolution [18] with which we compare our SAR derived accumulation map. This low-resolution dataset has until now been the best source of information for ice-sheet modelling within this region. We find that with use of SAR data not only small-scale accumulation variations are now visible, but also a significantly different accumulation pattern is revealed. While in Fig. 15a a clear increase in accumulation can be observed towards the East of our study area, the situation seems to be reversed in Fig. 15b. In total the accumulation sums up to 3.67 Gt a^{-1} versus 4.4 Gt a^{-1} from [18], corresponding to a difference of 20%. This result gives an indication for the present uncertainties in quantification of ice-sheet mass balance.

V. SUMMARY

This paper combines satellite borne radar data with ground truth mass balance information derived by annual stake line readings, firn cores and geophysical field surveys carried out by IPR. Our aim was to study the spatial distribution of different snow pack regimes over the Antarctic ice sheet and assess surface mass balance variations, in particular throughout the DML region. We used Escat and Nscat data in order to identify regions with similar backscattering behavior by three parameters (σ^0_{mean}, azimuth and incidence angle dependence of backscattering *FA* and *IG*), which are similarly mapped by both C-band and Ku-band sensor types. Thus, by applying a Maximum Likelihood classification we produce comparable results, showing that despite a limited imaging geometry also Escat is a useful tool to carry out snow pack studies. Distinctions depending on frequency can be explained largely by differences in penetration depth and therefore in the volume contributing

TABLE V
MEASURED (A_{PT}) VERSUS SAR DERIVED ACCUMULATION (A_{SAR}) IN kg m^{-2} a^{-1} ON AMUNDSENISEN PLATEAU

Name	*Lon*	*Lat*	*Time Period*	*Time Span*	A_{pt}	A_{SAR}	*Diff. [%]*
B31	03°26'W	75°35'S	1801-1997	196	59	55	-7.2
B32	00°01'E	75°00'S	1816-1997	181	62	55	-11.1
B33	06°30'E	75°10'S	1801-1997	196	47	55	16.5
DML 02	03°55'E	74°58'S	1919-1995	76	57	52	-9.0
DML 06	08°01'E	75°00'S	1899-1996	97	50	66	31.0
DML 08	03°17'E	75°45'S	1819-1996	77	60	67	12.3
DML 12	06°30'W	75°00'S	1816-1998	182	62	35	-42.7
DML 13	04°30'W	75°00'S	1800-1997	197	47	45	-5.1
DML 14	01°30'W	74°57'S	1801-1997	196	53	38	-28.0
DML 15	02°30'E	75°05'S	1801-1997	196	64	65	1.0
DML 16	05°00'E	75°10'S	1816-1997	181	48	62	28.4
DML 18	06°00'W	75°15'S	1801-1997	196	50	41	-19.0
DML 19	01'00'W	75°10'S	1810-1997	187	44	39	-11.9
DML 22	06'30'E	75°05'S	1801-1997	196	58	64	10.2
DML 23	06°30E	75°15'S	1816-1997	181	38	50	30.4
DML 27	00°42'E	75°03'S	1935-1999	64	68	53	-22.0
SW_07[1]	04°35'W	75°30'S	1982-1993	11	60	38	-37.5
SW_09[1]	02°41'E	75°30'S	1980-1993	13	50	61	22.4
SW_EP[1]	02°00'E	75°00'S	1865-1991	126	77	64	-16.5

[1] obtained by SWEDARP – Swedish Antarctic Research Program

to the backscattering as well as by differences in scattering mechanisms at internal interfaces and grains. Related to this fact the single frequencies may be responding to different periods in recent snow-accumulation history, what was however not examined in this study.

The scatterometer derived parameters *IG* and *FA* were also used to normalize Envisat ASAR wideswath data to unique incidence and azimuth angles for a test site in DML. Our studies confirm inverse correlations between ASAR backscattering and snow accumulation rates, which become strongest within low-accumulation dry snow zone areas. Our hypothesis, that within classes of similar backscattering behavior unique parameterisations can be established between accumulation rates and backscattering amplitude, can only be partly confirmed. Though we can delimit areas for which we find simple functions for estimating surface mass balance changes, the ability to transfer these from one region to another is limited. The reason for this is that beside the accumulation rate, further parameters which vary spatially in number and composition alter the snow-pack backscattering properties, such as the presence of small-scale surface roughness features or buried effective scattering layers, i.e. ice lenses, depth hoar or wind crusts. Furthermore, the terrain is changing the local incidence angle in a way that is not taken into account by our scatterometer derived normalization procedure. On the higher elevation plateau area of DML, a steadily decreasing mean annual air temperature with increasing elevation introduces a linear trend in σ^0, which overlays the irregular signal undulations caused by varying accumulation rates. Both observed signature responses are mostly controlled by grain-size variations [21].

For a test site in Dronning Maud Land we have derived the first high resolution accumulation map based on SAR and ground truth data. Even in this area with a comparably dense network of ground measurements, the spatial characteristics and the magnitude of accumulation differs significantly from previous interpolations of accumulation point measurements. This suggests, that accumulation compilations from single point records can be misleading if their area of validity is left unconsidered.

VI. CONCLUSION

SAR measurements can be utilized to map surface mass balance, most suitably within lower accumulation areas of the dry snow zone. However, the relationship between accumulation rate and backscattering is not unique over the entire spectrum of possible Antarctic snow pack conditions. The mean annual air temperature, which is highly dependent on elevation is a parameter that must further be considered in this context. It is therefore obvious that parameterizations of accumulation rates via SAR data can be established only for areas of limited extent that can be defined using low resolution scatterometer data. The inclusion of surface heights as a fourth parameter beside σ^0_{mean}, *FA*, and *IG*, for classifying Antarctic snow pack types might improve the discrimination of snow regimes that exhibit similar backscattering characteristics, in spite of different snow morphology.

A strong advantage of SAR derived accumulation estimates at high resolution is the ability to distinguish climatically caused accumulation changes from those related to small scale surface undulations upstream of a drilling site. This is of great relevance for the climatic interpretation of deep ice core records, such as obtained by the EPICA project. They could serve as well for validation of output from atmospheric numerical models. For regional calibration of radar signals, accurate ground truth data on accumulation are needed, preferably along continuous profiles lines. In this we see the major problem in application of our method.

However our findings are also useful by examining the surrounding backscattering pattern of accumulation point measurements. This would indicate the degree to which the latter can be considered to be representative on the regional scale, even if the spatial variability of snow accumulation cannot be quantified. With regard to Ku-Band, the detected small scale variations in snow pack properties will be useful for the analysis of high resolution radar altimeter data like from the forthcoming Cryosat mission.

ACKNOWLEDGMENT

SAR data were provided by ESA within the Cryosat Cal/Val AO. Scatterometer data were made available by the Physical Oceanography Distributed Active Archive Center (PO.DAAC) for Nscat, and by the French Processing and Archiving Facility (IFREMER) for Escat. We thank Dr. Olaf Eisen for providing mass balance information by means of IPR data. Ground truth accumulation data for sites 07 / 09 and SW were provided by SWEDARP. We also thank two anonymous reviewers for valuable comments on the manuscript.

REFERENCES

[1] R. J. Arthern, D. J. Wingham, and A. L. Ridout, "Controls on ERS altimeter measurements over ice sheets: Footprint-scale topography, backscatter fluctuations, and the dependence of microwave penetration depth on satellite orientation", *J. Geophys. Res.*, vol. 106, no. D24, pp. 33471-33484, 2001.

[2] E. P. W. Attema, "The active microwave instrument on-board the ERS-1 satellite," *Proc. IEEE*, vol.79, pp. 791–799, June 1991.

[3] A.W. Bingham and M. Drinkwater, "Recent changes in the microwave scattering properties of the Antarctic ice sheet," *IEEE Trans. Geosci. Remote Sensing*, vol. 38, no. 4, pp. 1810–1820, July 2000.

[4] D. H. Bromwich, "Snowfall in high southern latitudes," *Rev. Geophys.*, vol. 26, no. 1, pp. 149-168, 1988.

[5] J. C. Comiso , H. J. Zwally, and J. L. Saba, "Radiative Transfer Modelling of microwave emission and dependence on firn properties," *Ann. Glaciol.*, vol. 3, pp. 54-58, 1982.

[6] C. H. Davis, C. A. Kluever, B. J. Haines, C. Perez, and Y. Yoon, "Improved elevation change measurement of the southern Greenland ice sheet from satellite radar altimetry," *IEEE Trans. Geosci. Remote Sensing*, vol. 38, no. 3, pp. 1367–1378, May 2000.

[7] D. J. Drewry., S. R. Jordan, and E. Jankowski, "Measured properties of the Antartic ice sheet: surface configuration, ice thickness, volume and bedrock characteristics," *Ann. Glaciol.*, vol. 3, pp. 83-91, 1982.

[8] M. R. Drinkwater, D. G. Long, and A.W. Bingham, "Greenland snow accumulation estimates from satellite radar scatterometer data", *J. Geophys. Res.*, vol. 106, No. D24, pp. 33 935–33 950, 2001.

[9] J. D. Flach, K. C. Partington, C. Ruiz, E. Jeansou, and M. R. Drinkwater, "Inversion of the Surface Properties of Ice Sheets from Satellite Microwave Data", I *IEEE Trans. Geosci. Remote Sens*ing., vol. 43, no. 4, pp. 743-752, April 2005.

[10] D. Floricioiu and H. Rott, "Seasonal and short-term variability of multifrequency, polarimetric radar backscatter of Alpine terrain from Sir-C/X-SAR and AIRSAR data," *IEEE Trans. Geosci. Remote Sens*ing, vol. 39, no. 12, pp. 2634-2648, December 2001.

[11] R. Forster, K. C. Jezek, J. Bolzan, F. Baumgartner, and S. P. Gogineni, "Relationships between radar backscatter and accumulation rates on the Greenland ice sheet," *Int. J. Remote Sens.*, vol. 20, pp. 3131–3147, 1999.

[12] M. Frezzotti and O. Flora, "Ice dynamic features and climatic surface parameters in East Antarctica from Terra Nova Bay to Talos Dome and Dome C: ITASE Italian traverses," *Terra Antartica*, vol. 9, no. 1, pp. 47-54, 2002.

[13] A. K. Fung and K. S. Chen, "Dependence of the surface backscattering coefficients on roughness, frequency and polarization states," I*nt. J. Remote Sensing*, vol. 13, no. 9, pp. 1663-1680, 1992.

[14] M. B. Giovinetto and H. J. Zwally, "Spatial distribution of net surface accumulation on the Antarctic ice sheet," *Ann. Glaciol.*, vol. 31, pp. 171–178, 2000.

[15] I. D. Goodwin, "Ice sheet topography and surface characteristics in eastern Wilkes Land, East Antarctica," *ANARE Res. Notes,* vol. 64, 1988.

[16] I. D. Goodwin, "Snow-accumulation variability from seasonal surface observations and firn-core stratigraphy, eastern Wilkes Land, Antarctica," *J. Glaciol.*, vol. 37, no. 127, pp. 383-387, 1991.

[17] J. Gow, "On the rates of growth of grains and crystals in south polar firn," *J. Glaciol.*, vol. 8, no.33, pp. 241–252, 1969.

[18] P. Huybrechts, D. Steinhage, F. Wilhelms, and J. Bamber, "Balance velocities and measured properties of the Antarctic ice sheet from a new compilation of gridded data for modelling," *Ann. Glaciol.*, vol. 30, pp. 52-60, 2000.

[19] K. C. Jezek, P. Gogineni, and M. Shanableh, "Radar measurements of melt zones on the Greenland ice sheet," *Geophys. Res. Lett.*, vol. 21, no. 1, pp. 33–36, 1994.

[20] J. C. King, P. S. Anderson, D. G. Vaughan, G. W. Mann, S. D. Mobbs, and S. B. Vosper, "Wind-borne redistribution of snow across an Antarctic ice rise," *J. Geophys. Res.*, vol. 109, no. D11104, doi:10.1029/2003JD004361, 2004.

[21] B. Legrésy and F. Rémy, "Using the temporal variability of satellite radar altimetric observations to map surface properties of the

Antarctic ice sheet," *J. Glaciol,*. vol. 44, no. 147, pp. 197-206, 1998.

[22] H. Liu, K. Jezek, B. Li, and Z. Zhao, "Radarsat Antarctic Mapping Project digital elevation model version 2," Digital media, National Snow and Ice Data Center, Boulder, CO, USA, 2001.

[23] D. G. Long and M. R. Drinkwater, "Greenland ice-sheet surface properties observed by the Seasat-A scatterometer at enhanced resolution", *J. Glaciol*., vol. 40, no. 135, pp. 213–230, 1994.

[24] D. G. Long and G. B. Skouson, "Calibration of spaceborne scatterometer data using tropical rainforests," *IEEE Trans. Geosci. Remote Sensing,* vol. 34, no. 2, pp. 413–424, Mar. 1996.

[25] D. G. Long and M. R. Drinkwater, "Cryosphere applications of NSCAT data," *IEEE Trans. Geosci. Remote Sensing*, vol. 37, no. 3, pp.1671–1684, May 1999.

[26] D.G. Long and M. R. Drinkwater, "Azimuth variation in microwave scatterometer and radiometer data over Antarctica," *IEEE Trans. Geosci. Remote Sen*sing, vol. 38, no. 4, pp. 1857–1870, July 2000.

[27] C. Mätzler, "Applications of the interaction of microwaves with the natural snow cover," *Remote Sens. Rev*., vol. *2*, pp. 259–392, 1987.

[28] K. Melvold, J. O. Hagen, J. F. Pinglot, and N. Gundestrup, "Large spatial variation in accumulation rate in Jutulstraumen ice stream, Dronning Maud Land, Antarctica," *Ann. Glaciol.*, vol. 27, pp. 231-238, 1998.

[29] E. Mosley-Thompson, J. Dai, L. G. Thompson, P. M. Grootes, J. K. Arbogast, and J. F. Paskievitch, "Glaciological studies at Siple Station (Antarctica): potential ice-core paleoclimatic record," *J. Glaciol.*, vol. 37, no. 125, pp. 11-22, 1991.

[30] J. Munk, K.C. Jezek, R. R. Forster, S. P. Gogineni, "An accumulation map for the Greenland dry-snow zone facies derived from spaceborne radar," *J. Geophys. Res.*, vol. 108, no. D9, pp. ACL 8 1-12, 2003.

[31] N. A. Nereson, C. F. Raymond, R. W. Jacobel, and E.D. Waddington, "The accumulation pattern across Siple Dome, West Antarctica, inferred from radar-detected internal layers, " *J. Glaciol.*, vol. 46, no. 152, pp. 75-87, 2000.

[32] H. Oerter, F. Wilhelms, F. Jung-Rothenhäusler, F. Göktas, H. Miller, W. Graf, and S. Sommer, "Accumulation rates in Dronning Maud Land as revealed by dielectric-profiling measurements of shallow firn cores," *Ann. Glaciol.*, vol. 30 , pp. 27–34, 2000.

[33] A. Pälli, J. C. Kohler, E. Isaksson, J. C. Moore, J. F. Pinglot, V. A. Pohjola, and H. Samuelsson, "Spatial and temporal variability of snow accumulation using ground-penetrating radar and ice cores on Svalbard glacier," *J. Glaciol.*, vol. 48, no. 162, pp. 417-424, 2002.

[34] T. R. Parish, "Surface airflow over East Antarctica," *Mon. Weath. Rev.*, vol. 110, pp. 84-90, 1982.

[35] T. R. Parish and D. H . Bromwich, "The surface windfield over the Antarctic ice sheet," *Nature*, vol. 328, pp. 51–54, 1987.

[36] W. Rack, "Streuverhalten und Morphologie der Antarktischen Schneedecke aus Scatterometer-Messungen von ERS-1," MSc. thesis, Univ. Innsbruck, Innsbruck, Austria, 1995.

[37] F. Rémy, M. Ledroit, and J. F. Minster, "Katabatic wind intensity and direction over Antarctica derived from scatterometer data," *Geophys. Res. Lett.*, vol. 19, pp. 1021–1024, 1992.

[38] C. Richardson, E. Aarholt, S.-E. Hamram, P. Holmlund, and E. Isaksson, "Spatial distribution of snow in western Dronning Maud Land, East Antarctica, mapped by a ground-based snow radar," *J. Geophys. Res.*, vol. 102, no. B9, pp. 20 343-20 353, 1997.

[39] C. Richardson-Näslund, "Spatial characteristics of snow accumulation in Dronning Maud Land, Antarctica", *Global and Planetary Change*, vol. 42, pp. 31-43, 2004.

[40] E. Rignot and R. H. Thomas, "Mass Balance of Polar Ice Sheets," *Science*, vol. 297, pp. 502-506, 2002.

[41] G. Rotschky, O. Eisen, F. Wilhelms, U. Nixdorf, H. Oerter, "Spatial distribution of surface mass balance on Amundsenisen plateau, Antarctica, derived from ice-penetrating radar studies," to be published in *Ann. Glaciol.,* vol. 39, 2004.

[42] H. Rott, K. Sturm, and H. Miller, "Active and passive microwave signatures of Antarctic firn by means of field measurements and satellite data," *Ann. Glaciol.,* vol. 17, pp. 337–343, 1993.

[43] H. Rott and W. Rack, "Characterization of Antarctic Firn by Means of ERS-1 Scatterometer Measurements," in: *Proceedings of International Geoscience and Remote Sensing Symposium, 10-14 July 1995, Florence, Italy*, IEEE Publications, vol. 3, pp. 2041-2043, 1995.

[44] V. B. Spikes, S. Arcone, A. Hamilton, P. Mayewski, D. Dixon, and S. Kaspari, "Spatial and temporal variability in West Antarctic snow-accumulation rates," to be published in *Ann. Glaciol.*, vol. 39, 2004.

[45] S. Surdyk and M. Fily, "Comparison of the passive microwave spectral signature of the

Antarctic ice sheet with ground traverse data," *Ann. Glaciol.*, vol. 17, pp. 161-166, 1993.

[46] C. T. Swift, P. S. Hayes, J. S. Herd, W. L. Jones, and V. E. Delnore, "Airborne mircrowave measurements of the Southern Greenland ice sheet," *J. Geophys. Res.*, vol. 90, pp. 1983-1994, 1985.

[47] R. Thomas, C. Davis, W. Krabill, and J. McConnell, "Greenland Ice Sheet Elevation Change Since 1978 from Radar and Laser Altimetry," *Polar Geography*, vol. 23, no. 3, pp. 169-184, 1999.

[48] R. Thomas, B. Csatho, C. Davis, C. Kim, W. Krabill, S. Manizade, J. McConnell, and J. Sonntag, "Mass balance of higher-elevation parts of the Greenland ice sheet," *J. Geophys. Res.*, vol. 106, no. D24, 33 707-33 716, 2001.

[49] W. Tsai, J. E. Graf, C. Winn, J. N. Huddleston, S. Dunbar, M. H. Freilich, F. J. Wentz, D. G. Long, and W. Linwood Jones, "Postlaunch Sensor Verification and Calibration of the NASA Scatterometer," *IEEE Trans. Geosci. Remote Sens*ing, vol. 37, no. 3, pp. 1517-1542, May 1999.

[50] F. T. Ulaby, R. K. Moore, and A. K. Fung, *Microwave Remote Sensing - Active and Passive*, Vol. 3. Reading, MA: Addison-Wesley Publishing Co., 1981.

[51] D. G. Vaughan, J. J. Bamber, M. B. Giovinetto, J. Russell, A. P. R. Cooper, "Reassessment of net surface mass balance in Antarctica," *J. Climate*, vol.12, pp. 933– 946, 1999.

[52] R. D. West, D. P. Winebrenner, H. Rott, "Microwave emission from density-stratified Antarctic firn at 6 cm wavelength", *J. Glaciol.*, vol. 42, no. 140, pp. 63, 1996.

[53] D. J. Wingham, A. J. Ridout, R. Scharroo, R. Arthern, and C.K. Shum, "Antarctic elevation change from 1992 to 1996," *Science*, vol. 282, pp. 456-458, 1998.

[54] V. R. Wismann and K. Boehnke, "Monitoring snow properties on Greenland with ERS scatterometer and SAR," *Eur. Space Agency Spec. Publ*., ESA SP-414, pp. 857–862, 1997.

[55] H. J. Zwally and M. B. Giovinetto, "Accumulation in Antarctica and Greenland derived from passive-microwave data: a comparison with contoured compilations," *Ann. Glaciol.*, vol. 21, pp. 123-130, 1995.

PAPER III

A new surface accumulation map for western Dronning Maud Land, Antarctica, from interpolation of point measurements

Gerit ROTSCHKY,[1] Per HOLMLUND,[2] Elisabeth ISAKSSON[3],
Robert MULVANEY,[4] Hans OERTER,[1] Michiel R. VAN DEN BROEKE,[5]
Jan-Gunnar WINTHER[3]

[1]*Alfred Wegener Institute for Polar and Marine Research, P.O. Box: 120161, 27515 Bremerhaven, Germany*
[2]*Department of Physical Geography, Stockholm University, S-106 91 Stockholm, Sweden*
[3]*Norwegian Polar Institute, Polar Environmental Centre, N-9296 Tromsø, Norway*
[4]*British Antarctic Survey, Natural Environment Research Council, Madingley Road, Cambridge CB3 0ET, England*
[5]*Institute for Marine and Atmospheric Research Utrecht, P.O. Box 80.005, Utrecht University, Princetonplein 5,3584 CC Utrecht, The Netherlands*

ABSTRACT. As a result of intensive field activities carried out by several nations over the last 15 years a set of accumulation measurements for western Dronning Maud Land (DML), Antarctica, was collected, based on firn-core drilling and snow-pit sampling. This new information was supplemented by earlier data taken from the literature, resulting in 111 accumulation values. Using Geographical Information Systems software, a first region-wide mean annual snow-accumulation field was derived. In order to define suitable interpolation criteria, the accumulation records were analysed with respect to their spatial autocorrelation and statistical properties. The resulting accumulation pattern resembles well known characteristics such as a relatively wet coastal area with a sharp transition to the dry interior, but also reveals complex topographic effects. This work furthermore identifies new high-return shallow drilling sites by uncovering areas of insufficient sampling density.

INTRODUCTION

Over the last decades much effort has been put into recovering possible changes in the mass budget and dynamics of polar ice sheets in response to climate-change. Mass-balance estimates require knowledge of the amount and spatial distribution of snow accumulation, which still suffers from large uncertainties. Shallow firn and ice cores, supplemented by snow pits, are traditionally used to derive the accumulation and climate history throughout the last centuries. As a result from precipitation variations and wind-driven redistribution of snow, surface accumulation rate is spatially as well as temporally highly variable. Local values depend on the overall climate, regional weather conditions and terrain characteristics at macro to micro scale. For example, Reijmer and Van den Broeke (2003) found standard deviations in 4-7 years accumulation averages to range from 20% to 70% of the average annual accumulation, based on data of several automatic weather stations in Dronning Maud Land (DML). On an annual scale, large horizontal accumulation variations have been observed from stake measurements by Melvold and others (1998) reaching up to 500 kg m^{-2} a^{-1} over a distance of less then 3 km on Jutulstraumen. In this respect ice cores serve as a useful tool because they provide long-term averaged accumulation rates which more likely represent a typical value for their surrounding area. However, due to the time-consuming and often costly procedure of firn-core drilling, their numbers remain limited.

Sampling density of accumulation records varies strongly over the Antarctic ice sheet (Vaughan and others, 1999). Drilling sites are usually concentrated along traverse routes and easily accessible coastal regions. The sparse and uneven data distribution sets high demands on interpolation techniques used to map the broad scale accumulation distribution over wider regions. Furthermore it is

questionable, whether firn-core records covering different accumulation periods can be combined in a single map if trends in accumulation history cannot be precluded. Nevertheless, for most regions, firn cores still represent the only in-situ source of information that can be used for accumulation compilations.

DML has been under investigation by several countries over the last 50 years resulting in a large body of available literature. This region is particularly interesting because of its sensitivity to conditions over the Atlantic sector of the Southern Ocean, possibly connecting it with the climate record of the Greenland ice sheet. Field activities increased in the 1990's in the framework of the International Trans-Antarctic Scientific Expedition (ITASE), established in order to gain a greater understanding of Southern Hemisphere climate within the last 200 years, and due to pre-site surveys for the European Project for Ice Coring in Antarctica (EPICA), aiming at locating a suitable deep ice-core drilling site in the Atlantic sector of East Antarctica.

As more and more data on accumulation rates have successively been compiled each season, it becomes necessary to summarize and combine the information for a region wide picture and estimation of snow accumulation in DML. So far no accumulation map exists specifically for western DML that is based entirely on in-situ data. In this paper, we present a complete set of reliable accumulation records available at the time of this study for the western DML region. For a spatial interpolation we apply algorithms based on geostatistical methods and exploratory data analysis. By doing so we aim at recovering the large-scale accumulation pattern, resulting from overall climate, weather, and topographic conditions. Clearly, small scale accumulation variations cannot be resolved using point data. Prior to this our dataset is discussed in terms of its spatial and temporal validity. By this we justify the combination of unevenly distributed field data representing a variety of accumulation periods at each location.

GEOGRAPHICAL DESCRIPTION OF WESTERN DML

Morphology

The area of investigation is stretching inland from the Antarctic coast at 70°S to about

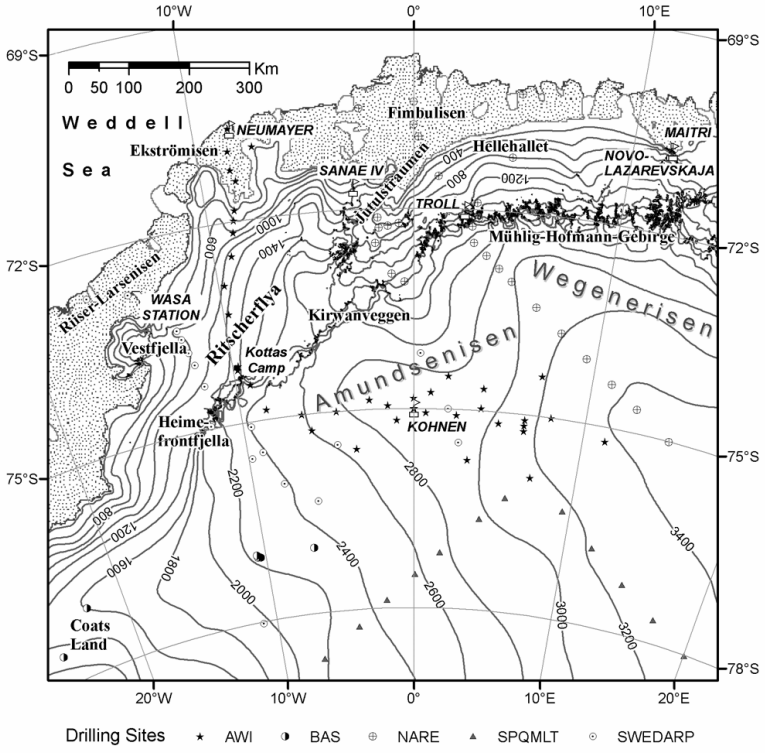

Figure 1. Area of investigation and sampling network. Varying symbols for point records were chosen in order to distinguish between different institutions involved in data acquisition. Elevation contours in 200 m intervals are given as solid black lines.

80°S, enclosed by the 20°W and 15°E meridians (Fig.1). Based on its topography, western DML can be subdivided into four regions: (1) the major ice shelves Riiser-Larsenisen, Ekströmisen, and Fimbulisen, (2) the lower inland ice regions Ritscherflya and Hellehallet, and (3) the high-altitude plateau area with an elevation above 2500 m a.s.l., i.e. the Wegener Inlandeis made up by Amundsenisen and Wegenerisen. A clear borderline between coastal / lower inland ice regions and the plateau consists of (4) the nunatak areas of the Heimefrontfjella, Kirwanveggen, and Mühlig-Hofmann-Gebirge mountain ranges, which penetrate the ice-sheet reaching heights of about 2700 m a.s.l.. Acting as a barrier to air masses approaching from the Weddell Sea and the Atlantic Ocean to the north this chain of mountains has large impact on the accumulation distribution, separating the area into two distinct accumulation regimes.

The surface topography of the plateau is smooth with wind-shaped features, i.e. small-size sastrugi (10-15 cm high) (Stenberg and others, 1998) indicating that the mean wind velocities in this part of Antarctica are moderate. Undulations with amplitudes on the metre-scale and wavelengths on the kilometre-scale have been linked to bedrock morphology (e.g. Budd and Carter, 1971; Rotschky and others, 2004). Large areas of Amundsenisen have been delineated as ice drainage basin feeding the Filchner Ice Shelf with the ice divide as far north as 75°S (Giovinetto and Bentley, 1985). Major outlets from Amundsenisen are Stancomb-Wills Ice Stream, draining into the Brunt Ice Shelf, and Jutulstraumen, feeding Fimbulisen. With an area of approximately 124 000 km², Jutulstraumen is the largest ice stream within our area of investigation. Topography varies much stronger coastward of the nunataks, where drainage basins alternate with mountain ridges. Varying slope gradients and aspects as well as a variable surface-wind field introduce complex patterns in the accumulation distribution (Van den Broeke and others, 1999).

General characteristics of snow accumulation

DML is situated in the Atlantic sector of Antarctica, and in the sphere of influence of cyclonic systems that move along the coast, the strongest winds blow from the east to northeast (Lunde, 1961). Field observations reveal a typical continental precipitation distribution with a general decrease in accumulation with increasing elevation and distance from the open ocean, and with decreasing mean annual air temperature, respectively (Giovinetto and others, 1990; Vaughan and others, 1999). In DML, the nunataks interrupt this steady modification by forcing the humid air masses to rise, resulting in accumulation extremes of up to 780 kg m^{-2} a^{-1} on Jutulstraumen, as reported by Melvold and others (1998) based on stakes measurements for a 1 year period. Large regional variations in accumulation occur in dependence of predominant cyclone pathways, topographic disturbances, and katabatic wind activity (Richardson and Holmlund, 1999; Van den Broeke and others, 1999; King and others, 2004). A detailed discussion of precipitation and related snow accumulation characteristics in DML was presented by Noone and others (1999).

SAMPLING FRAMEWORK

Our dataset includes accumulation data from snow pit studies as well as from firn and ice core drillings carried out by six nations during 20 different Antarctic field campaigns, held over a time period of about four decades. Compiled records are listed in the Appendix with a reference, tabulated by site name, campaign name and year of observation. Because of the susceptibility to errors we did not consider records based on snow pit stratigraphy alone. Results of this method have been criticised as being generally unreliable due to the subjective interpretation. Total obliteration of the annual layering resulting from strong metamorphism or wind erosion is held responsible for usual overestimations of accumulation rates derived from firn stratigraphy, particularly where accumulation is low (e.g. Picciotto and others, 1971; Giovinetto and Zwally, 2000; Frezzotti and others, 2004).

Sporadic visits to DML already began with the Norwegian-British-Swedish Antarctic Expedition in the years 1949-52, however, systematic data acquisition on accumulation did not start before the late 1960's. The earliest reliable dataset originates

from the third leg of the U.S. South Pole-Queen Maud Land traverse (SPQMLT 1964-68) covering the southernmost part of the area of interest between 75°S to 80°S and between 10°W to 40°E on Amundsenisen (Picciotto and others, 1971). Here the dating of 17 snow pits was based on total β-activity deposited after nuclear weapon tests. Data acquisition continued with German activities resulting in a number of 9 firn cores drilled within two seasons (1981/82 and 1986/87) at locations near the Georg-von-Neumayer station on the Ekström Ice Shelf (Schlosser and others, 1999) and on Ritscherflya (Oerter and others, 1999). Glaciological work conducted in the frame of the Swedish Antarctic Research Program (SWEDARP) in the seasons 1988/89 (Isaksson and Karlén, 1994) and 1991/1992 (Isaksson and others, 1996; this paper) included a number of 11 shallow firn cores along a traverse route starting at the Riiser-Larsenisen Ice Shelf across Ritscherflya towards Amundsenisen east of the Heimefrontfjella mountains. The latter area was visited again during the Swedish ITASE campaigns in 1993/1994, providing accumulation data based on snow pits dated by multi-parameter chemical records (Stenberg and others, 1998). Collaborative Swedish/Norwegian/Dutch activities continued in 1997/98 within EPICA including snow pit studies (Stenberg and others, 1999) as well as medium depth ice-core drillings at Camp Victoria (Karlöf and others, 2000) and a depot of the British Antarctic Survey (BAS) (Hofstede and others, 2004). Within five consecutive seasons from 1995/96 until 99/2000 EPICA traverse work under the leadership of the German Alfred Wegener Institute (AWI) retrieved more than 30 shallow firn and 3 medium depth ice cores with the majority taken on Amundsenisen, but also close to Neumayer station, in the Heimefrontfjella, and on Ritscherflya (Oerter and others, 1999 and 2000; this paper).

Within an extensive mass balance and glacier research project the Fimbulisen and Jutulstraumen region was traversed by several Norwegian Antarctic Research Expeditions (NARE) in the seasons 1992/93 (Melvold and others, 1998; Melvold, 1999) and 1993/94. They recovered a number of 12 shallow firn cores. In 1996/97 a Norwegian/Swedish/Dutch ground traverse as part of EPICA drilled 15 firn-cores along a traverse from Fimbulisen passing Hellehallet and Mühlig-Hofmann-Gebirge and on the plateau along the ice divide leading to the Japanese deep drilling site at Valkyrjedomen (called Dome F). Those records define the eastern boundary of our investigation area (Isaksson and others, 1999; Van den Broeke and others, 1999). NARE field workers in collaboration with Dutch scientists also recovered two medium depth ice cores on Amundsenisen in 2000/01 (Hofstede and others, 2004) and on Fimbulisen (Kaczmarska and others, 2004). BAS expeditions retrieved 2 shallow firn cores in the season 1986/87 (Wolff and Suttie, 1994) and 1987/88 (Mulvaney and Wolff, 1993), the only records available in Coats Land, the south-western corner of the investigated area. Ten years later, in 1997/98, BAS in joint venture with NARE participated in EPICA studies with 3 shallow firn cores (this paper) and one medium depth ice core on Amundsenisen (Hofstede and others, 2004). The latest available record at the time of writing results from AWI firn core drilling near Heimefrontfjella in 2003/04 (this paper).

SPATIAL AND TEMPORAL VALIDITY OF DATA

Annual local noise and small-scale spatial variability

Spatial and temporal variations in accumulation are attributed to the combined effects of (1) airmass transport pathways, (2) interaction of airflow with topography, and (3) local effects, i.e. sastrugi and redistribution by snowdrift. Post-depositional processes driven by wind reshape the primary precipitation pattern leading to preferential accumulation of material in topographic depressions, in contradiction to the lowered accumulation rates that we find on crests (e.g. Sommer and others, 2000; Arnold and Rees, 2003; Frezzotti and others, 2005). Complex local wind erosion and re-deposition processes occur due to undulations in surface topography at the kilometre scale and more specifically on variations of the downslope surface gradient (e.g. Melvold and others, 1998). King and others (2004) observed large spatial variability in snow accumulation (20–30% on a scale of around 1 km) even for gentle topography, which was attributed to a highly nonlinear relationship between wind

speed and snow transport. Stake line readings and ice-penetrating radar (IPR) studies provide continuous accumulation information at high spatial resolution (Richardson-Näslund and others, 1997; Richardson-Näslund 2004; Spikes and others, 2004; Rotschky and others, 2004). For instance Isaksson and Karlén (1994) found a standard deviation of 70% of the average annual accumulation using stake measurements at Ritscherflya. Such results raised questions on how representative single point records are at a regional scale. Their spatial scale of significance has been widely discussed and is a critical point when interpolating over large distances.

Locally highly variable snow deposition patterns are preserved in the form of a considerable inter-annual variability generally detected in firn core stratigraphy. This phenomenon has been discussed in a large body of literature (e.g. Goodwin, 1991; Frezzotti and others 2004 and 2005). Specifications for year-to-year variations range from 30% on Amundsenisen (Sommer and others, 2000) to as high as 250% for firn cores drilled on Jutulstraumen (Melvold and others, 1998). High-frequency variability in annual layer thickness within ice cores are agreed to be associated in the first place with wind redistribution controlled by micro-relief, rather than to climatically forced precipitation changes (Frezzotti and others, 2005; Reijmer and Van den Broeke, 2003). As a consequence, accumulation time series generally miss a clear correspondence even for nearby firn core sites (Sommer and others, 2000). Such findings indicate that only multi-year accumulation averages should be used for regional studies. A number of 5-10 years is generally considered sufficient for providing reliable estimates of local snow accumulation (Petit and others, 1982; Mosley-Thompson and others, l985; Morgan, 1985). We account for this fact by excluding all records that cover less than 5 years of accumulation in order to avoid biases in our interpolation map resulting from annual local noise and small-scale spatial variability. When having a choice between several measurements taken at the same location, we decided for the one with the longer average time interval.

Multi-decadal accumulation trends

Both positive and negative long-term trends of snow accumulation have been reported over the Antarctic Ice Sheet, e.g. Petit and others (1982), Morgan and Goodwin (1991), Mosley-Thompson (1992). Our dataset consists of records that are irregularly sampled in space and time, covering a wide variety of accumulation time periods. Average time intervals range from several years to several hundreds of years with the majority (78 out of 111) less than 50 years. Sampling was carried out over a time period of roughly 40 years (see Appendix). Therefore, differences in accumulation values might partly originate from a changing accumulation rate over time. Consequently, those could induce misinterpretations when modelling spatial variations statistically in order to define optimal interpolation criteria for applying geostatistical surface prediction methods, i.e. kriging (see section Surface Prediction below). It must therefore first be investigated, whether this dataset is suitable for compiling an accumulation map.

All investigators involved in data sampling agree that time series of accumulation rates and stable isotopes do not indicate a drastic change in atmospheric moisture transport in DML over the covered time periods of their studies (e.g. Karlöf and others, 2000; Melvold, 1999; Isaksson and others, 1996; Oerter and others, 1999). At decadal time scales, the records show no clear trend or different magnitude and direction in changes between the single sites. Oerter and others (1999) and Graf and others (2002) observed temporal variations for the last two centuries in central DML that were linked to temperature variations derived from stable isotopes records. However, for the same region constant accumulation rates characterized the last 2,000 years in three intermediate depth ice cores (Sommer and others, 2000). Slight increases or decreases in accumulation rates over several decades were found to be small compared to interannual variability. This is in accordance with findings of Isaksson and others (1996) and Hofstede and others (2004) who combined information from different sites on Amundsenisen. We found a stable plateau climate by comparing cores M with M150 (see Appendix). Both were drilled at 75°00'S/15°00'E and cover a

time period of 31 years and 1033 years, respectively. Despite the different average-time intervals similar accumulation values of 43 and 45 kg m^{-2} a^{-1}, respectively, indicate stable accumulation rates for the longest time interval included in this study.

Coastal areas experience stronger climatic fluctuations since they are exposed to the combined effects of changing sea ice extent and cyclonic activity (Isaksson and Karlén, 1994; Kaczmarska and others, 2004). However, since observed changes (e.g. Isaksson and others, 1996; Melvold, 1999) are generally restricted in time, show alternating signs and no inter-site correlation, a likely explanation is the movement of a bore-hole site through a complex undulation pattern related to bedrock topography (Melvold and others, 1998; Sommer and others, 2000). Depending on ice-flow velocity and wavelength of surface undulations, which is of the order of some kilometres (Richardson-Näslund and others, 1997; Rotschky and others, 2004; Eisen and others, 2005), a coring site requires several decades to travel from a low accumulation surface crest to a high accumulation surface hollow. For this reason an apparent trend may be detected from changes in annual-layer thickness of firn cores, even in stable climatic periods. However, the average accumulation derived from the affected firn core would still be representative for a larger surrounding area. Based on these data, we assume that no major change in accumulation occurred in western DML during the past 1000 years that would significantly corrupt the quality of a spatially interpolated picture of accumulation rates over our area of interest.

EXPLORATORY SPATIAL DATA ANALYSIS

Nearly all 111 selected accumulation records result from traverse work conducted by different nations as described above. Therefore, data collection did not follow an optimal sampling procedure. The resulting sampling density varies and remains relatively small considering the well-known high spatial variability of snow accumulation, particularly in mountainous areas. In order to define suitable parameters for a spatial interpolation we first examined the statistical properties of our dataset, i.e. value distribution, spatial variability, and global spatial trends.

Value distribution

Accumulation records range from as low as 19 kg m^{-2} a^{-1} at the south-eastern corner of our study area on Amundenisen to a maximum of 491 kg m^{-2} a^{-1} on Jutulstraumen. By looking at the number of records measured within defined accumulation intervals in steps of 20 kg m^{-2} a^{-1}, we find our dataset not to be normally distributed (Fig. 2). A bell-shaped histogram would be required for an optimal interpolation result. Instead, the majority of records are lower than 200 kg m^{-2} a^{-1}, causing the histogram bars to be clearly shifted to the left. The highest number of records (36) fall into the accumulation interval between 45 and 65 kg m^{-2} a^{-1}, while medium and higher values are obviously underrepresented in our dataset. This skewness is also expressed by a large difference between the median (63.5 kg m^{-2} a^{-1}) and the mean value (129.49 kg m^{-2} a^{-1}), which in turn is of the same order as the standard deviation of 124.67 kg m^{-2} a^{-1}. The considerably higher proportion of low data values within the dataset is clearly due to the preferential sampling on the DML plateau area (75 out of 111 records). Data points with values higher than 200 kg m^{-2} a^{-1} are without exception located near the coast and the adjacent lower inland regions north of the nunataks, while nearly all records below this threshold belong to the inland plateau. Already from this frequency distribution two separate accumulation regimes can be

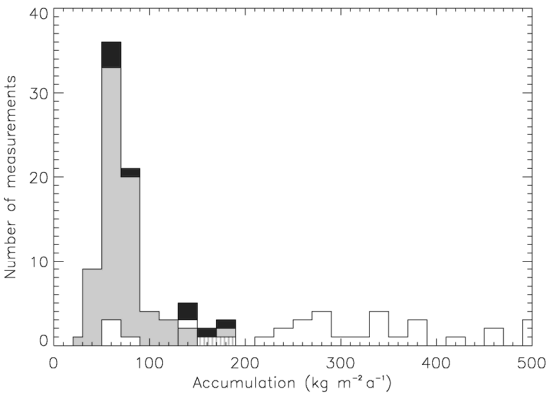

Figure 2. Frequency distribution of accumulation rates. In grey: records sampled on the plateau (generally below 200 kg m^{-2} a^{-1}), white: coastal records, and in black: total number.

distinguished.

By looking at the accumulation values separately for coastal and plateau regions, we find a distribution close to normal for the coast, expressed by similar mean and median values (Table 1). The coastal records account for the high standard deviation in our dataset, with a value of 128.2 compared to only 30.0 kg m^{-2} a^{-1} for the plateau. The latter is in agreement with findings of Oerter and others (1999). The higher spread in accumulation values for the coastal data is not surprising, considering the complex geographical nature described earlier. However, the relative standard deviation is similar for both regions. For the subset of records located on the plateau a distribution close to normal can be achieved by performing a logarithmic transformation of our data values. By this we can adjust the coefficient of skewness, a measure of the symmetry of a distribution, which should be near zero for optimal interpolation results.

For individual regions within the area of investigation we find distinct differences in accumulation mean and spread (Fig. 3). We are aware that the number of records is a critical factor for such comparisons, particularly for the nunatak areas. Amundsenisen and Wegenerisen exhibit their smooth topography and remote location with low spread and values generally lower than 120 kg m^{-2} a^{-1}. In contrast, the data are highly variable for coastal regions. The most striking region is Jutulstraumen, which covers the entire range of accumulation values within our dataset. This large spatial variation in accumulation has been attributed to strong erosion and re-deposition processes on the ice stream controlled by surface undulations and a

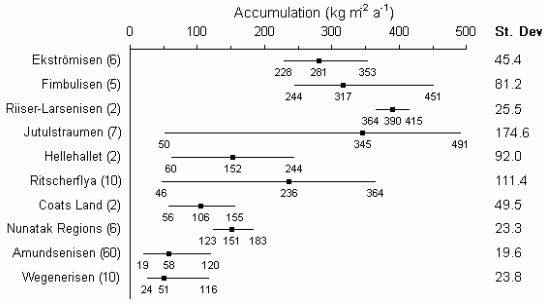

Figure 3. Minima, mean, and maxima of accumulation rates for individual regions. The number of respective records is given in brackets.

Table 1. Statistics of accumulation-value distribution in kg m^{-2} a^{-1}.

	Total	*Coast*	*Plateau*	*Plateau Log. Transf.*
No. records	111	36	75	75
Mean	130	271	62	4.04
Median	64	271	56	4.03
Min	19	46	19	2.94
Max	491	491	171	5.14
Std. dev.	124.2	128.2	30.0	0.42
Skewness	1.46	-0.06	1.86	0.37

complex near surface wind field (Holmlund and Näslund, 1994). Accumulation extremes also result from increased precipitation between 900 and 1200 m elevation due to orographic uplift and adiabatic cooling of humid air masses (Melvold and others, 1998).

Outliers

Outliers within a dataset can dramatically affect the performance of a surface prediction by distorting the variogram modelling associated with the kriging procedure later used for the interpolation. They should therefore be identified prior to the interpolation (Burrough, 1986). Within our dataset no global outliers exist, i.e. no records are very high or low relative to all of the values. However, on four locations we find sample points within the normal range of the entire dataset, but exhibiting unusually low values relative to their surrounding neighbours. Major accumulation deficits are found for core sites Jut_E (72°13'S, 00°43'W) and Jut_I (71°31'S, 01°11'W), both located on Jutulstraumen, which have been linked to strong katabatic wind activity as indicated by wind crusts, sastrugi and nearby blue ice fields (Melvold and others, 1998). Anomalous low values also characterize core sites B10_11 (72°30'S, 09°06'W) and “km 270” (72°56'S, 09°41'W), situated on Ritscherflya at an elevation of around 1000 m a.s.l.. From field observations and isotope analysis it was found that these low values are also due to erosion by wind activity, not caused by lower precipitation rates (Oerter and others, 1999). From stake line readings (Rotschky and others, 2006) and IPR measurements (Richardson-Näslund and others, 1997) we

know that those core sites are situated within a wider zone of very low accumulation rates, which is likely a consequence of strong katabatic winds originating in the Heimefrontfjella range. We can therefore conclude that all those local outliers have been measured correctly and represent real abnormalities, reflecting the high spatial accumulation variability in complex terrain. We expect that measuring errors are not a major problem for an interpolation of the dataset.

Global spatial trends

To identify global spatial trends we examined possible relationships between snow accumulation and distance to the nearest coast, elevation as well as slope gradient and orientation. Those variables are often used to explain the general distribution of snow accumulation rates (e.g. Giovinetto and others, 1990; Bernhard and Weibel, 1999). Terrain information was extracted from the RAMP digital elevation model (Liu and others, 2001). The ice front was taken from the Antarctic Digital Database (ADD) version 4, provided by the Scientific Committee on Antarctic Research (SCAR). Using the entire dataset, we did not find a correlation between accumulation rates and the chosen parameters. For instance, both the lowest (46 kg m^{-2} a^{-1}) and highest (491 kg m^{-2} a^{-1}) coastal values are found within the elevation interval of 900 to 1100 m a.s.l. at a distance of 200 to 250 km from the coast. Even on the flat ice shelves, accumulation ranges from 228 to 451 kg m^{-2} a^{-1}. Clear cross-correlations between slope gradient and accumulation reported by Melvold and others (l998) or King and others (2004) apply only for limited areas.

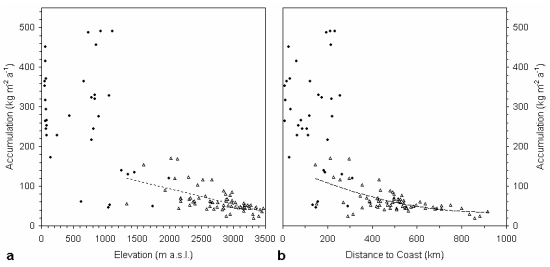

Figure 4. Global trends. Correlations between accumulation rates and (a) elevation as well as (b) distance to the coast. Coastal records are given as black dots, triangles indicate records sampled on plateau regions.

Table 2. Global trends. Correlation coefficients (R) between accumulation rates and elevation as well as distance to the coast.

Distance Interval (km)	*No. records*	*R*	*Elevation Interval (m a.s.l.)*	*No. records*	*R*
150 - 1000	75	-0.60	1300 - 3500	75	-0.60
400 - 1000	58	-0.61	2000 - 3500	72	-0.57
500 - 1000	37	-0.68	2500 - 3500	55	-0.52
600 - 1000	17	-0.80	3000 - 3500	26	-0.51

Excluding all coastal records from the analysis yields an expected negative cross-correlation between accumulation and elevation as well as distance to the nearest coast each with R = -0.6. As in Giovinetto and others (1990) we can describe those relations using first and second order regression functions (Fig. 4). Concerning continentality, the correlation improves when moving gradually away from the coast (Table 2). The best correlation of R = -0.8 we find for the distance interval of 700 to 1000 km from the coast, indicating that other reasons for spatial accumulation variations (e.g. surface undulations) become less important inland.

SURFACE PREDICTION

Semi-variogram modelling

The process of variogram modelling, i.e. variography, is an instrument for characterizing the spatial variability of a dataset. It gives useful information for selecting optimal interpolation parameters, e.g. the mathematical model to be used for computing efficient interpolation weights, the size and shape of the search window, as well as the number of neighbouring measurement sites to be included in the prediction of unsampled sites. In order to estimate accumulation rates for the western DML region we use kriging as geostatistical interpolation method. Fundamental to kriging is the assumption that a relationship exists between the location of sites and the measured values, which can be modelled statistically. In theory the difference of values should be the same between any two points that are the same distance and direction apart. Naturally, dissimilarities between records increase with distance since nearby samples tend to be more alike than those farther apart. The degree of

spatial autocorrelation is estimated from the data based on a scatter plot of half of the squared difference between pairs of sample values against their spatial separation *h*, called the semi-variogram cloud. An average of dissimilarities *y*(h)* is calculated for all sample pairs falling into a certain distance bin of defined size, i.e. the lag size. The theory concerning kriging is discussed in more detail by Burrough (1986) and Wackernagel (1998).

Interpolation settings

Following the exploratory spatial data analysis, the dataset was separated into coastal and inland sites in order to define a set of domain-specific interpolation criteria. Different statistical properties suggest to use two local rather than a single global model for an interpolation, even though for the coastal domain the number of records becomes a critical factor for achieving a stable semi-variogram. The Heimefrontfjella, Kirwanveggen, and Mühlig-Hofmann-Gebirge mark the borderline between both data subsets. To improve the western boundary conditions, where data are missing over large distances we used data from Coats Land for both domains.

The selection of a proper set of interpolation parameters is highly subjective. However, we found that the resulting patterns remained quite stable for reasonable values of tested interpolation parameters. Even the specific variogram model type, used for computing interpolation weights, seems to be of minor influence. Over the smooth plateau region, where accumulation variability is relatively small, we selected a spherical model type which shows a progressive decrease of spatial autocorrelation until some distance, beyond which the autocorrelation becomes zero. For the coastal domain, a circular model type with a steeper curve near the origin, giving more weight to the closest neighbours for each prediction, is more appropriate. Variations in lag size and number did not significantly affect the output surface. A lag size of 20 km was chosen for both domains in order to get representative averages for semi-variogram bins.

Concerning the number of measured values to be used in a prediction, stable results are computed including at least 2 to 5 neighbours in all four directions. Any further increase in the number of neighbours has no impact on the resulting pattern because of the decreasing influence of remote points. The specific shape of the neighbourhood determines where to look for data points. A clear indication for selecting optimal search radii is given by the range of the semi-variogram cloud defining the distance to which data are statistically correlated (Burrough, 1986). Higher autocorrelation in one direction than in another might result from global trends and/or anisotropy. Our earlier spatial data analysis showed a first order trend on the plateau running from northwest to southeast towards increasing elevation and distance to coast, which was removed prior to variogram modelling and added back before predictions were made. From variography we still find anisotropic autocorrelation for this region, i.e. values in northeast-southwest direction change more slowly than perpendicular to this. Since such a phenomenon can be explained from topography and resultant predominant wind direction as modelled e.g. by Van Lipzig and others (2004), we assume that these directional differences are not a measurement artefact resulting from the preferential alignment of records along traverse lines which could lead to insufficient sampling density for robust estimates in all directions. Consequently we accounted for this anisotropic spatial autocorrelation by applying varying search radii as described in the following.

In general we found a single plateau record to be representative for a larger area

Table 3. Interpolation settings.

Settings	*Coastal domain*	*Plateau domain (Interior region)*
Geostatistical method	Ordinary kriging	Universal kriging
Transformation	none	Log
Trend	none	linear
Model type	spherical	circular
Lag Size (m)	20,000	
Lag No.	15	
Neighbours	5 at least 2 per search quarter	
Search window		
Anisotropy	No	Yes (NW -SE)
Axis angle	45°	65°
Major axis (km)	80 - 125	205 - 250
Minor axis (km)	80 - 125	105 - 150

than coastal records. This is in agreement with other findings (Stenberg and others, 1999). The spatial autocorrelations suggests that the search radii should be between 200 and 250 km from northeast to southwest and 100 to 150 km perpendicular to this direction. For the coastal domain, where major variation occurs over shorter distances, the search radius was kept as small as possible (between 80 to 125 km in any direction). Little variations in search radii led to evident changes in the predicted surface, particularly in the coastal area. Since the most efficient search radius remains subject of speculation, a good solution is to produce an average composite of 10 realisations, each time adjusting the search window by slightly enlarging its two axes (i.e. the search radii) in 5 km steps. The differences between these predictions are used as a measure of uncertainty in the predicted surface.

Having computed the experimental variograms and fitted model parameters, our accumulation records were interpolated using ordinary kriging for the coast and universal kriging for the plateau domain. The latter should be applied only if an apparent spatial trend in the data can be explained from a priori knowledge (Burrough, 1986). Using a logarithmic transformation makes the data more normally distributed in case of the plateau domain. Here, the interpolation was carried out using the logarithmically transformed data which were then transformed back. In Table 3 our interpolation settings are summarized.

RESULTS AND DISCUSSION

Surface Prediction

The resulting accumulation distribution is mapped in Figure 5. Clearly, predicting a surface from sparse point data gives only a smoothed picture of the underlying reality. Details of spatial accumulation variability cannot be reproduced and the resulting pattern is highly dependent on the random distribution of sample points. For the coastal area, high accumulation alternates with accumulation lows reflecting a spatial

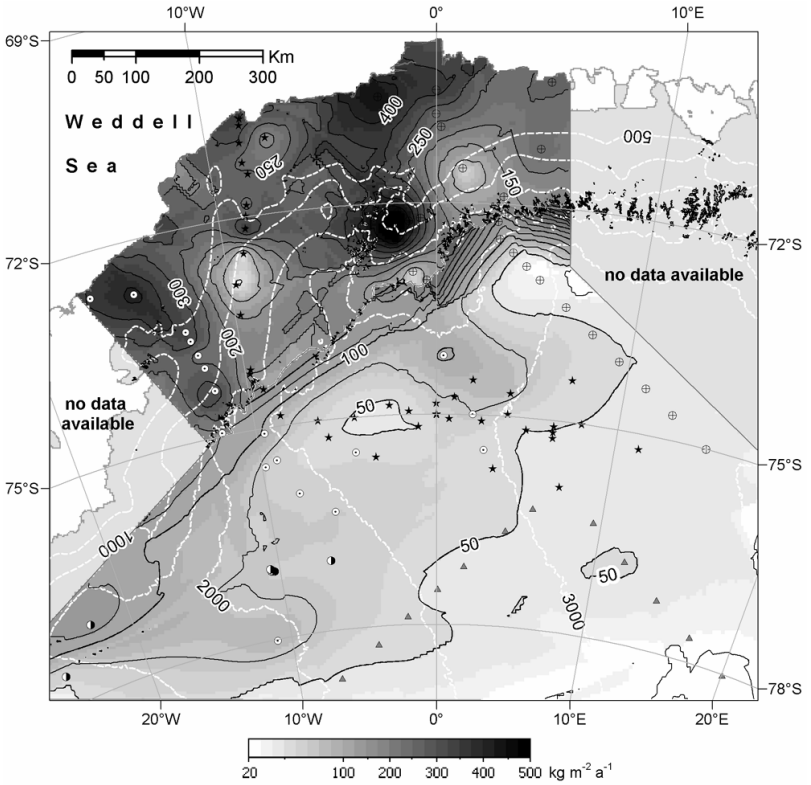

Figure 5. Contoured accumulation pattern for western DML (data available from the PANGEA Web site 33Hhttp://doi.pangaea.de/10.1594/PANGAEA.472297). A grey scale as well as contours at 50 kg m^{-2} a^{-1} (coastal domain) and 25 kg m^{-2} a^{-1} (plateau domain) are used to indicate the broad spatial variability in snow accumulation across the predicted area. Elevation contours in 500 m intervals are given as dashed white lines. The borderline between coastal and plateau domain follows the mountain chains and is shown as solid grey line.

variability in precipitation and snow transport that is topographically forced. Isolated circular patterns around single records result from values that deviate significantly from their surrounding neighbours. On the plateau, a clear trend of decreasing accumulation with increasing distance to coast and elevation from northwest to southeast (as described above) is reproduced. Values range from 150 kg m^{-2} a^{-1} just south of the mountain ridges down to as little as 25 kg m^{-2} a^{-1} near the south-eastern corner of our study area. Tongue-shaped patterns of higher accumulation advance from coastal regions further inland, where nunatak barriers are absent over larger distances, for instance south of Jutulstraumen and Coats Land. Some problems are visible near Mühlig-Hofmann-Gebirge where predicted values at the northern margin of the plateau domain increase rapidly over short distances. In this area computed accumulation rates are unreliable. Interpolation difficulties occur furthermore where in situ data are missing over large distances between traverse lines running inland from the coast. The resulting striped patterns are clearly an artefact of the interpolator and not representative for the true accumulation.

Due to interpolation uncertainties in consequence of the sparse and uneven data sampling scheme, estimating the total surface mass balance in western DML is difficult. In spite of the larger area, the total accumulation on the plateau ($58 \cdot 10^4$ km²) sums up to only 38 Gt a^{-1} versus 62 Gt a^{-1} for the coastal region with a spatial extent of $24 \cdot 10^4$ km². Discrepancies in total accumulation between our 10 slightly varied realisations are marginal (generally less than 1%). In Table 4 we compare our results with previous accumulation compilations by Vaughan and others (1999) and by Arthern and others (2006), who both guided the interpolation using background fields of satellite microwave observations, as well as by Huybrechts and others (2000), who applied a spline interpolation to nearly the same input data as in the present study. While the results of Vaughan and others (1999) and Huybrechts and others (2000) are 18% and 16% larger, respectively, the recently published findings by Arthern and others (2006) yield about 13% less accumulation for the western DML area than this study. These differences result from

Table 4. Total accumulation in Western DML in Gt a^{-1}. Comparison between this study and earlier published results.

	Coastal domain	*Plateau domain*	*Total*	*Difference %*
this paper	62.0	37.7	99.7	-
Vaughan and others, 1999	63.4	54.5	117.9	+18.3
Huybrechts and others, 2000	74.5	41.3	115.8	+16.2
Arthern and others, 2006	49.1	37.4	86.5	-13.3

significantly higher estimates for the plateau in case of Vaughan and others (1999) and for the coastal area in case of Huybrechts and others (2000). In opposite, Arthern and others (2006) yield similar estimates for the plateau, their coastal estimates however are significantly lower than ours. Mainly the same input data have been used in all of the studies, which suggests that differences occur due to interpolation approaches. In general, spline interpolation may produce local artefacts of excessively high or low values if input values change dramatically over short distances. Therefore, the results of Huybrechts and others (2000) are unreliable for the DML coastal area. The main reason for disagreements we see in the absence of a barrier between the coastal and plateau accumulation regimes in earlier studies, which results in an overestimation of the area of validity of high accumulation coastal records in case of Vaughan and others (1999) and of low accumulation plateau records in case of Arthern and others (2006), respectively. Like those of Arthern and others (2006) our results indicate that snow accumulation in western DML is very probably smaller than previously assumed.

Interpolation accuracy

In general, accuracies vary across the predicted area with data sampling density. To evaluate the uncertainty of the interpolated surface, an error estimate is required. In absence of an extra set of independent

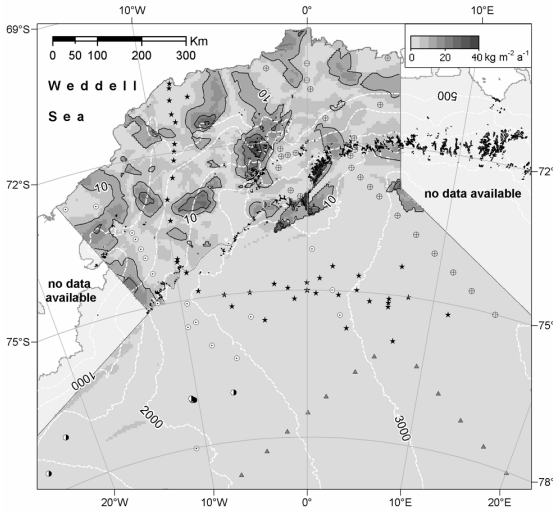

Figure 6. Map of standard deviation between 10 predictions with stepwise increase of search radii. The data are available from the PANGEA Web site 34Hhttp://doi.pangaea.de/10.1594/PANGAEA.472298. A grey scale and contours at 10 kg m^{-2} a^{-1} (black lines) indicate the interpolation inaccuracy. Elevation contours in 500 m intervals are given as dashed white lines. The borderline between coastal and plateau domain follows the mountain chains and is shown as solid grey line.

observations randomly distributed across the predicted area, we cannot quantify the accuracy directly. From the relatively small number of available data, a subset for validation purposes could not be created prior to interpolation. Each point in the dataset is essential for the variogram modelling and original prediction.

Some measure of certainty is provided as a by-product of the kriging procedure, known as the kriging variance. In the literature, this quantity has been criticised specifically as being ineffective and found to be a poor substitute for a true error (e.g. Journel, 1986; Chainey and Stuart, 1998). Basically, the kriging variance, depending only on the geometrical arrangement of the sample data points, simply states that accuracy decreases with growing distance from input data.

As a measure of confidence we instead used the differences between the 10 interpolation realisations, each with slight adjustments in the applied search window as described above. The lower the standard deviation of the different predictions, the more accurate the interpolation is likely to be in terms of self-consistency of the model applied to the data. The standard deviations across the predicted area are mapped in Figure 6, expressing a clear difference between coastal and plateau domains. On the plateau, data density seems sufficient for achieving stable interpolation results, with the exception of the Jutulstraumen inlet area. In contrast, for coastal regions, exhibiting a much larger spatial accumulation variation, major interpolation uncertainties occur for unsampled locations between measurement sites. Clearly, small adjustments in the shape of the search window impact mostly were single values deviate greatly from their surrounding neighbours (local singularities as described above). This result is leading back to the question, how representative single point records are for their wider surrounding. In order to catch the full range of accumulation variability occurring due to the complex coastal terrain and wind field conditions, further data acquisition should be carried out also in other directions than from north to south. Regional climate modelling may also help in this respect (Van den Broeke and others, 2006).

SUMMARY AND CONCLUSIONS

A set of 111 accumulation measurements from western DML is compiled and presented. Most data result from field work carried out over the last 15 years in the frame of EPICA and ITASE. Older records from literature are used to supplement the data. In spite of a large variety of covered accumulation periods, ranging between 5 and 1000 years, we find the datasets temporally representative as no significant trend in accumulation history over the last centuries has been reported from ice core records of this region. Uneven data distribution resulting from preferential alignment of measurement sites along traverse lines, which lead mostly inland from the coast, is a more critical factor for judging the spatial accumulation variability. Nevertheless, an interpolated map of mean annual snow accumulation rate could be derived that is in accordance with presumptions made from known overall spatial trends and topographically forced changes in accumulation. The interpolation was carried out using the geostatistical interpolation method of kriging, based on two local models and domain specific interpolation settings for coastal and inland

sites. Our results suggest that the total accumulation rate for the predicted area is about 16% to 18% smaller than published in earlier years. For a quantitative evaluation of the uncertainty in predicted accumulation rates we calculated the standard deviation of 10 interpolation realisations each with slight stepwise increase in search radii. A map of the standard deviation thus obtained could help in locating future sampling sites to further minimize interpolation uncertainties. The existing sampling network should be improved with respect to surface topography and associated surface wind field patterns which in combination have the potential to change accumulation conditions dramatically over short distances, especially in the complex terrain of the coastal regions. These results are of interest for the interpretation of climate records from the study area as well as for ongoing surface-mass balance modelling, aiming at resolving the fine scale accumulation pattern across western DML.

ACKNOWLEDGEMENTS

This work is a contribution to the 'European Project for Ice Coring in Antarctica' (EPICA), a joint European Science Foundation (ESF))/European Commission (EC) scientific programme, funded by the EC and by national contributions from Belgium, Denmark, France, Germany, Italy, the Netherlands, Norway, Sweden, Switzerland and the United Kingdom. This is EPICA publication No. xx. The authors thank editor R. Bindschadler and two anonymous reviewers for valuable comments on the manuscript. Reprinted from the Journal of Glaciology with permission of the International Glaciological Society.

REFERENCES

Arnold, N. and G. Rees. 2003. Self-similarity in glacier surface characteristics. *J. Glaciol.*, **49**(167), 547-554.

Arthern, R. J., D. P. Winebrenner and D. G. Vaughan (2006), Antarctic snow accumulation mapped using polarization of 4.3-cm wavelength microwave emission. *J. Geophys. Res.*, **111**, D06107, doi:10.1029/2004JD005667.

Bernhard, L. and R. Weibel. 1999. Modelling snowmelt using a digital terrain model and GIS-based techniques. *In* R. Dikau and H. Sauer, *eds*. *GIS for earth surface systems. Analysis and modelling of the natural environment.* Gebrüder Borntraeger, Berlin.

Budd, W. F. and D. B. Carter. 1971. An analysis of the relation between the surface and bedrock profiles of ice caps. *J. Glaciol.,* **10**(59), 197-209.

Burrough, P.A. 1986. Principles of Geographical Information Systems for Land Resources Assessment. New York, Oxford University Press.

Chainey, S., N. Stuart. 1998. Stochastic simulation: an alternative interpolation technique for digital geographic information. In Carver, S., *ed., Innovations in GIS 5*. London, UK, Taylor & Francis Ltd.

Eisen, O., W. Rack, U. Nixdorf and F. Wilhelms. 2005. Characteristics of accumulation around the EPICA deep-drilling site in Dronning Maud Land, Antarctica. *Ann. Glaciol.*, **41**, 41-46.

Frezzotti, M., M. Pourchet, O. Flora, S. Gandolfi, M. Gay, S. Urbini, C. Vincent, S. Becagli, R. Gragnani, M. Proposito, M. Severi, R. Traversi, R. Udisti and M. Fily. 2004. New estimations of precipitation and surface sublimation in East Antarctica from snow accumulation measurements. *Climate Dyn.*, **23**, 803–813.

Frezzotti, M., M. Pourchet, O. Flora, S. Gandolfi, M. Gay, S. Urbini, C. Vincent, S. Becagli, R. Gragnani, M. Proposito, M. Severi, R. Traversi, R. Udisti and M. Fily. 2005. Spatial and temporal variability of snow accumulation in East Antarctica from traverse data. *J. Glaciol.*, **51**(172), 113-124.

Giovinetto, M.B. and C.R. Bentley. 1985. Surface balance in ice drainage systems of Antarctica. *Antarct. J. U. S.*, **20**, 6 –13.

Giovinetto, M.B., N.M. Waters and C.R. Bentley. 1990. Dependence of Antarctic surface mass balance on Temperature, Elevation, and Distance to open ocean. J. Geophys. Res., **95**(D4), 3517-3531.

Giovinetto, M.B. and H.J. Zwally. 2000. Spatial distribution of net surface accumulation on the Antarctic ice sheet. *Ann. Glaciol.*, **31**, 171-178.

Goodwin, I.D. 1991. Snow-accumulation variability from seasonal surface observations and firn-core stratigraphy, eastern Wilkes Land, Antarctica. *J. Glaciol.*, **37**(127), 383-387.

Graf, W., H. Oerter, O. Reinwarth, W. Stichler, F. Wilhelms, H. Miller and R. Mulvaney. 2002. Stable-isotope records from Dronning Maud Land, Antarctica. *Ann. Glaciol.*, **35**, 195-201.

Hofstede, M., R.S.W. Van deWal, K.A. Kaspers, M.R. Van den Broeke, L. Karlöf, J.-G. Winther, E. Isaksson, G. Lappegard, R. Mulvaney, H. Oerter and F.Wilhelms. 2004. Firn accumulation records for the past 1000 years on the basis of dielectric profiling of six cores from Dronning Maud Land, Antarctica. J. Glaciol., 50(169), 279-291.

Holmlund, P. and J.-O. Näslund. 1994. The glacially sculptured landscape in Dronning Maud Land, Antartica, formed by wet-based mountain glaciation and not by the present ice sheet. *Boreas* **23**, 139-148.

Huybrechts, P., D. Steinhage, F. Wilhelms and J. Bamber. 2000. Balance velocities and measured properties of the Antarctic ice sheet from a new compilation of gridded data for modelling. *Ann. Glaciol.*, **30**, 52-60.

Isaksson, E. and W. Karlén. 1994. Spatial and temporal patterns in snow accumulation and oxygen isotopes, Western Dronning Maud Land, Antarctica. *J. Glaciol.*, **40**(135), 399-409.

Isaksson, E., W. Karlén, N. Gundestrup, P. Mayewski, S. Whitlow and M. Twickler. 1996. A century of accumulation and temperature changes in Dronning Maud Land, Antarctica. *J. Geophys. Res.*, **101**(D3), 7085-7094.

Isaksson, E., M.R. Van den Broeke, J.-G. Winther, L. Karlöf, J.F. Pinglot and N. Gundestrup. 1999. Accumulation and proxy-temperature variability in Dronning Maud Land, Antarctica, determined from shallow firn cores. *Ann. Glaciol.*, **29**, 17-22.

Journel, A.G. 1986. Geostatistics: Models and tools for the earth sciences. *J. of the International Association for Mathematical Geology*, **18**(1), 119-140.

Karlöf, L., J.-G. Winther, E. Isaksson, J. Kohler, J.F. Pinglot, F. Wilhelms, M. Hansson, P. Holmlund, M. Nyman, R. Pettersson and M. Stenberg. 2000. A 1500 years record of accumulation at Amundsenisen western Dronning Maud Land, Antarctica, derived from electrical and radioactive measurements on a 120 m ice core. *J. Geophys. Res.*, **105**(D10), 12,471-12,483.

Kaczmarska, M., Karlöf, L., Isaksson, E., Winther, J-G., Godtliebsen, F., Hofstede, C.M., Van den Broeke, M.R., Van de Wal, R.S.W. & Gundestrup, N. 2004. Accumulation variability derived from an ice core from coastal Dronning Maud Land, Antarctica. *Ann. Glaciol.*, **39**, 339-345.

King, J.C., P.S. Anderson, D.G. Vaughan, G.W. Mann, S.D. Mobbs and S.B. Vosper. 2004. Wind-borne redistribution of snow across an Antarctic ice rise. *J. Geophys. Res.*, **109**(D11104), doi:10.1029/2003JD004361.

Liu, H., K. Jezek, B. Li and Z. Zhao. 2001. Radarsat Antarctic Mapping Project digital elevation model version 2. Digital media, National Snow and Ice Data Center, Boulder, CO, USA.

Lunde, T. 1961. On the snow accumulation in Dronning Maud Land. *Nor. Polarinst. Skr.* 123.

Melvold, K., J.O. Hagen, J.F. Pinglot and N. Gundestrup. 1998. Large spatial variation in accumulation rate in Jutulstraumen ice stream, Dronning Maud Land, Antarctica. *Ann. Glaciol.*, **27**, 231-238.

Melvold, K. 1999. Impact of recent climate on glacier mass balance: studies on Kongsvegen, Svalbard, and Jutulstraumen, Antarctica. (D.Sc. thesis, University of Oslo.) (Department of Geography Report 13.)

Morgan, V.I. 1985. An oxygen isotope – climate record from the Law Dome, Antarctica. *Clim. Change*, **7**, 415-426.

Morgan, V.I., I.D. Goodwin, D.M. Etheridge and C.W. Wookey. 1991. Evidence from Antarctic ice cores for recent increases in snow accumulation. *Nature,* **354**(6348), 58-60.

Mosley-Thompson, E., P. D. Kruss, L. G. Thompson, M. Pourchet and P. Grootes. 1985. Snow stratigraphic record at South Pole: potential for paleoclimatic reconstruction. *Ann. Glaciol.,* **7**, 2633.

Mosley-Thompson, E. 1992. Paleoenvironmental conditions in Antarctica since A.D. 15000: Ice core evidence. *In* R.S. Bradley and P.D. Jones, *eds. Climate since A.D. 1500*. Routledge, New York.

Mulvaney, R. and E. Wolff. 1993. Evidence for winter spring denitrification of the stratosphere in the nitrate record of Antartic firn cores. *J. Geophys. Res.*, **98**(D3), 5213-5220.

Noone, D., J. Turner and R. Mulvaney. 1999. Atmospheric signals and characteristics of accumulation in Dronning Maud Land, Antarctica. *J. Geophys. Res.*, **104**(D16), 19,191-19,211.

Oerter, H., W. Graf, F. Wilhelms, A. Minikin and H. Miller. 1999. Accumulation studies on Amundsenisen, Dronning Maud Land, Antartica, by means of tritium, dielectric profiling and stable-isotope measurements: first results from the 1995-97 field seasons. *Ann. Glaciol.*, **29**, 1-9.

Oerter, H., F. Wilhelms, F. Jung-Rothenhäusler, F. Göktas, H. Miller, W. Graf and S. Sommer. 2000. Accumulation rates in Dronning Maud Land, Antartica, as revealed by dielectric-profiling measurements of shallow firn cores. *Ann. Glaciol.*, **30**, 27-34.

Petit, J.R., J. Jouzel, M. Pourchet and L. Merlivat. 1982. A detailed study of snow accumulation and stable isotope content in Dome C (Antarctica), *J. Geophys. Res.,* **87**(C6), 4301-4308.

Picciotto, E., G. Grozaz and W. De Breuck. 1971. Accumulation on the South Pole-Queen Maud Land Traverse, 1964-1968. Antarctic Snow and Ice Studies II, *Antarc. Res. Ser.*, **16**, 257-315.

Reijmer, C. and M.R. Van den Broeke. 2003. Temporal and spatial variability of the surface mass balance in Dronning Maud Land, Antarctica, as derived from automatic weather stations. *J. Glaciol.*, **49**(167), 512-520.

Richardson, C. and P. Holmlund. 1999. Spatial variability at shallow snow-layer depths in central Dronning Maud Land, East Antarctica. *Ann. Glaciol.*, **29**, 10-16.

Richardson-Näslund, C., E. Aarholt, S.-E. Hamram, P. Holmlund and E. Isaksson. 1997. Spatial distribution of snow in western Dronning Maud Land, East Antarctica, mapped by a ground-based snow radar. *J. Geophys. Res.*, **102**(B9), 20,343-20,353.

Richardson-Näslund, C. 2004. Spatial characteristics of snow accumulation in Dronning Maud Land, Antarctica. *Global and Planetary Change*, **42**, 31-43.

Rotschky, G., O. Eisen, F. Wilhelms, U. Nixdorf and H. Oerter. 2004. Spatial distribution of surface mass balance on Amundsenisen plateau, Antarctica, derived from ice-penetrating radar studies. *Ann. Glaciol*., 39, 265-270.

Rotschky, G., W. Rack. W. Dierking, H. Oerter. 2006. Retrieving snowpack properties and accumulation estimates from a combination of SAR and scatterometer measurements. *IEEE Trans. Geosci. Remote Sens.*, **44**(4), 943-956.

Schlosser, E., H. Oerter and W. Graf. 1999. Surface mass balance investigations on Ekströmisen, Antarctica,1980-1996. Ber. Polarforsch. / *Rep. Pol. Res.*, 313.

Sommer, S., C. Appenzeller, C., R. Röthlisberger, M.A. Hutterli, B. Stauffer, D. Wagenbach, H. Oerter, F. Wilhelms, H. Miller and R. Mulvaney. 2000. Glacio-chemical study spanning the past 2 kyr on three ice cores from Dronning Maud Land, Antarctica. 1. Annually resolved accumulation rates. *J. Geophys. Res.*, **105**(D24), 29,411-29,421.

Spikes, V.B., G.S. Hamilton, S.A. Arcone, S. Kaspari and P. Mayewski. 2004. Variability in accumulation rates from GPR profiling on the West Antarctic plateau. *Ann. Glaciol.*, **39**, 238-244.

Stenberg, M., E. Isaksson, M. Hansson, W. Karlén, P.A. Mayewski, M.S. Twickler, S.I. Whitlow, and N. Gundestrup. 1998. Spatial variability of snow chemistry in western Dronning Maud Land, Antartica. *Ann. Glaciol.*, **27**, 378-384.

Stenberg, M., M. Hansson, P. Holmlund and L. Karlöf. 1999. Variability in snow layering and snow chemistry in the vicinity of two drill sites in western Dronning Maud Land, Antarctica. *Ann. Glaciol.*, **29**, 33-37.

Van den Broeke, M.R., J.-G. Winther, E. Isaksson, J.F. Pinglot, L. Karlöf, T. Eiken and L. Conrads. 1999. Climate variables along a traverse line in Dronning Maud Land, East Antarctica. *J. Glaciol.*, **45**(150), 295-302.

Van den Broeke, M. R., W. J. van de Berg and E. van Meijgaard. 2006. Snowfall in coastal West Antarctica much greater than previously assumed, *Geophys. Res. Lett.,* **33**, L02505, doi:10.1029/2005GL025239.

Van Lipzig, N.P.M., J. Turner, S.R. Colwell and M.R. Van den Broeke. 2004. The near-surface wind field over the Antarctic continent. *Int. J. Climatol.*, **24**, 1973-1982.

Vaughan, D.G., J. L. Bamber, M. B. Giovinetto, J. Russell and A. P.R. Cooper. 1999. Reassessment of net surface mass balance in Antarctica. *J. Climate*, **12**(4), 933-946.

Wackernagel, H. 1998. Multivariate geostatistics: an introduction with applications. Berlin, Springer.

Wolff, E. and E. Suttie. 1994. Antarctic snow record of southern-hemisphere lead pollution. *Geophys. Res. Let.*, **21**(9), 781 – 784.

APPENDIX

List of firn/ice core (C) and snow pit (P) measurements sampled over the area of interest (also available from the PANGEA Web site http://doi.pangaea.de/10.1594/PANGAEA.407654). Records included (i) in the interpolation are marked with a "y" in the first row.

	Site name		Institution / Campaign	Year drilled	Lat	Lon	Period	A kg $m^{-2}a^{-1}$	Dating Method	Reference
y	SPQML_01	P	SPQMLT 03	1967/68	79°08'S	36°43'E	1955-1968	35	total β	Picciotto a. oth. 1971
y	SPQML_02	P	SPQMLT 03	1967/68	78°51'S	33°14'E	1955-1968	37	total β	Picciotto a. oth. 1971
y	SPQML_03	P	SPQMLT 03	1967/68	78°43'S	29°43'E	1955-1968	35	total β	Picciotto a. oth. 1971
y	SPQML_04	P	SPQMLT 03	1967/68	78°35'S	27°05'E	1955-1968	36	total β	Picciotto a. oth. 1971
y	SPQML_05	P	SPQMLT 03	1967/68	78°19'S	23°22'E	1955-1968	25	total β	Picciotto a. oth. 1971
y	SPQML_06	P	SPQMLT 03	1967/68	78°01'S	20°05'E	1955-1968	19	total β	Picciotto a. oth. 1971
y	SPQML_07	P	SPQMLT 03	1967/68	77°39'S	17°10'E	1955-1968	29	total β	Picciotto a. oth. 1971
y	SPQML_08	P	SPQMLT 03	1967/68	77°16'S	14°25'E	1955-1968	45	total β	Picciotto a. oth. 1971
y	SPQML_09	P	SPQMLT 03	1967/68	76°50'S	11°53'E	1955-1968	52	total β	Picciotto a. oth. 1971
y	SPQML_10	P	SPQMLT 03	1967/68	76°22'S	09°32'E	1955-1968	45	total β	Picciotto a. oth. 1971
	SPQML_11	P	SPQMLT 03	1967/68	75°56'S	07°13'E	1955-1968	51	total β	Picciotto a. oth. 1971
y	SPQML_12	P	SPQMLT 03	1967/68	76°17'S	05°48'E	1955-1968	47	total β	Picciotto a. oth. 1971
y	SPQML_13	P	SPQMLT 03	1967/68	76°38'S	04°16'E	1955-1968	51	total β	Picciotto a. oth. 1971
y	SPQML_14	P	SPQMLT 03	1967/68	77°10'S	01°46'E	1955-1968	43	total β	Picciotto a. oth. 1971
y	SPQML_15	P	SPQMLT 03	1967/68	77°30'S	00°05'E	1955-1968	42	total β	Picciotto a. oth. 1971
y	SPQML_16	P	SPQMLT 03	1967/68	77°53'S	01°55'W	1955-1968	56	total β	Picciotto a. oth. 1971
y	SPQML_17	P	SPQMLT 03	1967/68	78°16'S	04°01'W	1955-1968	52	total β	Picciotto a. oth. 1971
y	SPQML_18	P	SPQMLT 03	1967/68	78°42'S	06°52'W	1955-1968	45	total β	Picciotto a. oth. 1971
y	B04	C	AWI	1981/82	70°37'S	8°22'W	1892-1981	353	$\delta^{18}O$, 3H	Schlosser a. oth. 1999
	FBKM002	C	AWI	1986/87	70°36'S	8°22'W	1972-1986	335	$\delta^{18}O$, ECM, 3H	this paper
y	FBKM40	C	AWI	1986/87	70°57'S	08°31'W	1971-1986	294	$\delta^{18}O$, ECM, 3H	Oerter a. oth. 1999
y	B12	C	AWI	1986/87	71°14'S	08°32'W	1961-1986	228	$\delta^{18}O$, ECM, 3H	Oerter a. oth. 1999
	FBKM70-W	C	AWI	1986/87	71°15'S	08°39'W	1979-1986	295	$\delta^{18}O$, ECM, 3H	this paper
y	FBKM90	C	AWI	1986/87	71°24'S	08°21'W	1969-1986	266	$\delta^{18}O$, ECM, 3H	Oerter a. oth. 1999
	SSKM125	P	AWI	1986/87	71°41'S	08°30'W	1982-1986	205	$\delta^{18}O$, ECM, 3H	Oerter a. oth. 1999
y	FBKM143	C	AWI	1986/87	71°50'S	08°37'W	1972-1986	229	$\delta^{18}O$, ECM, 3H	Oerter a. oth. 1999
y	FBKM160	C	AWI	1986/87	71°59'S	08°44'W	1969-1986	277	$\delta^{18}O$, ECM, 3H	Oerter a. oth. 1999
y	FBKM180	C	AWI	1986/87	72°10'S	08°50'W	1973-1986	364	$\delta^{18}O$, ECM, 3H	Oerter a. oth. 1999
y	B10, B11	C	AWI	1986/87	72°30'S	09°06'W	1970-1986	53	$\delta^{18}O$, ECM, 3H	Oerter a. oth. 1999
y	FBKM270	C	AWI	1986/87	72°56'S	09°41'W	1970-1986	46	$\delta^{18}O$, ECM, 3H	Oerter a. oth. 1999
y	BAS_CLA	C	BAS	1986/87	77°34'S	25°22'W	1964-1986	56	total β	Wolff a. Suttie 1994
y	BAS_H1	C	BAS	1987/88	77°02'S	22°32'W	1964-1987	155	nss, volc. horiz.	Mulvaney a. Wolff '93
y	SW89_A	C	SWEDARP	1988/89	72°39'S	16°39'W	1976-1988	364	$\delta^{18}O$	Isaksson a. Karlén '94
y	SW89_C	C	SWEDARP	1988/89	72°46'S	14°35'W	1976-1988	415	$\delta^{18}O$	Isaksson a. Karlén '94
y	SW89_D	C	SWEDARP	1988/89	73°27'S	12°33'W	1976-1988	330	$\delta^{18}O$	Isaksson a. Karlén '94
	SW89_E	C	SWEDARP	1988/89	73°36'S	12°26'W	1976-1988	311	$\delta^{18}O$	Isaksson a. Karlén '94
y	SW89_F	C	SWEDARP	1988/89	73°49'S	12°13'W	1976-1988	217	$\delta^{18}O$	Isaksson a. Karlén '94
y	SW89_G	C	SWEDARP	1988/89	74°01'S	12°01'W	1976-1988	276	$\delta^{18}O$	Isaksson a. Karlén '94
y	SW89_H	C	SWEDARP	1988/89	74°21'S	11°43'W	1976-1988	329	$\delta^{18}O$	Isaksson a. Karlén '94
y	SW89_J	C	SWEDARP	1988/89	75°05'S	09°32'W	1955-1988	104	total β	Isaksson a. Karlén '94
y	SW92_E	C	SWEDARP	1991/92	73°36'S	12°26'W	1932-1991	324	$\delta^{18}O$, ECM	Isaksson a. oth. 1996
y	SW_EPCIA	C	SWEDARP	1991/92	75°00'S	02°00'E	1865-1991	77	CD (sodium, nitrate), volc. hor.	Isaksson a. oth. 1996
y	SW92_1	C	SWEDARP	1991/92	74°10'S	00°22'E	1965-1993	116	total β	This paper
y	SW92_2	C	SWEDARP	1991/92	76°19'S	06°05'W	1955-1993	71	total β	This paper
y	Jut_A	C	NARE	1992/93	72°17'S	01°42'W	1976-1993	491	$\delta^{18}O$	Melvold 1999
y	Jut_B	C	NARE	1992/93	72°08'S	01°46'W	1976-1993	487	$\delta^{18}O$	Melvold 1999
y	Jut_C	C	NARE	1992/93	72°16'S	01°16'W	1976-1993	456	$\delta^{18}O$	Melvold 1999
y	Jut_D	C	NARE	1992/93	72°31'S	01°46'W	1976-1993	491	$\delta^{18}O$	Melvold 1999
y	Jut_E	C	NARE	1992/93	72°59'S	01°08'W	1965-1993	50	total β	Melvold 1998
y	Jut_F	C	NARE	1992/93	73°06'S	00°28'W	1965-1993	120	total β	Melvold 1998
y	Jut_H	C	NARE	1992/93	70°30'S	02°28'W	1976-1993	451	$\delta^{18}O$, total β	Melvold 1999
y	Jut_I	C	NARE	1992/93	71°31'S	01°11'E	1965-1993	60	total β	Melvold 1998
y	Jut_J	C	NARE	1992/93	72°13'S	00°43'W	1976-1993	320	$\delta^{18}O$, total β	Melvold 1999
y	Jut_K	C	NARE	1992/93	70°45'S	00°00'E	1976-1993	253	$\delta^{18}O$, total β	Melvold 1999
y	Jut_L	C	NARE	1992/93	70°56'S	00°13'E	1976-1993	244	$\delta^{18}O$, total β	Melvold 1999
y	Jut_M	C	NARE	1992/93	70°25'S	00°00'W	1984-1993	371	$\delta^{18}O$, total β	Melvold 1999
	SW93_1	P	SWEDARP	1993/94	73°28'S	12°34'W	1991-1993	280	CD (8 ions, $\delta^{18}O$)	Stenberg a. oth. 1998
y	SW93_2	P	SWEDARP	1993/94	74°58'S	11°48'W	1988-1993	120	CD (8 ions, $\delta^{18}O$)	Stenberg a. oth. 1998
y	SW93_3	P	SWEDARP	1993/94	78°02'S	10°59'W	1986-1993	90	CD (8 ions, $\delta^{18}O$)	Stenberg a. oth. 1998

y	SW93_4	P	SWEDARP	1993/94	75°33'S	09°46'W	1984-1993	70	CD (8 ions, $\delta^{18}O$)	Stenberg a. oth. 1998
y	SW93_5	P	SWEDARP	1993/94	75°29'S	09°05'W	1982-1993	60	CD (8 ions, $\delta^{18}O$)	Stenberg a. oth. 1998
y	SW93_7	P	SWEDARP	1993/94	75°30'S	04°35'W	1982-1993	60	CD (8 ions, $\delta^{18}O$)	Stenberg a. oth. 1998
y	SW93_9	P	SWEDARP	1993/94	75°30'S	02°41'E	1980-1993	50	CD (8 ions, $\delta^{18}O$)	Stenberg a. oth. 1998
	SW93_10	P	SWEDARP	1993/94	73°57'S	12°05'W	1991-1993	150	CD (8 ions, $\delta^{18}O$)	Stenberg a. oth. 1998
	SW93_11	P	SWEDARP	1993/94	74°16'S	11°46'W	1991-1993	150	CD (8 ions, $\delta^{18}O$)	Stenberg a. oth. 1998
	SW93_12	P	SWEDARP	1993/94	73°39'S	09°43'W	1990-1993	130	CD (8 ions, $\delta^{18}O$)	Stenberg a. oth. 1998
	SW93_13	P	SWEDARP	1993/94	72°01'S	08°45'W	1992-1993	390	CD (8 ions, $\delta^{18}O$)	Stenberg a. oth. 1998
y	FB96K02	C	AWI	1995/96	73°22'S	09°42'W	1964-1995	140	Artificial tritium (SS), ECM, DEP	Oerter a. oth. 1999
y	FB96DML01	C	AWI	1995/96	74°52'S	02°33'W	1895-1995	41	ECM, DEP, nss	Oerter a. oth. 1999
y	FB96DML02	C	AWI	1995/96	74°58'S	03°55'E	1919-1995	59	ECM, DEP, nss	Oerter a. oth. 1999
y	FBWatz95-2	C	AWI	1995/96	70°56'S	07°24'W	1964-1995	173	$\delta^{18}O$, 3H	This paper
y	S_{20}	C	NARE	1996/97	70°15'S	04°49'E	1965-1996	265	$\delta^{18}O$, ECM	Isaksson a. oth. 1999
y	S_{15}	C	NARE	1996/97	71°12'S	04°36'E	1965-1996	244	$\delta^{18}O$, ECM	Isaksson a. oth. 1999
y	A	C	NARE	1996/97	71°54'S	03°05'E	1965-1996	135	total β, ECM	Isaksson a. oth. 1999
y	B	C	NARE	1996/97	72°08'S	03°11'E	1965-1996	171	total β, ECM	Isaksson a. oth. 1999
y	C	C	NARE	1996/97	72°16'S	02°53'E	1965-1996	123	total β, ECM	Isaksson a. oth. 1999
y	D	C	NARE	1996/97	72°31'S	03°00'E	1965-1996	116	total β, ECM	Isaksson a. oth. 1999
y	E	C	NARE	1996/97	72°41'S	03°40'E	1965-1996	59	total β, ECM	Isaksson a. oth. 1999
y	F	C	NARE	1996/97	72°52'S	04°21'E	1965-1996	24	total β, ECM	Isaksson a. oth. 1999
y	G	C	NARE	1996/97	73°03'S	05°03'E	1965-1996	30	total β, ECM	Isaksson a. oth. 1999
y	H	C	NARE	1996/97	73°24'S	06°28'E	1965-1996	46	total β, ECM	Isaksson a. oth. 1999
y	I	C	NARE	1996/97	73°44'S	07°56'E	1965-1996	53	total β, ECM	Isaksson a. oth. 1999
y	J	C	NARE	1996/97	74°03'S	09°30'E	1965-1996	52	total β, ECM	Isaksson a. oth. 1999
y	K	C	NARE	1996/97	74°22'S	11°06'E	1965-1996	44	total β, ECM	Isaksson a. oth. 1999
y	L	C	NARE	1996/97	74°39'S	12°47'E	1965-1996	41	total β, ECM	Isaksson a. oth. 1999
y	M	C	NARE	1996/97	75°00'S	15°00'E	1965-1996	45	total β	Isaksson a. oth. 1999
	FB97DML01	C	AWI	1996/97	74°52'S	02°33'W	1964-1996	46	ECM, DEP, nss	Oerter a. oth. 1999
	FB97DML03	C	AWI	1996/97	74°30'S	01°58'E	1941-1996	91	ECM, DEP, nss	Oerter a. oth. 1999
y	FB97DML04	C	AWI	1996/97	74°24'S	07°13'E	1905-1996	53	ECM, DEP, nss	Oerter a. oth. 1999
	FB97DML05	C	AWI	1996/97	75°00'S	00°01'E	1930-1996	71	ECM, DEP, nss	Oerter a. oth. 1999
y	FB97DML06	C	AWI	1996/97	75°00'S	08°01'E	1899-1996	50	ECM, DEP, nss	Oerter a. oth. 1999
	FB97DML07	C	AWI	1996/97	75°35'S	03°26'W	1908-1996	57	ECM, DEP, nss	Oerter a. oth. 1999
y	FB97DML08	C	AWI	1996/97	75°45'S	03°17'E	1919-1996	60	ECM, DEP, nss	Oerter a. oth. 1999
y	FB97DML09	C	AWI	1996/97	75°56'S	07°13'E	1897-1996	45	ECM, DEP, nss	Oerter a. oth. 1999
y	FB97DML10	C	AWI	1996/97	75°13'S	11°21'E	1900-1996	47	ECM, DEP, nss	Oerter a. oth. 1999
	FB96K01	C	AWI	1996/97	74°13'S	09°45'W	1962-1995	125	ECM, DEP, nss	Oerter a. oth. 2000
y	FB9801	C	AWI	1997/98	70°43'S	08°26'W	1948-1997	317	ECM, CFA, nss	Oerter a. oth. 2000
y	FB9802	C	AWI	1997/98	74°13'S	09°45'W	1881-1997	129	ECM, CFA, nss	Oerter a. oth. 2000
y	FB9809	C	AWI	1997/98	74°30'S	01°58'E	1801-1997	89	ECM, CFA, nss	Oerter a. oth. 2000
y	B32	C	AWI	1997/98	75°00'S	00°01'E	1801-1997	62	ECM, CFA, nss	Oerter a. oth. 2000
y	FB9806	C	AWI	1997/98	75°00'S	00°02'E	1816-1997	62	ECM, CFA, nss	Oerter a. oth. 2000
y	FB9807	C	AWI	1997/98	75°00'S	00°02'E	1816-1997	67	CFA, nss	Oerter a. oth. 2000
y	B31	C	AWI	1997/98	75°35'S	03°26'W	1801-1997	59	ECM, CFA, nss	Oerter a. oth. 2000
y	SS9801	P	AWI	1997/98	74°51'S	08°30'W	1989-1997	76	ECM, CFA, nss	Oerter a. oth. 2000
y	FB9817	C	AWI	1997/98	75°00'S	06°30'W	1816-1998	62	CFA, nss	Oerter a. oth. 2000
y	FB9816	C	AWI	1997/98	75°00'S	04°30'W	1800-1997	47	CFA, nss	Oerter a. oth. 2000
y	FB9815	C	AWI	1997/98	74°57'S	01°30'W	1801-1997	53	CFA, nss	Oerter a. oth. 2000
y	FB9814	C	AWI	1997/98	75°05'S	02°30'E	1801-1997	64	ECM, CFA, nss	Oerter a. oth. 2000
y	FB9813	C	AWI	1997/98	75°10'S	05°00'E	1816-1997	48	CFA, nss	Oerter a. oth. 2000
y	B33	C	AWI	1997/98	75°10'S	06°30'E	1801-1997	47	ECM, CFA, nss	Oerter a. oth. 2000
y	FB9804	C	AWI	1997/98	75°15'S	06°00'W	1801-1997	50	ECM, CFA, nss	Oerter a. oth. 2000
y	FB9805	C	AWI	1997/98	75°10'S	01°00'W	1810-1997	44	ECM, CFA, nss	Oerter a. oth. 2000
y	FB9808	C	AWI	1997/98	74°45'S	01°00'E	1801-1997	68	ECM, CFA, nss	Oerter a. oth. 2000
y	FB9810	C	AWI	1997/98	74°40'S	04°00'E	1801-1997	86	CFA, nss	Oerter a. oth. 2000
y	FB9811	C	AWI	1997/98	75°05'S	06°30'E	1801-1997	58	CFA, nss	Oerter a. oth. 2000
y	FB9812	C	AWI	1997/98	75°15'S	06°30'E	1816-1997	38	CFA, nss	Oerter a. oth. 2000
y	FB9818	C	AWI	1998/99	74°27'S	09°27'W	1958-1999	169	DEP, $\delta^{18}O$	This paper
y	FB9903	C	AWI	1999/00	74°50'S	00°01°E	1931-1999	80	DEP, $\delta^{18}O$	This paper
y	FB9904	C	AWI	1999/00	75°03'S	00°42'E	1935-1999	68	DEP, $\delta^{18}O$	This paper
y	CV	C	SWEDARP	1997/98	76°00'S	08°03'W	1810-1997	62	volc. horiz., total β	Karlöf a. oth. 2000
y	M1	C	BAS	1997/98	77°01'S	10°26'W	1816-1997	70	total β	This paper
y	M4	C	BAS	1997/98	77°03'S	10°20'W	1955-1997	63	total β	This paper
y	M5	C	BAS	1997/98	77°00'S	10°33'W	1955-1997	69	total β	This paper
y	M6	C	BAS	1997/98	77°01'S	06°40'W	1955-1997	68	total β	This paper
y	BAS-Depot	C	BAS	1997/98	77°02'S	10°30'W	965-1998	71	DEP (volc. horiz.)	Hofstede a. oth. 2004
	M150	C	NARE	2000/01	75°00'S	15°00'E	965-1998	43	DEP (volc. horiz.)	Hofstede a. oth. 2004
y	FB0501	C	AWI	2004/05	74°09'S	09°41'W	1975-2004	183	$\delta^{18}O$, DEP	This paper

ECM Electrical conductivity method CFA Continuous Flow Analysis SS Sea salt CD Chemical data
$\delta^{18}O$ Oxygen-isotope stratigraphy NSS Non-sea-salt sulphate (volcanic eruptions) DEP Dielectric profiling